École polytechnique de Louvain

Design, modelling, and experimental characterization of a helical electrodynamic suspension for MAGLEV systems

Author: **Alexandra Georgopoulos**
Supervisor: **Prof. Bruno Dehez**
Readers: **Prof. Paul Fisette, Dr. Benoît Herman, Dr. Joachim Van Verdeghem, Louis Beauloye**
Academic year 2024–2025
Master [120] in Electro-mechanical Engineering

Abstract

Magnetic levitation (MAGLEV) trains rely on distinct systems to achieve both the levitation and propulsion of the vehicle. Among the technologies used for levitation, electrodynamic suspensions (EDS) are based on repulsive forces through induced currents in a conductive track, produced by a time-travelling magnetic field. Recently, the electrodynamic wheel (EDW), which consists of permanent magnets (PMs), has been proposed as a device capable of providing both levitation and propulsion simultaneously. However, due to its prismatic topology and the flat guideway associated to it, there is significant potential to improve its efficiency.

This master's thesis focuses on the development of an EDW based on a helical arrangement of PMs and a coaxial circular track, providing levitation, propulsion and guidance. First, models based on 3D finite elements methods (FEM) using the software COMSOL Multiphysics® are developed, allowing the study and characterization of the proposed suspension. These models, based on the Lorentz-term for steady-state simulations or on moving meshes for time-dependent ones, are compared and discussed with regard to their validity, results and computational efficiency. Subsequently, the influence of the dimensional parameters of the wheel, as well as the influence of mechanical variables such as the driving speed or displacements, are assessed based on these models.

Then, a first insight of the dynamical behavior of a pod equipped with four helical electrodynamic wheels (HEDW), placed in set of two in parallel tracks on either side of the capsule, is investigated. This analysis is divided into two parts : the lateral dynamics resulting of a decentering of the wheel in the guideway, and the longitudinal dynamics to study acceleration and deceleration of the vehicle.

Finally, the study of possible discretization techniques of the ideal helix for manufacturing purposes and the conception of a scaled prototype allows the experimental validation of the FEM models. Moreover, different characteristics issued from the numerical characterization are reproduced and validated.

Acknowledgements

I would like to take this opportunity to thank all those who contributed to the successful completion of this master's thesis.

First and foremost, I would like to express my sincere gratitude to my supervisor, professor Bruno Dehez. I don't have the words to express how his constant enthusiasm, support, hours-long meetings and expertise meant to me. I would also like to thank him for the incredible opportunity he offered to pursue this amazing journey through a PhD thesis, which I have no doubts will be just as great an experience as this year has been with him.

I wish to extend my heartfelt thanks to Louis Beauloye, who accompanied me throughout this year and shared with me his knowledge on electrodynamic suspensions and 3D FEM modelling. Many problems would have stayed unresolved without his help.

This work would not have been possible without the resources and the numerous advices provided by other researchers - namely Adrien Robert, Louis Devillez and François Boulanger. I am profoundly grateful for their enthusiasm and support. I would also like to thank Dr. Joachim Van Verdeghem for his help and for lending his computer for the never-ending simulations, alongside his small jokes that somehow made me smile.

Special acknowledgements go to Dr. Benoît Herman who revised my prototype plans and agreed to read this master's thesis and be part of the jury. The same goes to prof. Paul Fisette, who's words of encouragements in the hallway always lifted up my days.

I am grateful to the CREDEM platform without which the prototype and test bench would not have been possible. In particular, I would like to thank Simon De Jaeger for setting up the sensor interface, Vincent Musette for the manufacturing of the various parts of the test bench, and Alban Maton for the permanent magnets EDM cutting.

Finally, I owe my deepest gratitude to my family and friends - and especially Pauline - for their endless encouragements and belief in me through these five years of education.

Use of Artificial Intelligence

Artificial intelligence, in particular ChatGPT, was used in this work as a tool for improving writing and spelling correction.

Contents

Symbols and Abbreviations

List of Symbols

Coordinate frames

(r, θ, z)	Cylindrical coordinate frame	
(x, y, z)	Cartesian coordinate frame	

Dimensional parameters

α	Helical angle	$[rad]$
λ	Helical lead	$[m]$
τ_θ	Azimuthal pole pitch	$[m]$
τ_z	Axial pole pitch	$[m]$
e	Nominal air gap	$[m]$
L	Wheel length	$[m]$
L_{air}	Lateral clearance of the air enclosing the 3D FEM geometry	$[m]$
p	Number of pole pairs	$[-]$
R_{air}	Radius of the air cylinder enclosing the 3D FEM geometry	$[m]$
R_{in}	Inner magnet radius	$[m]$
R_{out}	Outer magnet radius	$[m]$
R_t	Track inner radius	$[m]$
t_c	Core (back-iron) thickness	$[m]$
t_m	Magnet thickness ratio	[-]
t_t	Track thickness	$[m]$

Mechanical parameters

β	Track opening angle	$[rad]$
δ	Skin depth	$[m]$
δ_x	Lateral displacement	$[m]$
δ_y	Vertical displacement	$[m]$
γ	Slip	$[-]$
ω	Rotational speed	$[rad/s]$
ω_e	Electrical frequency	$[rad/s]$
ϕ	Track orientation	$[rad]$
V_R	Circumferential speed	$[m/s]$
V_S	Synchronous speed	$[m/s]$
V_T	Travel (longitudinal) speed	$[m/s]$

Forces and torque

F_x	Force in the X-direction (Cartesian coordinate frame)	$[N]$
F_y	Force in the Y-direction (Cartesian coordinate frame)	$[N]$
F_z	Force in the Z-direction (Cartesian coordinate frame)	$[N]$
$F_{//}$	Parallel force	$[N]$
$F_{\perp}$	Perpendicular force	$[N]$
F_{drag}	Drag force	$[N]$
$F_{guidance}$	Guidance force	$[N]$
F_{lift}	Lift (levitation) force	$[N]$
F_{thrust}	Thrust (propulsion) force	$[N]$
T_{drag}	Drag torque	$[Nm]$

Dynamical parameters

Φ	Roll	$[rad]$
Ψ	Yaw	$[rad]$
ρ	Air density	$[kg/m^3]$
Θ	Pitch	$[rad]$
A	Front area of the pod	$[m^2]$
C_D	Drag coefficient	$[-]$
D	Lateral distance between two HEDWs	$[m]$
D'	Longitudinal distance between two HEDWs	$[m]$
I_p	Pitch inertia	$[kg\,m^2]$
I_r	Roll inertia	$[kg\,m^2]$
m	Mass	$[kg]$

Field quantities

ϵ_r	Relative permittivity	$[-]$
$\mathbf{A}$	Magnetic vector potential	$[Tm]$
$\mathbf{B}$	Magnetic flux	$[T]$
$\mathbf{D}$	Displacement current	$[C/m^2]$
$\mathbf{E}$	Electrical field	$[V/m]$
$\mathbf{H}$	Magnetic field	$[A/m]$
$\mathbf{J}$	Currents density	$[A/m^2]$
$\mathbf{M}$	Magnetization vector	$[A/m]$
$\mathbf{T}$	Maxwell's stress tensor	$[N/m^2]$
μ_r	Relative permeability	$[-]$
σ	Electrical conductivity	$[S/m]$
B_r	Remanent flux density	$[T]$
V	Magnetic scalar potential	$[A]$

List of Abbreviations

DoF Degree of Freedom.

EDS Electrodynamic Suspension.

EDW Electrodynamic Wheel.

EMS Electromagnetic Suspension.

FEM Finite Element Method.

GDR Guidance-to-Drag Ratio.

GTR Guidance-to-Thrust Ratio.

HEDW Helical Electrodynamic Wheel.

LDR Lift-to-Drag Ratio.

LIM Linear Induction Motor.

LSM Linear Synchronous Motor.

LTR Lift-to-Thrust Ratio.

LWR Lift-to-Weight Ratio.

MAGLEV Magnetic Levitation.

MEF Magnetic and Electric Fields.

MLS Magnetic Lead Screw.

MSP Magnetic Scalar Potential.

MVP Magnetic Vector Potential.

PM Permanent Magnet.

RMM Rotating Machinery Magnetic.

SCM Superconducting Magnet.

TDR Thrust-to-Drag Ratio.

1 | Introduction

Contents

If we were to trace back the evolution of railway technologies throughout the years, the drive for high-speed would be the main factor pushing innovation and research. Along this, the recognition of sustainable transportation led to the development of environmental-friendly and low-consumption technologies. In other words : going further and faster, but greener [1–3].

During the past decades, in response to these two new challenges, a new type of transportation was developed : named MAGLEV for magnetic levitation. Based on travelling magnetic fields, MAGLEV trains are able to levitate above a conductive track, and thus benefit of frictionless motion. This feature has a number of advantages over traditional trains : high speeds above 400km/h are achievable, alongside reduced noise and vibrations. Therefore, comfort is preserved and the maintenance costs are lower due to the absence of wear of the wheelset and the guideway [4–8]. As of today, the main factor preventing the establishment of MAGLEV trains over traditional iron wheel-on-rails ones are the high costs associated to it - and especially linked to their initial investment [5].

Most MAGLEV vehicles developed so far rely on separate systems for levitation, propulsion and guidance. Regarding levitation, the two main technologies are electromagnetic suspensions (EMS) or electrodynamic suspensions (EDS). While the first rely on attractive forces generated between electromagnets and a ferromagnetic track, the second is based on repulsive forces. This master's thesis focuses on the development of a new EDS topology.

1.1 Electrodynamic Suspensions

Electrodynamic suspensions are based on the repulsive force between moving magnets and a conductive non-magnetic track, such as aluminum. Such systems can be implemented either with permanent magnets (PMs) or superconducting magnets (SCMs). These latter requiring cooling beyond a given temperature, they are thus associated to a higher energy consumption [4, 9, 10].

Faraday's law of induction states that a time-varying magnetic field relative to a non-magnetic conductive guideway induces eddy currents in this latter. Lenz's law then states that these induced currents generate a magnetic field in response, that opposes the change that caused it. This repulsive force has two components. The first, in the vertical direction, generates lift against gravity. The second, in the longitudinal direction, is termed as electrodynamic drag and resists the forward motion of the pod. The representation of an EDS formed with PMs is shown in Figure 1.1, along with its vehicle application.

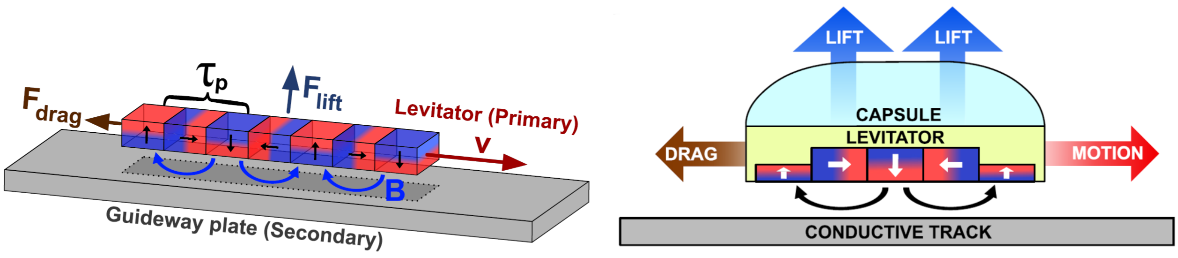

Figure 1.1: EDS representation. (a) PMs array. (b) Vehicle application. [10]

EDS are able to achieve air gaps up to 100mm, making them suitable for high-speeds and even freight applications. Moreover, they do not require control over said air gap, making them reliable and fail-safe for variations of loads. At low speeds, both the lift and the drag force increase with speed. At high speeds, both characteristic converge towards a bound value, a principle opposed to frictional aerodynamic drag [4, 9, 10]. This typical evolution of the forces of EDS is illustrated in Figure 1.2.

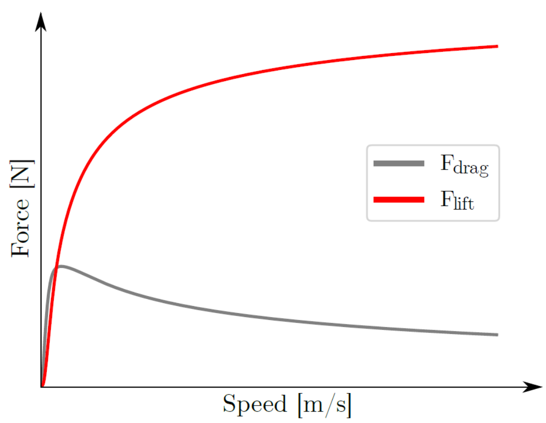

Figure 1.2: Typical evolution of the forces of EDS with speed [9].

The major drawback of EDS is the necessity of a secondary system at low-speed and rest, generally based on mechanical friction wheels, since sufficient levitation cannot be assured before a given cruising speed.

1.2 Linear Motors Propulsion

The propulsion of MAGLEV vehicles is usually achieved with synchronous (LSM) or asynchronous (LIM) linear motors. Their main objectives are to provide acceleration and deceleration, but also compensate the magnetic and aerodynamic drag at cruising speed. With the required coils placed onboard of the capsule or along the track, their principle is similar to that of a cut and open rotating motor [10]. An example of LSM is shown in Figure 1.3.

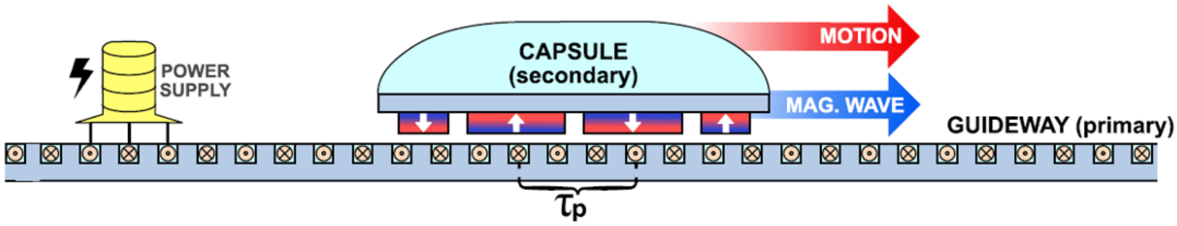

Figure 1.3: Linear synchronous motor used with on-board magnets for propulsion [10].

Faced with the challenge of environmental-friendly and low-consumption technologies, this master's thesis aims at studying an innovative topology of EDS based on a helical arrangement of PMs, able to ensure the three components of forces simultaneously needed to ensure the stability of a MAGLEV vehicle : levitation, propulsion and guidance.

2 | State of the Art

Contents

This chapter establishes the state of the art regarding the proposed helical electrodynamic suspension.

First, the prismatic electrodynamic wheel is introduced - a first system providing combined levitation, propulsion and guidance. Second, magnetic lead screws highlight the use of helical magnets arrangements. Finally, a history of patents mentioning the application of the helical wheel to MAGLEV transportation systems up to the present day is outlined.

2.1 Electrodynamic Wheel

The electrodynamic wheel (EDW) was first proposed in 1973 by R.C. Borcherts and L.C. Davis [11, 12], under the name of *Rotary Superconducting Motor* or *Superconducting Paddlewheel*, as an integrated levitation and propulsion device based on superconducting coils wound around a cylindrical core (also called drum). The device is illustrated in Figure 2.1, along with its intended application to high speed ground transportation systems.

Later on, in the early 2000s, the rapid improvement and discoveries regarding rare-earth magnets led to the development of PMs EDWs, notably as proposed and studied by J. Bird

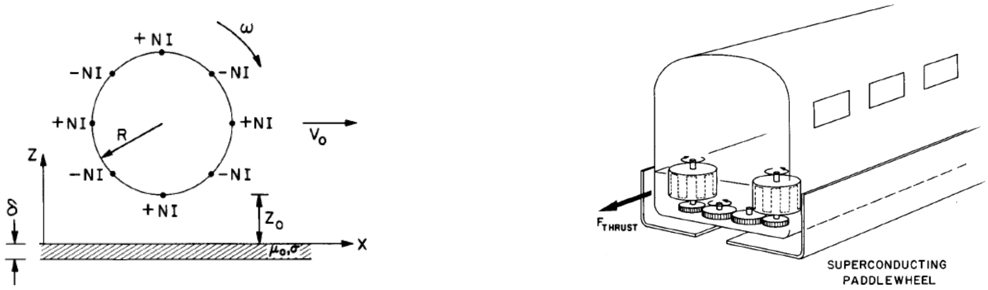

(a) (b)

Figure 2.1: The superconducting paddlewheel. (a) Device. (b) Application to transportation systems. [12]

in [13, 14]. The replacement of superconducting windings by PMs offers more sustainable and low-cost devices, since these latter do not require any additional cooling system to enhance their performance. However, a tradeoff arises from the inherent magnet's scarcity and initial investment costs associated with them.

As for traditional permanent magnets electrodynamic suspensions (PM-EDS), the motion of a magnetic source above a conducting non-magnetic guideway induces eddy currents generating reaction forces. The mechanical rotation of the PMs arrangement by an external drive motor generates the needed time-travelling magnetic field.
Moreover, the rotation of the wheel allows to convert the inherent drag force of traditional PM-EDS systems into a continuous propulsion force instead [5, 10, 13, 14].

Two main wheels configurations can be found in the literature, namely radial and axial, as represented in Figure 2.2 [15]. Their name derives from the orientation of their revolution axis with regards to the conductive guideway. For a radial configuration, the revolution axis is parallel to the track, whereas an axial configuration relies on a revolution axis perpendicular to it.

(a) (b)

Figure 2.2: Configurations of EDWs. (a) Radial. (b) Axial. [15]

2.1.1 Radial Electrodynamic Wheel

A radial configuration of EDW, formed with a Halbach array of PMs, is represented in Figure 2.3. The Halbach disposition of the magnets allows to strengthen the field at the circumference of the wheel, thus increasing the magnitude of the induced currents in the conductive plate.

The orientation of the propulsion force, denoted F_p, is dependent from the direction of the angular velocity ω_m, analogous to a friction force - and dictate the positively defined travelling direction of the wheel. By adjusting the relative slip speed between this rotational motion and the translational velocity of the suspension, acceleration or braking can be achieved [16, 17].

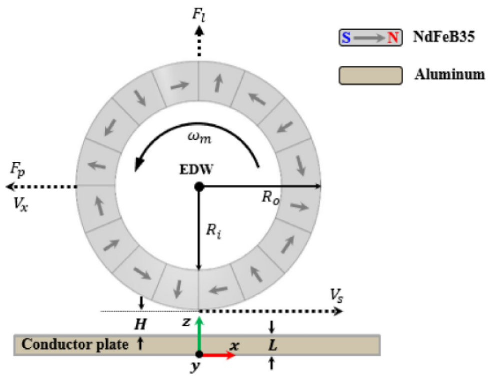

Figure 2.3: Halbach EDW and generated forces [16].

The study of placing EDWs in series [18] further led to the development of MAGLEV vehicles, which principle is illustrated in Figure 2.4. When two wheels are placed in the vicinity of each other, the second is able to take advantage of the first's magnetic field. Therefore, the coupling requires less mechanical energy to generate the same amount of forces, due to the increased magnetic field density.

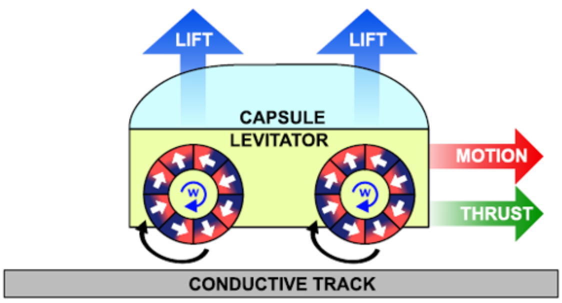

Figure 2.4: Vehicle equipped with EDWs [10].

For the most part, electrodynamic wheels are rotated by an external drive motor. Recently, an integrated motorisation system has been proposed in [19]. Illustration of this innovative solution can be found in Figure 2.5. A coupled and decoupled topologies are proposed, both relying on an outer EDW. If the PMs arrangement serves both the electrical motor while keeping their main intent for the suspension, the system is said coupled. If additional magnets are used for the motor's rotor, separated from the initial suspension array by a

ferromagnetic core, then the system is said decoupled.
Both approaches result in a more compact and energy-efficient device, due to the improved magnets' utilisation.

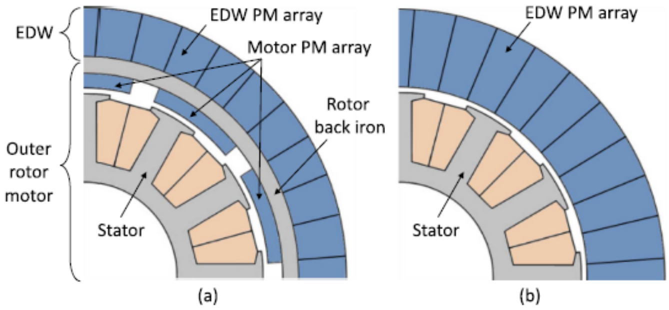

Figure 2.5: Integrated motor and outer EDW. (a) Decoupled. (b) Coupled. [19].

Vehicles equipped with EDWs are deemed suitable for high-speed as well as low-speed ground transportation applications [5, 15, 17]. Today's applications of vehicles equipped with radial electrodynamic wheels are driven towards four-wheels, although six-wheels vehicles are also proposed [20–22].

Similarly, vehicles equipped with four wheels in a two-by-two axial configuration have been developed and studied [23, 24]. As for the radial configuration, integrated motor devices have been developed in [25].

2.1.2 Guidance through Track Topologies

The third degree of freedom, guidance, is achieved passively through various guideway topologies.
The principal topology investigated by J. Bird for the EDW is the split-guideway, described in [5, 26, 27]. This system consists of two flat, parallel conductive plates, separated by an air gap, over which the wheel travels centrally. When it deviates sideways, the asymmetry in the eddy currents in both plates generates a restoring force that pushes the wheel back to the centerline. A representation can be found in Figure 2.6.

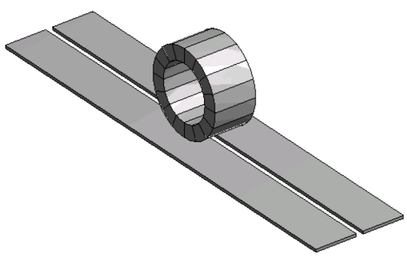

Figure 2.6: The split-guideway topology, assuring guidance of the EDW [5].

Based on the same principle of difference in currents density between plates to achieve guidance, several other topologies were investigated to ensure the stability of EDS. Among them, the U-guideway or channel described in [15]. A collection of proposed topologies is illustrated in Figure 2.7 [28].

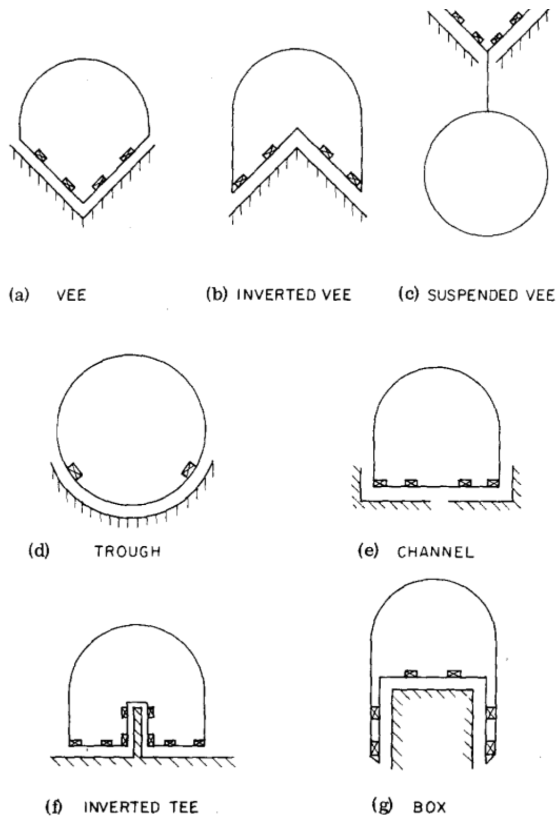

Figure 2.7: Various track topologies assuring guidance by difference in eddy currents density [28].

2.2 Magnetic Lead Screws

2.2.1 Ideal Surface Mounted Magnetic Lead Screw

Magnetic lead screws (MLS) use helical arrangements of PMs to convert between rotational and linear motions [29, 30]. As mechanical screws, they are composed of two main coaxial components : the screw and the nut. Unlike their mechanical counterpart, they offer frictionless motion. As represented in Figure 2.8, the ideal MLS consists of radially magnetized and skewed PMs mounted on the surface of both components. These magnets face each other across the air gap, and back-iron is placed behind them to guide the magnetic flux and reduce leakages.

When the pole pitches (i.e. the axial width of a single magnetic pole or magnet) are equal on both components, a full revolution of the nut (360°) results in a linear displacement of the screw equal to twice this pole pitch. If the pole pitches differ between the two parts, the MLS can then achieve a gearing action simultaneously.

To strengthen the magnetic field in the air gap between the screw and nut, a Halbach topology, as shown in figure Figure 2.9, can be considered. This results in enhanced thrust and torque [29, 31].

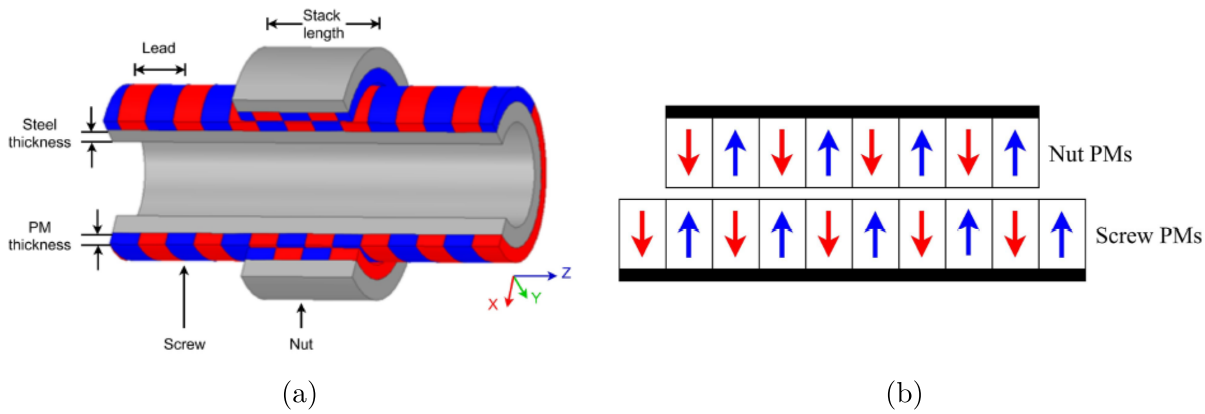

Figure 2.8: Ideal alternate radially magnetized MLS. (a) 3D model. (b) 2D axis symmetric model. [29]

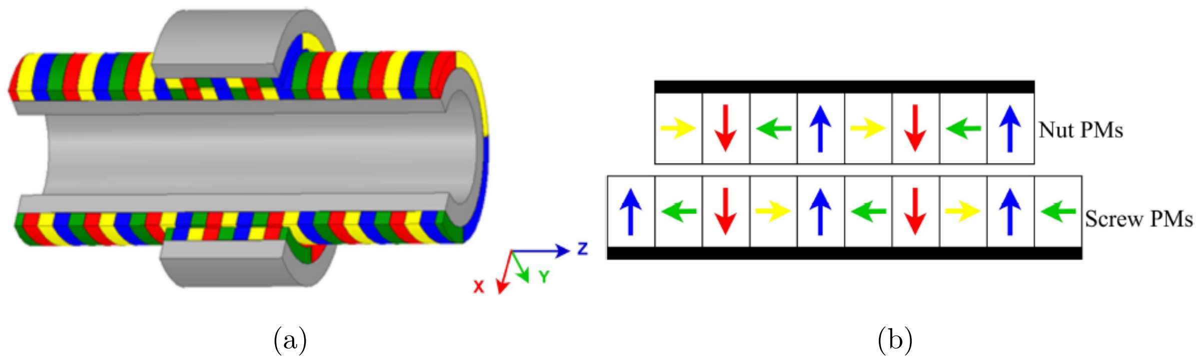

Figure 2.9: Ideal Halbach MLS. (a) 3D model. (b) 2D axis symmetric model. [29]

2.2.2 Ideal Spoke-Type Magnetic Lead Screw

In contrast to surface mounted topologies, are embedded or spoke-type ones. Axially magnetized PMs are placed between steel or iron segments, as illustrated in Figure 2.10. The magnetic flux is directed towards these ferromagnetic segments, and then across the air gap [29, 32].

Since the core does not contribute to guiding the flux, it should be made of a non-magnetic material in order to avoid short-circuiting the flux. Since magnetic material serve a preferential low-reluctance path for the flux, most of it would be concentrated in the yoke rather than through the air gap [32].

2.2.3 Discretized Magnetic Lead Screw

Ideal helical PMs are hard to manufacture. Discretized topologies aim to simplify the manufacturing process. The helix then consist of cut magnets, shifted longitudinally. The higher

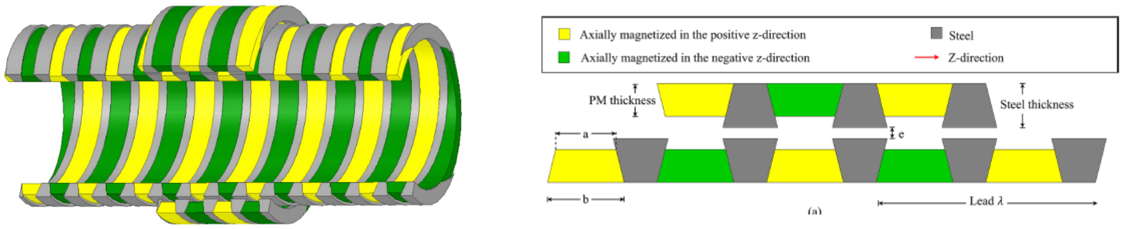

(a) (b)

Figure 2.10: Ideal spoke-type MLS. (a) 3D model. (b) 2D axis symmetric model. [29]

the number of discretized elements, the better the approximation of the ideal helix. However, since custom-made magnets are needed, this might result in high overall costs [29, 33].

Figure 2.11 represents a discretized topology as developed in [34]. Since the magnets segments are embedded, these are axially magnetized. To smooth the resulting flux, an additional ideal helical iron ring can be placed above the screw.

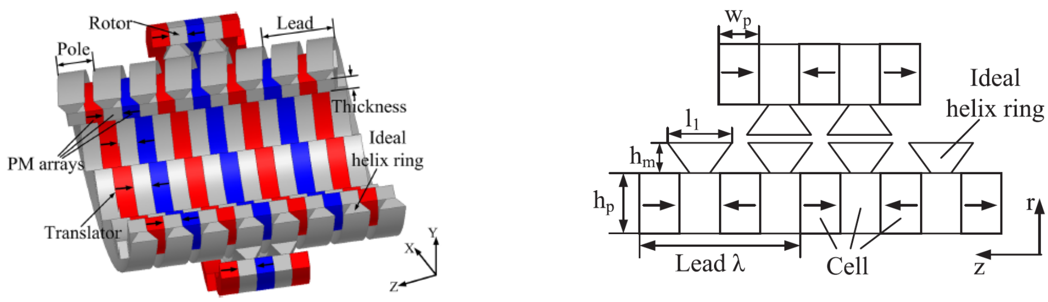

(a) (b)

Figure 2.11: Discretized embedded MLS. (a) 3D model. (b) 2D axis symmetric model. [34]

Several designs of discretization were envisaged for the MLS, notably with circular magnets also [33, 34].

2.3 Applications of Helical Wheels to Ground Transportation

This section traces back the history of patents mentioning the application of a helical wheel to MAGLEV transportation systems.

2.3.1 Superconducting Screw

Simultaneously to proposing the superconducting paddlewheel, L.C. Davis and R.H. Borcherts introduced the superconducting screw for high speed ground transportation in 1973 [12]. Represented in Figure 2.12, it is composed of two windings around a common cylindrical core, wound such as to generate a helical magnetic field. These windings have N turns each, and carry a current in opposite directions, thereby establishing alternating north and south magnetic poles along the axis of the core.

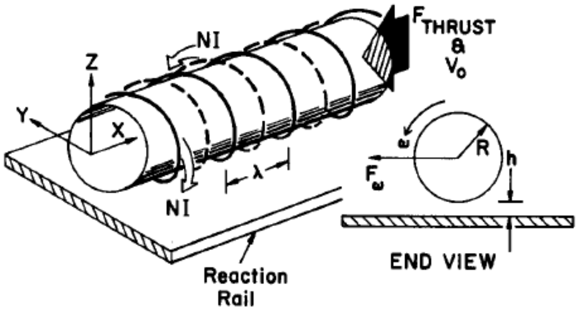

Figure 2.12: Schematic diagram of a double helix superconducting screw [12].

The integration of the superconducting screw for a vehicle destined to high speed ground transportation is represented in Figure 2.13. The suspension is placed longitudinally, with its revolution axis parallel to the moving direction, on either side of the capsule to provide stability. The reaction plate or guideway is placed in-between the two screws, as a box channel (Figure 2.7). As for the EDW, an auxiliary drive motor must rotate the screw. The moving magnetic field therefore induces a thrust force axially, and a levitation force perpendicular to this latter.
The system was studied with the help of a simplified analytical modelling, made possible by the flat guideway topology, but never tested due to feasibility concerns regarding the material strength and cryogenics aspects for superconducting windings. Moreover, to maximize the efficiency of the screw suspension, this latter should be long enough in order to minimize the end effects, increasing the complexity of the mechanical integration design.

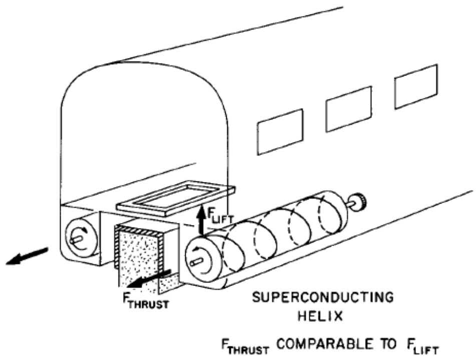

Figure 2.13: Integration of the superconducting helix for a high speed ground transportation system [12].

2.3.2 Helical Permanent Magnets Wheel

In 1982, the helical electrodynamic wheel based upon PMs is introduced [35]. Illustrated in Figure 2.14, the device is composed of ideal double helices without spacing, forming a surface mounted alternate north-south topology.

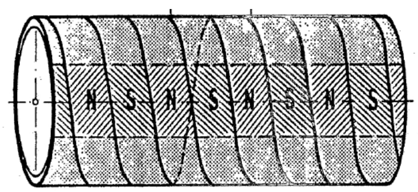

Figure 2.14: Helical electrodynamic wheel formed with permanent magnets [35].

As for the EDW, the wheel is driven by an external motor in order to generate a time-travelling magnetic field. The considered track, shown in Figure 2.15, is slightly curved.

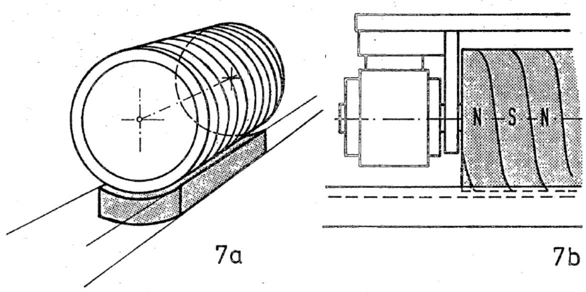

Figure 2.15: Application to ground transportation systems. (a) Slightly curved track. (b) Additional drive motor. [35]

2.3.3 Double Helices Non-Contacting Drive

In 1992, P. Schuster filed a patent for a magnetic helix non-contacting drive [36], where it presents a rotating part called linear drive formed of double helices with spacing between them. The proposed tracks were either a flat profiled one, or a coaxial ferromagnetic guideway that encircles the system.

Figure 2.16 illustrates two possible embodiments. The linear drive is composed of a soft magnetic core, around which radially magnetized PMs doubles helices are placed such as to create an alternate topology.
On the left side (Fig. 1 and Fig. 3) of Figure 2.16, two linear drives share a common profiled track. The drives are arranged such that the north and south poles symmetrically align on opposite sides of that guideway. In order to keep this alignment, both screws have to rotate synchronously.
On the right side (Fig. 2 and Fig. 4) of Figure 2.16, a unique linear drive is surrounded by two flat profiled tracks, enhancing stability and guidance from both sides.
The guideway (Fig. 5) features recess windows that are equidistant to the magnetic pole pitch.

Figure 2.17 (Fig. 6 and Fig. 7) represents the same double helices drive with radially magnetized PMs. The guideway now coaxially encircles the linear drive as a tube, and is composed of hills and valleys that are once again equidistant to the magnetic pole pitch. The curved guideway may surround the drive almost entirely or partially, to increase the

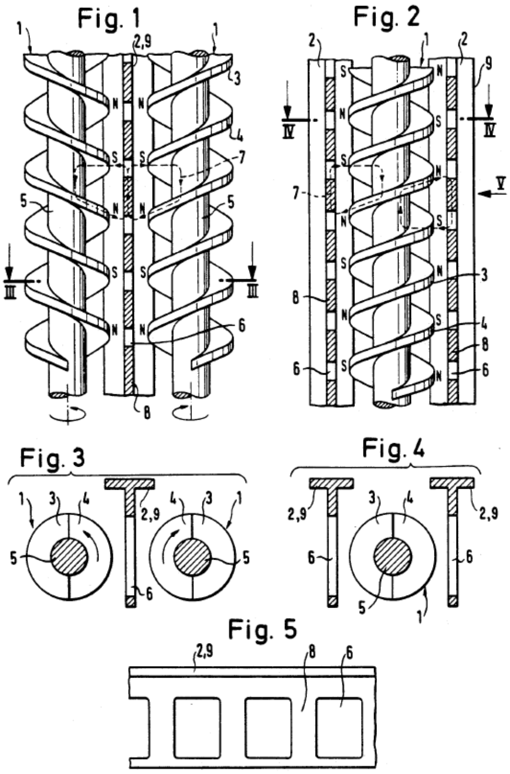

Figure 2.16: Double helix linear drive with flat guideway. (Fig. 1 and Fig. 3) Shared guideway between two drives. (Fig. 2 and Fig. 4) Double guideway for a single drive. (Fig. 5) Recesses in said guideway. [36]

efficiency. A section of the guideway is left opened to let mounting or fixing elements pass.

Similarly to MLS topologies, a spoke-type version based on embedded axially magnetized PMs was proposed. Moreover, the double helices can be placed either on the capsule or the guideway itself. However, for applications to transportation systems, it is appropriate to have a fixed guidance part and the drive mounted on the vehicle in order to reduce the number of PMs involved.

2.3.4 Device for Electromagnetic Levitation and Propulsion

The most recent patent describing a device for electromagnetic levitation and propulsion based on a helical structure of PMs dates from 2022 [37]. As represented in Figure 2.18, different couplings with multiple wheels, namely parallel or series, are exploited.

To reduce end-effects, conically-shaped structures at both end of the cylinder are introduced. These are illustrated in Figure 2.19. These latter rotate freely, and are thus not driven alongside the main cylinder. Therefore, their length must be adjusted according to the nominal speed of the vehicle.

The patent also proposes several track topologies where parallel combinations of wheels share the same guideway. The track can be either flat or curved around the cylinders, and with various opening angles. These are represented in Figure 2.20. Since the guideway is

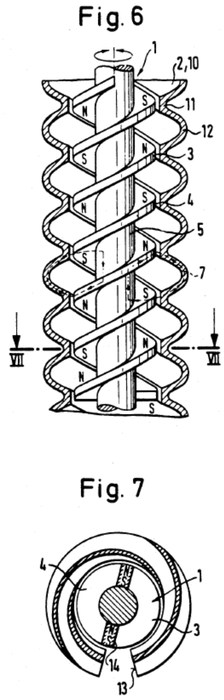

Figure 2.17: Double helix linear drive with coaxial circular guideway [36].

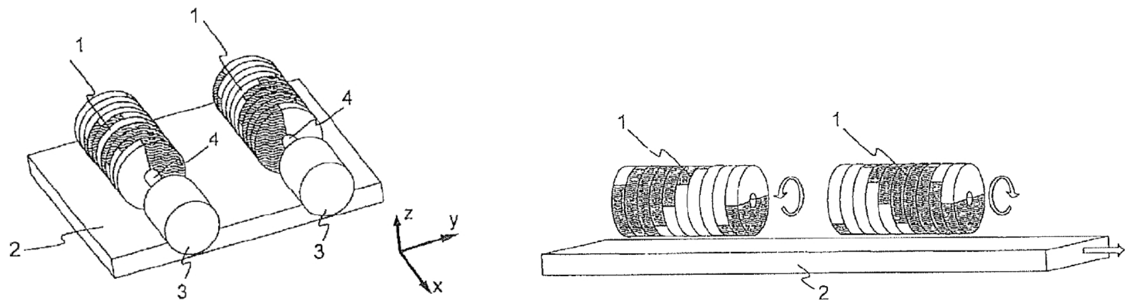

(a) (b)

Figure 2.18: Coupling of helical electrodynamic wheels. (a) Parallel coupling. (b) Series coupling. [37].

unique and shared, the magnetic field generated by both wheels passes through the same section of conductive material in the middle. This increases the eddy currents locally, leading to fewer losses for the same drive power.

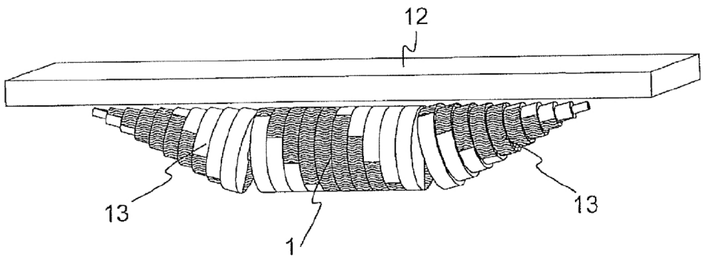

Figure 2.19: Additional conically-shaped structures to reduce end-effects [37].

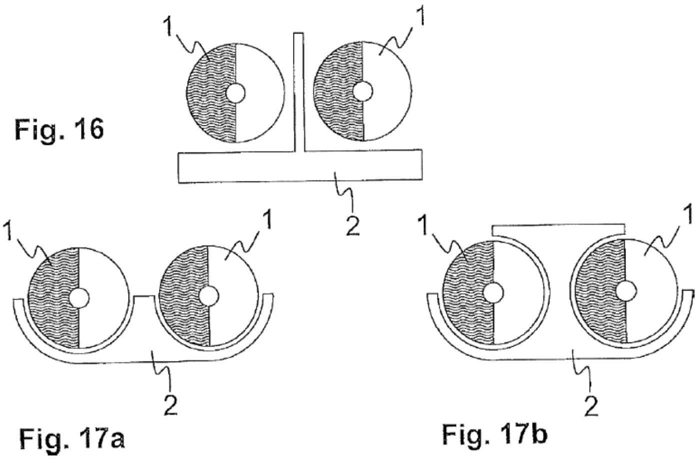

Figure 2.20: Proposed shared track, either flat or circular [37].

3 | Research Objectives

Contents

3.1 Concept and Functional Principles

The electrodynamic wheel as studied by J. Bird in [5] provides the three fundamental forces needed for a MAGLEV vehicle simultaneously : levitation, propulsion and guidance through track topologies. However, due to the prismatic wheel and flat guideway, the active part of PMs contributing to the induced forces instantaneously is rather low : the projection of a single line parallel to the track.

The proposed helical electrodynamic wheel (HEDW) alleviates this problem by considering a curved track on an arc of a circle whose revolution axis is parallel to that of a cylindrical wheel, therefore increasing the part of PMs contributing to the generation of forces : the projection of the guideway spanning angle. Representation of this can be found in Figure 3.1, where the track opening is 180 degrees. This results in a more cost-effective and energy-efficient technology, alleviating the problems associated with the ratio between the mass of the magnets and the levitation produced encountered by the prismatic EDW.

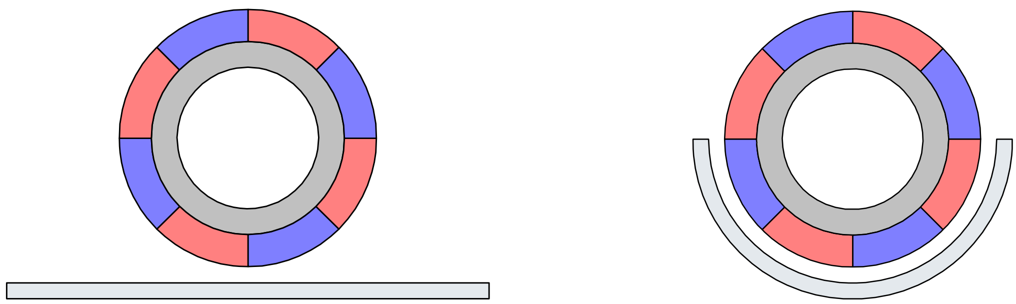

(a) (b)

Figure 3.1: Comparison between the prismatic EDW and the proposed HEDW. (a) Prismatic EDW with a flat guideway. (b) Proposed HEDW with curved guideway.

The helical arrangement of PMs around the axial direction generates a static magnetic field, that when rotated mechanically creates a travelling magnetic field in the longitudinal direction, based on the same principle as the magnetic lead screw. This longitudinal motion of the field creates propulsion, whereas levitation is assured such as for traditional EDS. The curvature of the track, surrounding the wheel, serves as guidance.

The proposed application vehicle would be equipped with four of such HEDWs, by pair of two in distinct parallel tracks. This vehicle is illustrated in Figure 3.2.

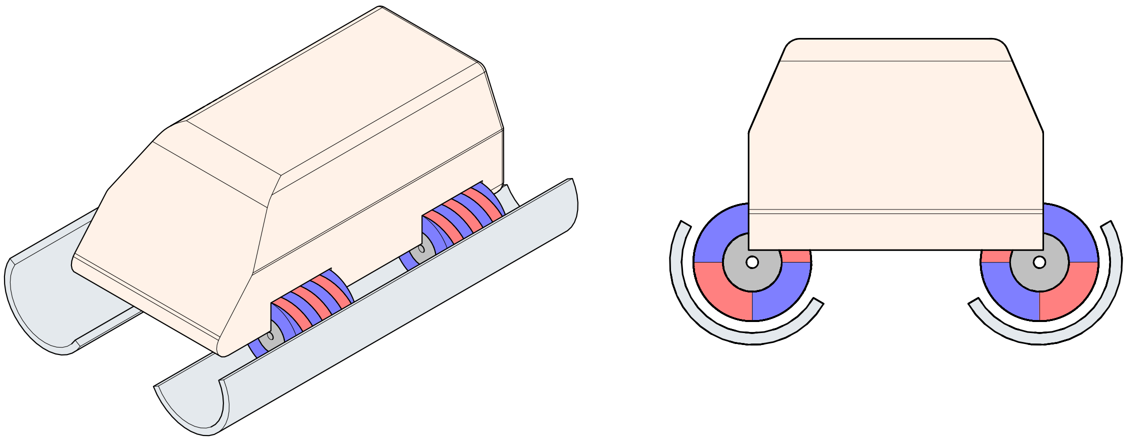

Figure 3.2: Proposed application vehicle, equipped with four HEDWs placed by pair of two in distinct parallel tracks.

A MAGLEV vehicle, assimilated to a floating body in space, has six degrees of freedom : three translational movements already mentioned and being the levitation, propulsion and guidance - as well as three angular motions being the roll, the pitch and the yaw of the pod.
Stability can be achieved by controlling the direction of rotation, as well as the angular speed, of the four wheels independently. However, since each wheel generates the three forces components simultaneously (levitation, guidance, propulsion), this implies dynamical coupling between the six degrees of freedom. Additionally, control could also be ensured by varying the opening or the orientation of the conductor from one section of track to another.

3.2 Scope of the Study

The aim of this master's thesis is to design, model and characterize a HEDW capable of providing combined levitation, propulsion and guidance forces for a MAGLEV vehicle. The scope and different steps of this study are illustrated in Figure 3.3.

The first objective is to develop a model that can be used to analyze and characterize the proposed wheel. These models, based on 3D finite element methods (FEM), should thus be able to predict the forces induced in the three directions of a Cartesian coordinate frame for a single wheel in quasi-static equilibrium. A discussion will be opened on the different model formulations and their impact on the results, as well as the appropriateness of carrying out a numerical characterization on them.

With the help of these models, the second objective is the study and the characterization of the proposed HEDW. This analysis includes the influence of two subsets of parameters to be evaluated : the dimensional parameters and the mechanical or control variables. Dimensional parameters include the radius and length of the wheel, or its number of poles pairs and helical angle. Mechanical variables include the speed of rotation of the wheel, its longitudinal travel speed, or its relative positioning with regard to the guideway.

Following this characterization, the third objective is to perform a first dynamical analysis of the proposed vehicle. With the help of the results obtained through simulations, a first prediction of the lateral behavior, subject to various displacement disturbances, can be assessed. Moreover, the principle behind the acceleration and deceleration of the pod, in the longitudinal plane, are studied.

Finally, the conception of a scaled prototype will serve to validate the presented models and results with an experimental characterization.

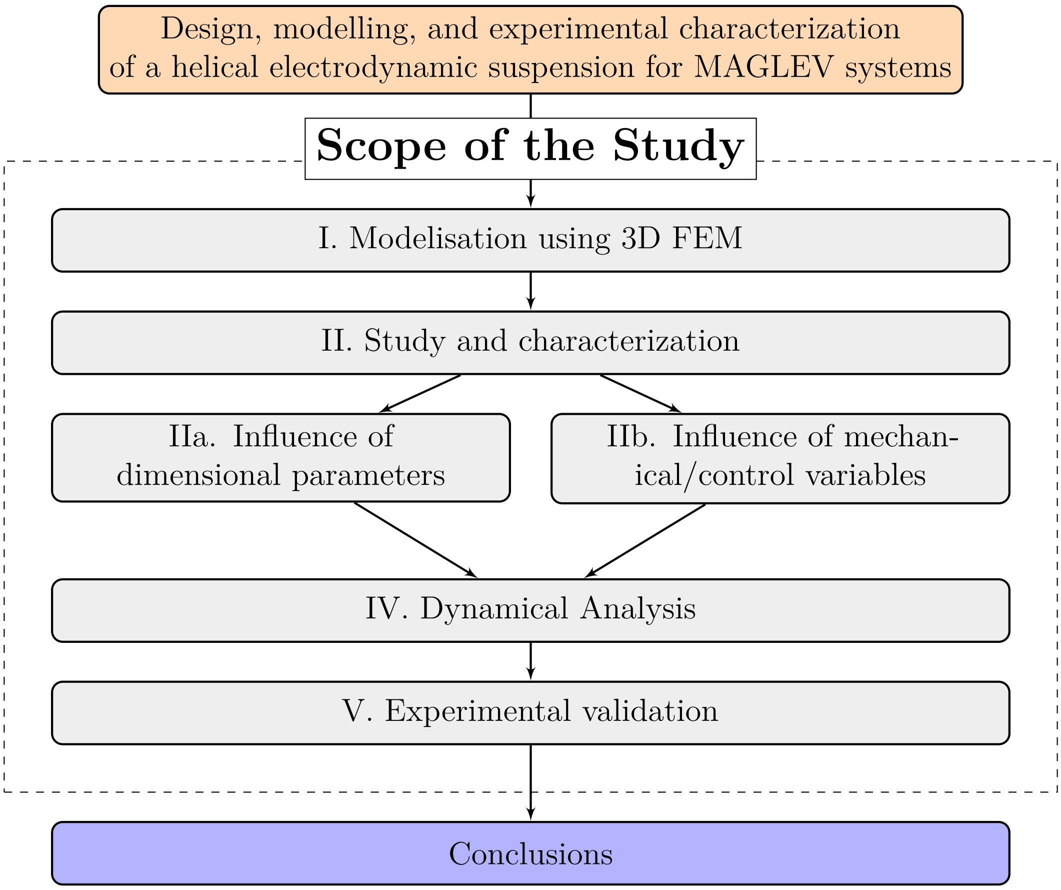

Figure 3.3: Scope of the Study.

4 | Helical Electrodynamic Wheel

Contents

This chapter focuses on the definition of the HEDW, more specifically of its dimensional and mechanical parameters. Then, the generated static magnetic field for the considered study case is illustrated.

4.1 Definition and Dimensional Parameters

The HEDW is based on several circular helices of PMs around a cylindrical core, creating a heteropolar static magnetic field. The circular helix itself is defined to have a constant radius R around the axial direction (length of the wheel), and thus a constant torsion. The mathematical set of parametric equations describing a right-handed helix spiraling around the z-direction in a Cartesian coordinate frame (x, y, z) is the following :

$$\begin{cases} x(t) = R\cos(t) \\ y(t) = R\sin(t) \\ z(t) = ct \end{cases} \tag{4.1}$$

Where t is a parameter evolving in the interval $[0; 2\pi]$ for a single turn, and c a constant that determines the spacing of the helix along the z-axis (named pitch or lead). The slope and the lead are then expressed as :

$$slope = \frac{R}{c} = tan(\alpha) \tag{4.2}$$

$$lead = 2\pi c = 2\pi \frac{R}{tan(\alpha)} = \lambda \tag{4.3}$$

Where α is known as the helical angle. The ideal HEDW is then built on the idea of extruding the section of a circular magnet along this helical path, as represented in Figure 4.1a. The combination of several magnetic helices, without gaps in between them, forms the proposed suspension.

The number of helices defines the number of magnetic poles of the suspension, each of which is fully polarized in the same direction. An alternate topology of radially magnetized helices is depicted in Figure 4.1b, and this latter will serve as the case study throughout this research. Other possible topologies are described in Appendix A. The assembly of four alternating north-south helices thus constitute two pair of poles in this example.

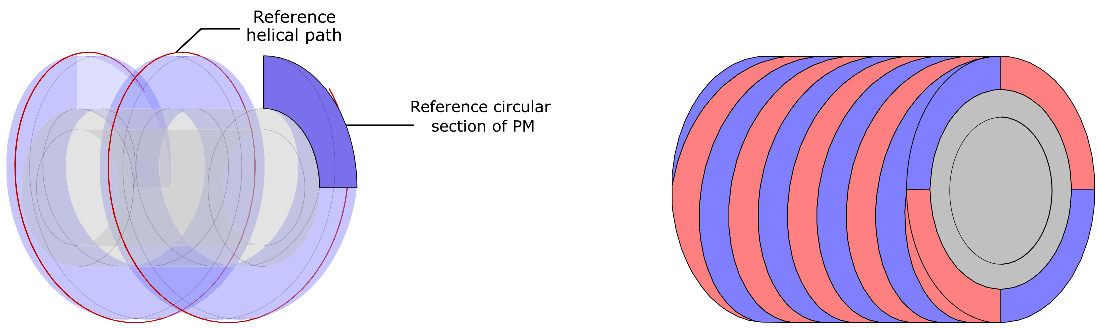

(a) (b)

Figure 4.1: The ideal HEDW. (a) Extrusion of a circular section of PM along a defined helical path to form the ideal magnetic helix. (b) Combination of several helices to form a two pair of poles ideal alternate HEDW.

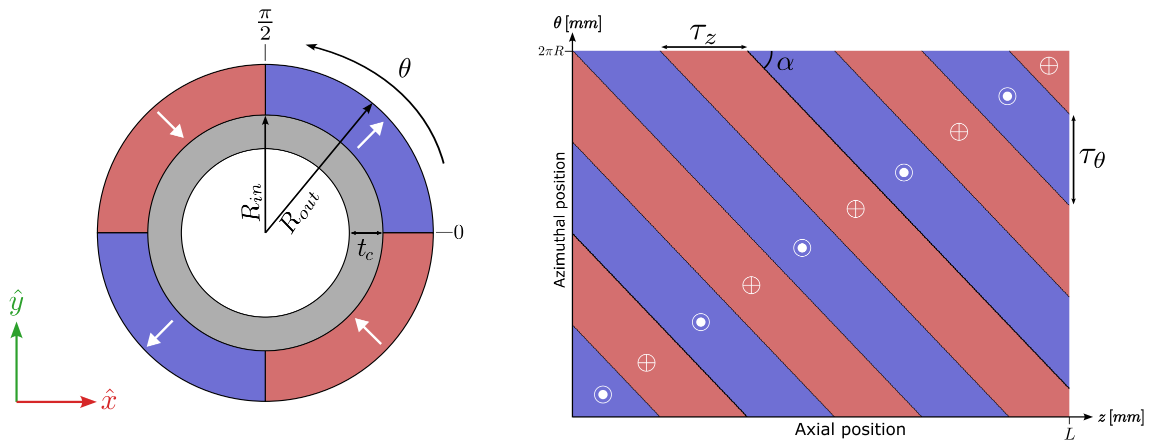

(a) (b)

Figure 4.2: Ideal alternate HEDW. (a) Cross-sectional view in Cartesian coordinate frame. (b) Unwound 2D-plane in cylindrical coordinate frame.

We define R_{in} the inner magnet radius, R_{out} the outer magnet radius and L the length of the wheel - as illustrated in Figure 4.2.

Unwinding the wheel in a cylindrical coordinate frame (r, θ, z) allows to better visualize and define several other dimensional parameters. Figure 4.2b represents the HEDW in a 2D plane, where the horizontal axis represents the axial length and the vertical axis the azimuthal direction along the circumference of the wheel. Such a plane is defined for a given radius R of the wheel in the thickness range of the magnets $(R_{in} < R < R_{out})$. The helical angle α is the primary parameter that defines the curvature of the helices. This parameter can take a value between 0° and 90°. The greater α, the more wound each helix is around the cylindrical core - whereas the particular case of $\alpha = 0°$ refers to the prismatic EDW. This influence of α is depicted in Figure 4.3. The thickness of the cylindrical core is defined as t_c. Table 4.1 summarizes these primary dimensional parameters of the wheel.

(a) (b)

Figure 4.3: Influence of the helical angle α. (a) High α (close to 90°), resulting in very wound helices. (b) Low α (close to 0°), resulting in a configuration close to the prismatic EDW.

Primary parameter	**Symbol**	**Unit**
Inner magnet radius	R_{in}	m
Outer magnet radius	R_{out}	m
Core thickness	t_c	m
Wheel length	L	m
Number of pole pairs	p	-
Helical angle	α	rad

Table 4.1: Primary dimensional parameters of the HEDW.

In the field of electrodynamic suspensions, the pole pitch of the magnets (their width) is the parameter that dictates the system's performances. In this particular arrangement, two distinct pole pitches can be defined: the azimuthal pole pitch τ_θ and the axial pole pitch τ_z. As they can be defined based on the previously presented primary parameters, they will be attached to a second set of parameters, named secondary parameters of the wheel. Both pole pitches can be visualized in Figure 4.2b. The importance of the helical angle α on the axial pole pitch τ_z can be clearly visualized in Figure 4.3.

The axial pole pitch τ_z is similar in definition to the pitch of a screw. It must not be mistaken with the lead of a single helix: the distance that helix travels axially in one complete turn (2π). Therefore, the pole pitch of the magnets will always be defined as the axial length or width of a magnetic pole along the wheel axis. This distinction is represented in Figure 4.4.

Based on the primary parameters, the pole pitches can therefore be expressed as :

$$\tau_\theta = \frac{2\pi R_{out}}{2p} = \frac{\pi R_{out}}{p} \tag{4.4}$$

$$\tau_z = \frac{2\pi R_{in}}{p\, tan(\alpha_{in})} = \frac{2\pi R_{out}}{p\, tan(\alpha_{out})} \tag{4.5}$$

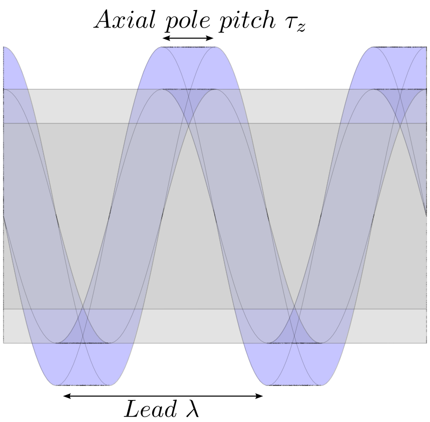

Figure 4.4: Distinction between pitch and lead of a PM helix.

When the lead of a helix is kept constant, the helical angle naturally varies with the radius. As the radius increases, the helical angle increases also, as the helix wraps around a wider circumference over the same axial distance. Physically, this is a direct consequence of the extrusion of a section of circle to form the ideal helix. Mathematically, this comes from the definition of the helical path, where the ratio $\frac{R}{tan(\alpha)}$ of Equation 4.3 must be kept constant. If R varies, so must $tan(\alpha)$. This key principle is illustrated in Figure 4.5.

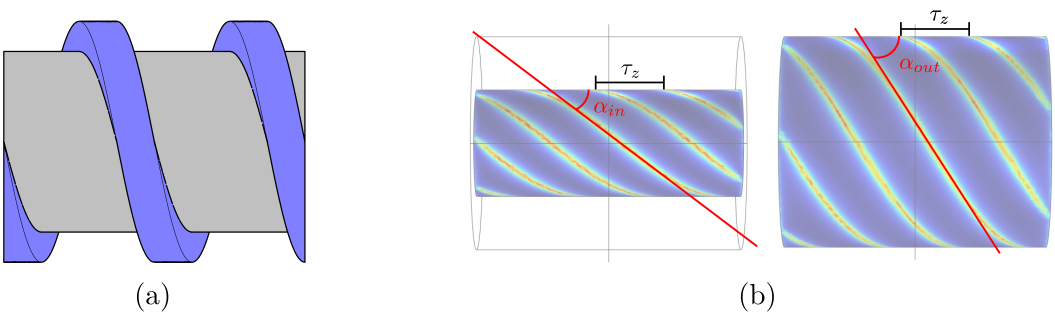

Figure 4.5: Difference in helical angle α between the inner magnet radius R_{in} and the outer magnet radius R_{out}. (a) Consequence from the extrusion of a section of PM circle to form the ideal helix. (b) Resulting difference to keep constant axial pitch τ_z (from COMSOL Multiphysics®).

Knowing the inner helical angle, the resulting one at the outer radius can be deduced with the help of Equation 4.6 :

$$\alpha_{out} = tan^{-1}\left(\frac{R_{out}\, tan(\alpha_{in})}{R_{in}}\right) \tag{4.6}$$

The last secondary parameter is the ratio between the inner and outer magnet radius, defined as t_m, that in some sense expresses the thickness of the magnets considered. If t_m is close to 1, then the magnets are thin with regard to the outer diameter of the wheel. Oppositely, the more t_m approaches the zero value, the more we tend to a full cylinder of PMs - and where the core tends to disappear.

$$t_m = \frac{R_{in}}{R_{out}} \tag{4.7}$$

Table 4.2 summaries the secondary parameters of the proposed helical electrodynamic suspension.

Secondary parameter	**Symbol**	**Unit**
Azimuthal pole pitch	τ_θ	m
Axial pole pitch	τ_z	m
Magnet ratio	t_m	-

Table 4.2: Secondary dimensional parameters of the HEDW.

Regarding the track, made of a non-magnetic conductive material such as aluminum, it is formed by a section of hollow cylinder whose axis of revolution is placed parallel to the axis of rotation of the wheel. As for the suspension itself, the guideway can be defined with a set of dimensional parameters, illustrated in Figure 4.6. The thickness of the track is denoted t_t. The nominal air gap e when the wheel is centered defines the inner radius of the track R_t, such that :

$$R_t = R_{out} + e \tag{4.8}$$

Table 4.3 summarizes the dimensional parameters of the track.

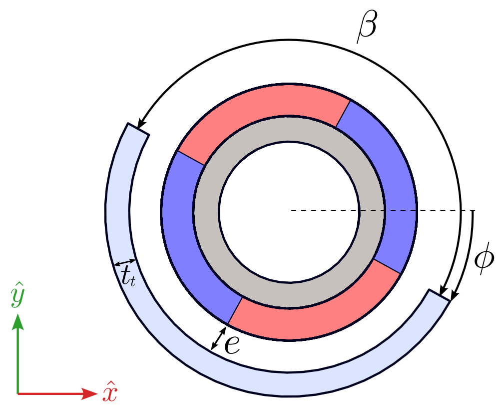

Figure 4.6: Dimensional parameters regarding the conductive track.

Dimensional parameter	**Symbol**	**Unit**
Track inner radius	R_t	m
Nominal air gap	e	m
Track thickness	t_t	m

Table 4.3: Dimensional parameters of the track

4.2 Mechanical Variables

This section describes the mechanical parameters, related to the speed and position of the HEDW or the opening and orientation of the track.

As illustrated in Figure 4.6, the track can span a full circle (360°) or have a given opening angle β to allow structural mounting elements to pass. In such case, the resulting span of conductor is thus $360° - \beta$. Moreover, the track can be inclined by an angle ϕ with regard to the horizontal plane.

Figure 4.7 illustrates the two velocity components of the HEDW, namely the rotational speed ω and the travel or longitudinal speed V_T in the desired direction of motion. The circumferential speed V_R is defined based on the rotational speed ω and the outer radius R_{out} as :

$$V_R = \omega R_{out} \tag{4.9}$$

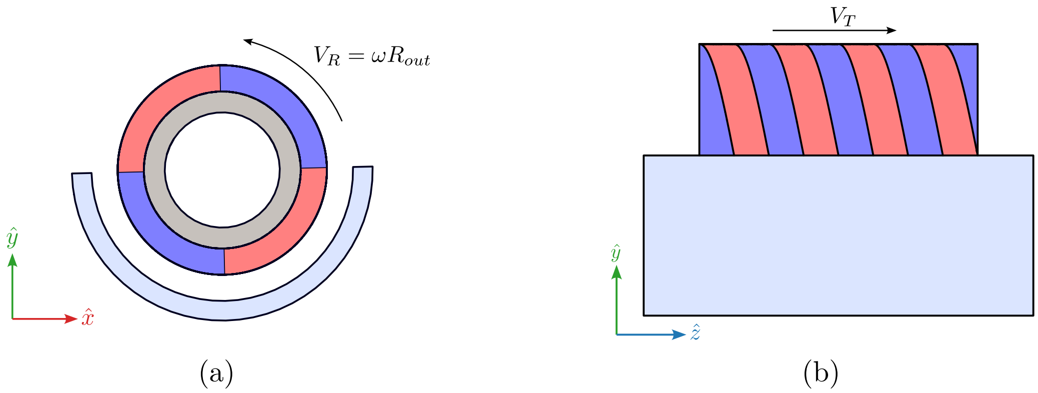

Figure 4.7: Speeds. (a) Circumferential speed. (b) Travel (longitudinal) speed.

The dynamical motion of the pod may introduce relative displacements of the wheel inside the track. These displacements, when seen from a Cartesian coordinate frame (x, y, z), can be either lateral and denoted δ_x or vertical and denoted δ_y. Such displacements, defined with regard to the center of the wheel, are represented in Figure 4.8.

The position of the wheel, as well as its speeds, are essential information for the control of the vehicle. Therefore, these variables take the appellation of mechanical or control variables. Table 4.4 summarizes these parameters.

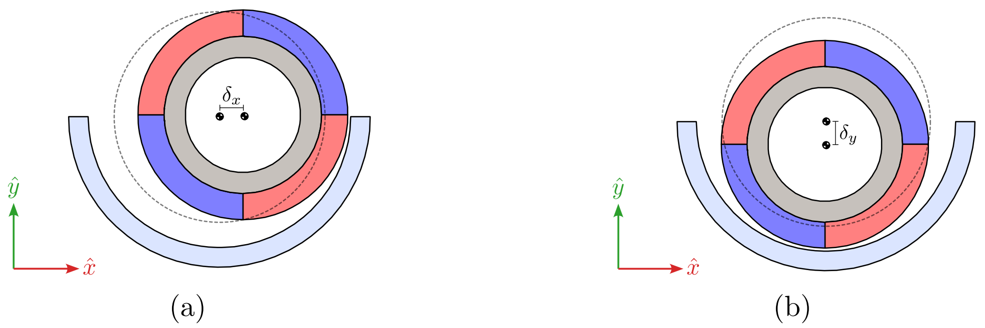

Figure 4.8: Displacement of the HEDW inside the track. (a) Lateral displacement δ_x. (b) Vertical displacement δ_y.

Mechanical parameter	**Symbol**	**Unit**
Track opening	β	rad
Track orientation	ϕ	rad
Rotational speed	ω	rad/s
Circumferential speed	V_R	m/s
Translational speed	V_T	m/s
Lateral displacement	δ_x	m
Vertical displacement	δ_y	m

Table 4.4: Mechanical or control variables of the track and the HEDW.

4.3 Static Magnetic Field

This section presents the static magnetic field generated by the ideal two pole pairs alternate HEDW that serves as case study.

Figure 4.10 depicts the magnetic flux norm **B** as well as its components in a cylindrical coordinate system (r, θ, z). These components are plotted along two paths, illustrated in Figure 4.9 : a circular path in the air gap that encircles the wheel at its mid-length, and a linear path running along the axial direction of the wheel, also positioned in the air gap at a fixed radius. The choice of cylindrical coordinates is aligned with the ideal radial magnetization of the wheel.

The magnetic flux norm is defined as :

$$|\mathbf{B}| = \sqrt{B_r^2 + B_\theta^2 + B_z^2} \tag{4.10}$$

The four peaks of $|\mathbf{B}|$ in Figure 4.10a correspond to the four individual poles (two north and two south) constituting the two pole pairs configuration.

The end-effects can be visualized in Figure 4.10b, where the start and end of the wheel are defined by the two vertical dotted lines. All flux components decrease exponentially starting from the boundaries, before finally reaching the null-value.

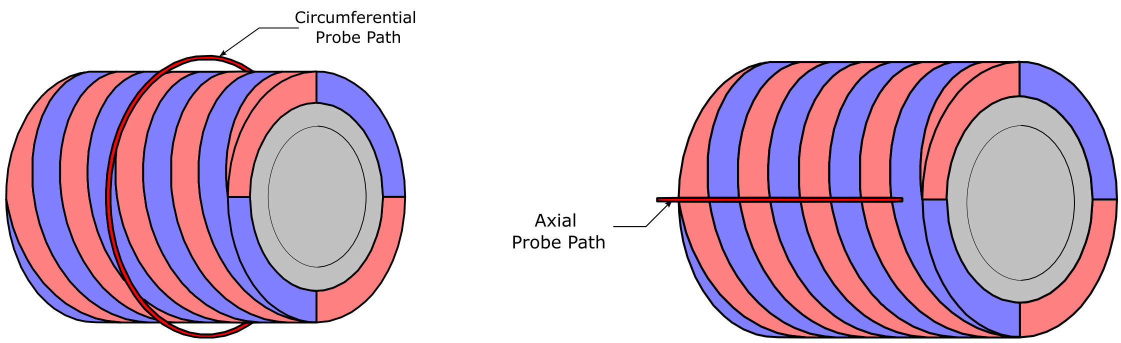

(a) (b)

Figure 4.9: Probe paths for the static magnetic field. (a) Circumferential path. (b) Axial path.

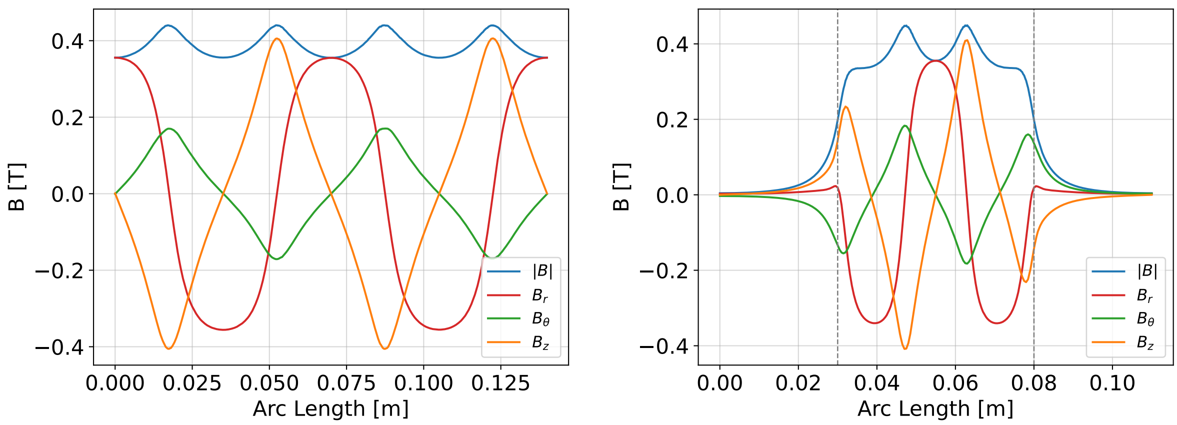

(a) (b)

Figure 4.10: Static magnetic field. (a) Along a circumferential path. (b) Along an axial path.

5 | FEM Modelling

Contents

In order to study - and later on characterize - the suspension described in the previous chapter, we need a model allowing us to compute the generated forces. Due to the helical pattern of the magnetic field and the considered guideway topology, the choice fell on modelling through finite element methods (FEM). This chapter therefore presents the models developed using the software COMSOL Multiphysics®.

First, the geometrical layout is described. Then, the general governing equations are presented. Subsequently, two different models were developed, named respectively Lorentz-based model (quasi-static) and rotating machinery model (time-dependent). Both rely on slightly different strategies, although fundamentally based on solving Maxwell's equations of electromagnetism. The assumptions and validity behind each model are then discussed, and they are compared based on their results and their computational efficiency.

An analysis on the impact of the mesh size and the convergence criteria regarding the size of the geometries is conducted in Appendix B.

5.1 Geometry

The considered geometry in a Cartesian coordinate frame (x,y,z) is shown in Figure 5.1. An illustration of the three types of domains - air, conductor, and PMs - is provided in Figure 5.2. Due to the helical arrangement of PMs, generating a three-dimensional magnetic field inside the air gap, and the absence of a plane of symmetry for the helix, the use of 3D finite element models is necessary.

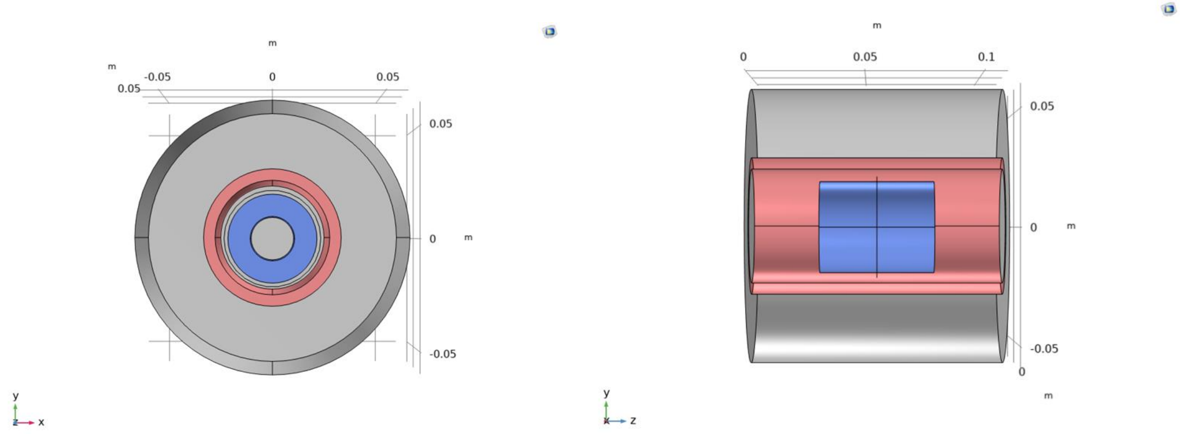

(a) (b)

Figure 5.1: Considered 3D FEM geometries. In blue, the HEDW. In red, the track. In grey, the air cylinder. (a) Front view. (b) Side view.

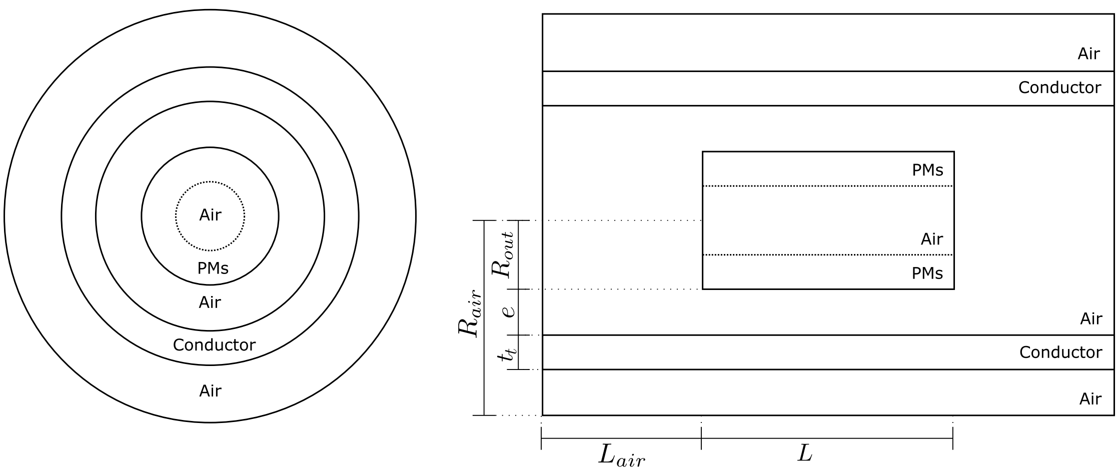

Figure 5.2: Considered 3D FEM domains.

The HEDW is embodied as a hollow cylinder of radius R_{out} and length L, where the thickness represents the PMs only. A mathematical formulation, further developed at the end of this section, is used to define the helical pattern of the suspension. A boundary condition on the inner surface can be applied to account for the effects of a ferromagnetic core, if required by the considered topology. This helps eliminate the need to mesh the core, an advantage given the costly computational nature of 3D FEM simulations.

Similarly, the track of thickness t_t is modeled as a second hollow cylinder placed around the wheel. Finally, a solid cylinder of radius R_{air} encloses the entire geometry to represent the air domain into which the magnetic field can close its path. This air domain needs to be sufficiently large in order not to interfere with or truncate the natural extension of the magnetic field, and thus preserve the physical accuracy of the simulation. Furthermore, the air cylinder must be longer than the wheel itself, in order to capture the end-effects of the suspension. A lateral space of L_{air} is thus cleared on both sides.

The magnetic and electrical properties of the different materials considered are summarized in Table 5.1.

Domain	Parameter	Value
Air	Electrical conductivity σ	$0\,[S/m]$
	Relative permeability μ_r	$1\,[-]$
	Relative permittivity ϵ_r	$1\,[-]$
Guideway Aluminum	Electrical conductivity σ	$3.774 \cdot 10^7\,[S/m]$
	Relative permeability μ_r	$1\,[-]$
	Relative permittivity ϵ_r	$1\,[-]$
PMs NdFeB 50	Remanent flux density B_r	$1.41\,[T]$
	Electrical conductivity σ	$0\,[S/m]$
	Relative permeability μ_r	$1.05\,[-]$
	Relative permittivity ϵ_r	$1\,[-]$

Table 5.1: Material properties used in the model.

5.1.1 Mathematical Formulation for the Helical Pattern

This subsection develops the mathematical formulation of an alternate surface mounted HEDW, applied to the PMs cylinder of the previously described geometry. As the dimensions (inner and outer magnet radius) are defined by the geometry, this formulation only maps the helical pattern onto this hollow cylinder without taking into account these boundaries.

This is achieved in three steps, in a cylindrical coordinate frame (r, θ, z). First, it starts by the definition of the poles at the start of the wheel, namely z = 0. Second, the advance and torsion of this section in the axial direction, such as to form a helix, are taken into account. Third, the repetitive nature of this helix in this longitudinal direction is added to the formulation.

1. Poles section at z = 0
The side view of the wheel at coordinate z = 0 (illustrated in Figure 4.2a), represents the number of pole pairs p and how they are distributed along the circumference. In an alternate topology, p pairs of pole actually mean $2p$ individual helices, each one of them representing an opening section of $\frac{2\pi}{2p} = \frac{\pi}{p}$ radians. Along this circumference, the coordinate θ thus encounters various poles, following the relation :

$$k\left(\frac{\pi}{p}\right) < \theta < (k+1)\left(\frac{\pi}{p}\right) \quad \text{for } k = 0, 1, \dots, (2p-1) \tag{5.1}$$

2. Torsion in z
The cross-sectional view defined previously at coordinate z = 0 is turning along the

axial z-direction to form the desired helical pattern. In other terms, this is equivalent to considering an angular offset $\Delta\theta$ at each infinitesimal cross-sectional area along this direction of advance :

$$k\left(\frac{\pi}{p}\right) < \theta + \Delta\theta < (k+1)\left(\frac{\pi}{p}\right) \quad \text{for } k = 0, 1, \ldots, (2p-1) \tag{5.2}$$

Where this angular offset is constraint by the axial pole pitch, such that we can write :

$$\Delta\theta = \frac{z}{\tau_z} \tag{5.3}$$

$$k\left(\frac{\pi}{p}\right) < \theta + \frac{z}{\tau_z} < (k+1)\left(\frac{\pi}{p}\right) \quad \text{for } k = 0, 1, \ldots, (2p-1) \tag{5.4}$$

3. Periodicity in z
The last step requires taking into account the periodicity of the helix in the longitudinal direction. This periodicity spacing is naturally governed by indexing a full angular offset $\frac{\pi}{p}$ to the previous equation :

$$k\left(\frac{\pi}{p}\right) < \theta + \left(\frac{z}{\tau_z}\right)\left(\frac{\pi}{p}\right) < (k+1)\left(\frac{\pi}{p}\right) \quad \text{for } k = 0, 1, \ldots, (2p-1) \tag{5.5}$$

This final equation can be expressed as a condition on the variable k, defining the polarity of each helix. Indeed, each material point of a given helix should belong to the same k parameter, which can be defined by using the floor function such as :

$$k = \left\lfloor \frac{\phi + \Delta\phi\left(\frac{\pi}{p}\right)}{\frac{\pi}{p}} \right\rfloor \tag{5.6}$$

Each helix magnetization direction is then defined given the value of the parameter k, modulated by the number of poles considered and the desired topology. The use of the modulo function allows to consider several pole pairs with the same expression, since the magnetization pattern is periodic along the circumference of the wheel. Therefore, the considered alternate surface mounted topology can be expressed as :

$$\begin{cases} +\hat{r}, & \text{if } (k \bmod 2) = 0 \\ -\hat{r}, & \text{if } (k \bmod 2) = 1 \end{cases} \tag{5.7}$$

5.2 Governing Equations

This section presents the governing equations, common to both of the models developed [38, 39].

Since the magnetic field is not fluctuating rapidly in time (the characteristic size of the system being much smaller than the electromagnetic wavelength), the magneto-quasi-static hypothesis is considered valid and the displacement current $\mathbf{D}$ can be safely removed from Maxwell's electromagnetic equations ($\frac{\partial \mathbf{D}}{\partial t} \approx 0$). The following subset of Maxwell's equations represent the governing equations to be solved, where $\mathbf{H}$ is the magnetic field intensity, $\mathbf{B}$ the flux density, $\mathbf{J}$ the current density and $\mathbf{E}$ the electrical field intensity.

$$\nabla \times \mathbf{H} = \mathbf{J} \tag{5.8}$$

$$\nabla \times \mathbf{E} = -\frac{\partial \mathbf{B}}{\partial t} \tag{5.9}$$

$$\nabla \cdot \mathbf{B} = 0 \tag{5.10}$$

$$\nabla \cdot \mathbf{J} = 0 \tag{5.11}$$

Introducing the magnetic vector potential $\mathbf{A}$ (MVP) and the magnetic scalar potential V (MSP), the equations for $\mathbf{B}$ and $\mathbf{E}$ can be formulated using these new variables :

$$\mathbf{B} = \nabla \times \mathbf{A} \tag{5.12}$$

$$\mathbf{E} = -\frac{\partial \mathbf{A}}{\partial t} - \nabla V \tag{5.13}$$

Using the constitutive relationship $\mathbf{B} = \mu_0(\mathbf{H} + \mathbf{M})$, where $\mathbf{M}$ is the magnetization vector, Ampère's law (Equation 5.8) becomes :

$$\nabla \times (\frac{1}{\mu_0} \nabla \times \mathbf{A} - \mathbf{M}) = \mathbf{J} \tag{5.14}$$

Using the vector identity $\nabla \times (\nabla \times \mathbf{A}) = \nabla(\nabla \cdot \mathbf{A} - \nabla^2 \mathbf{A})$ and the Coulomb gauge $\nabla \times \mathbf{A} = 0$, the previous equation can be expressed as :

$$\nabla^2 \mathbf{A} = -\mu_0 \mathbf{J} - \mu_0 \nabla \times \mathbf{M} \tag{5.15}$$

Within a conductive and moving material, Ohm's law constitutive equation for induced currents is expressed as :

$$\mathbf{J} = \sigma(\mathbf{E} + v \times \mathbf{B}) = \sigma(-\frac{\partial \mathbf{A}}{\partial t} - \nabla V + v \times (\nabla \times \mathbf{A})) \tag{5.16}$$

Substituting this into the previous equation leads to the magneto-quasi-static Poisson equation in its final form, allowing to model each domain of the geometry defined in Figure 5.2 :

$$\nabla^2 \mathbf{A} = -\mu_0 \sigma(-\frac{\partial \mathbf{A}}{\partial t} - \nabla V + v \times (\nabla \times \mathbf{A})) - \mu_0 \nabla \times \mathbf{M} \tag{5.17}$$

Table 5.2 summarizes the different simplifications and resulting equation for each domain, derived from Equation 5.17. Notably, the magnetization vector $\mathbf{M}$ is non-zero for the PMs only, where it defines the remanent flux density : $\mathbf{B_r} = \mu_0 \mathbf{M}$. Similarly, the electrical conductivity σ is non-zero for the guideway only, being the unique domain where induced eddy currents occur.

Domain	**Simplification**	**Final Poisson Equation**
Air	$\sigma = 0$, $\mathbf{M} = 0$	$\nabla^2 \mathbf{A} = 0$
PMs	$\sigma = 0$	$\nabla^2 \mathbf{A} = -\mu_0 \nabla \times \mathbf{M}$
Conductor	$\mathbf{M} = 0$	$\nabla^2 \mathbf{A} = -\mu_0 \sigma(-\frac{\partial \mathbf{A}}{\partial t} - \nabla V + v \times (\nabla \times \mathbf{A}))$

Table 5.2: Magneto-quasi-static equation : domains and simplifications.

Finally, magnetic insulation is applied at the boundaries of the surrounding air cylinder :

$$\hat{n} \times \mathbf{A} = 0 \tag{5.18}$$

The perfect magnetic conductor boundary, taking into account the ferromagnetic core, is developed according to the model used.

5.2.1 Forces, Torques and Powers

The forces and torques are evaluated in the Cartesian reference frame (x,y,z), as defined in Figure 5.3. The guidance force ($F_{guidance}$) is defined along the X-axis (red), the levitation force (F_{lift}) along the Y-axis (green) and the propulsion force (F_{thrust}) along the Z-axis (blue). Throughout this work, these colors will be respected.

Two approaches can be considered to compute these forces.

The first method relies on Lorentz's law, where the force is computed by integrating the cross product of the eddy current density $\mathbf{J}$ and the magnetic flux density $\mathbf{B}$ over the volume V of the conductive guideway :

$$\mathbf{F} = \int_V \mathbf{J} \times \mathbf{B} \, dV \tag{5.19}$$

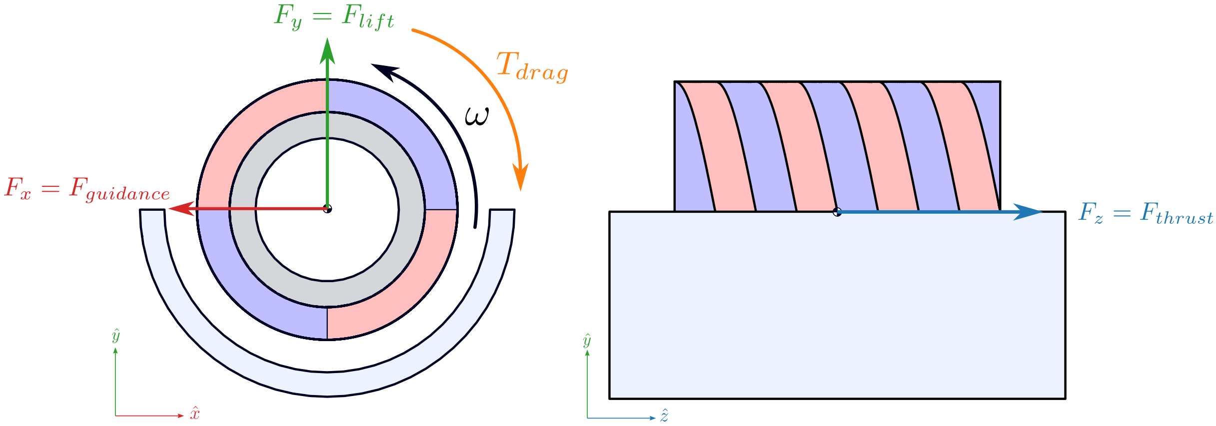

Figure 5.3: Forces in the Cartesian coordinate frame.

The alternative approach relies on the Maxwell's stress tensor $\mathbf{T}$, which provides the force acting on a body by integrating over a closed surface S that encloses it :

$$\mathbf{F} = \oint_S \mathbf{T} \cdot \hat{n} \, dS \tag{5.20}$$

where $\hat{n}$ is the outward normal vector to the surface. For this study case, both methods lead to the same results.

Figure 5.4 depicts the power flow of the considered system. The source electrical power P_{elec} is converted by the motor into mechanical power P_{meca} allowing the rotation of the wheel. By conservation of energy, this power serves two purposes.

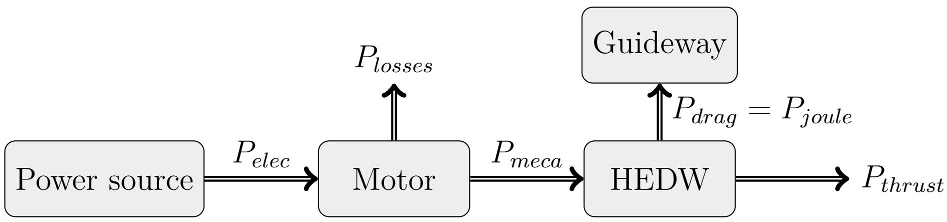

Figure 5.4: Power flow of the system.

First, the eddy currents in the guideway generate a drag torque T_{drag} (orange) on the wheel that tends to oppose its rotational movement ω. Power is therefore dissipated to counteract this torque and maintain the rotational speed set by the controller. This power is denoted P_{drag} or P_{joule} and can be expressed as :

$$P_{drag} = T_{drag} \, \omega = P_{joule} = \int_V \frac{|\mathbf{J}|^2}{\sigma} \, dV \tag{5.21}$$

Moreover, the drag torque can be defined as follows, where f_x and f_y are components of the force density :

$$T_{drag} = \int_V f_x \cdot y - f_y \cdot x \, dV \tag{5.22}$$

Second, the useful mechanical power used to propel the vehicle and overcome the aerodynamic drag forces acting on it, is defined as :

$$P_{thrust} = F_{thrust} \, V_T \tag{5.23}$$

where V_T is the speed of the pod.

5.3 Lorentz-based Model (Steady-State)

The first model developed to evaluate the forces is referred to as the Lorentz-based model. It uses exactly the geometry depicted in Figure 5.2, where it solves for the magnetic vector potential **A** and the electrical potential **E** across all domains. This model is restricted to steady-state studies, and is implemented in COMSOL Multiphysics® using the *Magnetic and Electric Fields* (MEF) interface.

From the used formulation, the perfect magnetic boundary condition at the interface between the PMs and ferromagnetic core is expressed as :

$$\hat{n} \times \mathbf{H} = 0 \tag{5.24}$$

The Lorentz-term $v \times \mathbf{B}$ from Equation 5.16 is used to define the currents resulting from the rotational and linear motion of the suspension, where each component of the speed in the reference Cartesian coordinate frame (x, y, z) must be explicitly set. Since Equation 5.16 is valid within conductive materials only, the motion is applied to the guideway whereas the electrodynamic wheel itself remains fixed. Illustration of the principle of the Lorentz-based model can be found in Figure 5.5.

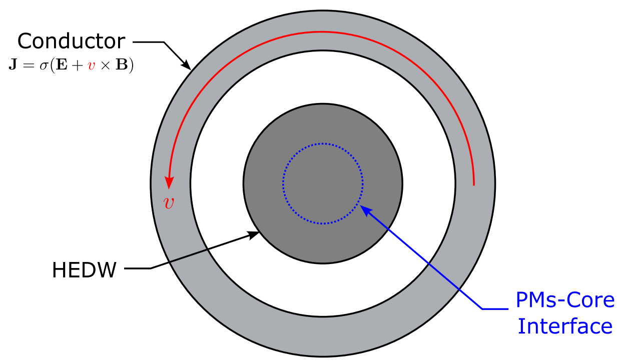

Figure 5.5: Lorentz-based model.

The velocity components are expressed with the following set of equations, where v_x and v_y together govern the rotation of each material point of the conductor. As defined in the previous chapter, V_T denotes the translational velocity of the system, or here the track. δ_x and δ_y denote the lateral and vertical displacement of the wheel.

$$\begin{cases} v_x = -\omega(y - \delta y) \\ v_y = -\omega(x - \delta x) \\ v_z = V_T \end{cases} \tag{5.25}$$

However, this Lorentz-based model relies on a key assumption. The source magnetic field (i.e., the PMs) must interact with the same image of unchanging distribution of the current density at all time (symmetric density). Intuitively, this hypothesis holds only when the wheel is centered in the guideway - because when a small displacement δ_x or δ_y from the nominal air gap e occurs, the air domain between both is deformed from a perfect circle, breaking the model's symmetry. This is illustrated in Figure 5.6. The deformation of the air gap increases as the displacement of the wheel becomes larger, therefore implying the validity of this model exclusively to centered conditions.

(a) (b)

Figure 5.6: Airgap deformation with displacement. (a) Centered. (b) Decentered.

The same effect is encountered when dealing with various opening angles of the track - where the source magnetic field sees alternating regions of currents and air - therefore limiting the use and physical accuracy of this model.

The main advantage of this model is its low computational cost ($\approx$ 60s), since the entities and meshes remain fixed and the problem is solved by introducing the Lorentz-term.

5.4 Rotating Machinery Model (Time-Dependent)

The rotating machinery model is based on a $\mathbf{A} - V$ formulation of the vector and scalar magnetic potentials. Initially intended for classic electromechanical motors or generators, this model allows only the rotational motion ω of the wheel, based on moving meshes, and thus no translational motion to occur. This model allows time-dependent simulations, where the motion of the rotor is taken into account in the boundary condition between the stator and rotor geometries. The model is illustrated in Figure 5.7, and is implemented in COMSOL Multiphysics® using the *Rotating Machinery Magnetic* (RMM) interface [40].

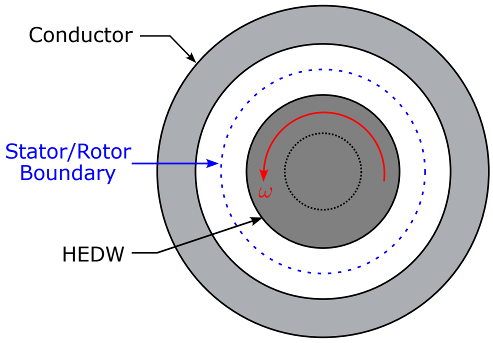

Figure 5.7: Rotating machinery model.

Within this model, the rotor and stator parts must therefore be defined as distinct assemblies, separated by a boundary. The advantage of this model is the possibility to rotate the suspension itself - and not the guideway compared to the Lorentz-based model, and thus capture accurately the behavior of a relative displacement of the wheel inside the track.

Figure 5.8 illustrates the boundary between the rotor (wheel) and stator (guideway), and how it evolves with displacements. The boundary can be tightened around the wheel to allow considerable relative displacements.

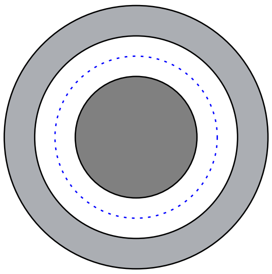

(a)

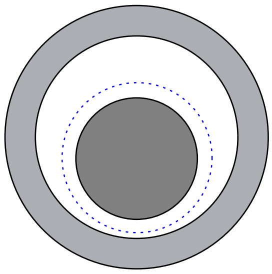

(b)

Figure 5.8: Stator/rotor boundary evolution with displacement. (a) Centered. (b) Decentered.

The rotor problem is solved in a rotating frame, in which the wheel remains fixed, whereas the stator problem is solved in the general non-moving Cartesian frame. Therefore, an interpolation between the two references takes place at the boundary interface, enforcing the continuity of the magnetic scalar potential V in the fixed stator frame.

Since no currents take place within the electrodynamic wheel nor the air gap, these domains are modeled using the conservation of the magnetic flux for nonconducting domains. Ampère's law is thus applied only to the guideway and the air beyond it - a mixed continuity condition between scalar and vector magnetic potential involved at the inner boundary of the track where both formulations meet. This is illustrated in Figure 5.9.

Using the magnetic scalar potential at the rotor/stator boundary ensures reduced numerical errors due to the interpolation between the nodes of the stator and rotor frames. The

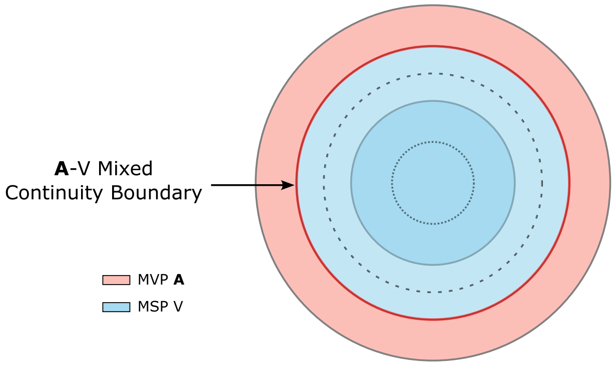

Figure 5.9: Mixed $\mathbf{A} - V$ continuity boundary.

current conservation of Ampère's law is violated using the magnetic vector potential at the boundary, resulting in a numerically unstable model [40].

From the used formulation, the perfect magnetic boundary condition at the PMs-core interface is expressed as a zero magnetic scalar potential :

$$V = 0 \tag{5.26}$$

Due to the moving meshes interfacing and time-dependent simulations, this model is computationally expensive - with simulations times starting at $\approx$ 1h and reaching up to one or two days.

5.5 Models Comparison and Discussion

This section compares the two considered models - the Lorentz-based model and the rotating machinery model - and their range of validity. In particular, the key hypothesis behind the Lorentz-based model is examined in details.

As a reminder, the Lorentz-term $v \times \mathbf{B}$ of Equation 5.16 is valid only if the source magnetic field (here, the PMs arrangement) interacts with a symmetric image of the current density in the conductor throughout the motion. When a relative displacement occurs in an enclosed track, the air gap is no longer a perfect circle - and the eddy currents density is higher in magnitude on the side where the gap is shorter. This difference in currents density increases further with a larger displacement. Therefore, both models should be equivalent only when the wheel and the track are coaxial (centered position).

Table 5.3 presents the resulting forces (in a Cartesian coordinate frame) and drag torque and the difference between both models when the suspension is centered. At this position, no guidance (F_x) and levitation (F_y) forces occur, because of the symmetry of the induced currents. The thrust force (F_z) is the only component generated, as well as the drag torque, due to the helical arrangement considered.

	Fx [N]	Fy [N]	Fz [N]	Tdrag [Nm]
Lorentz-based model	≈ 0	≈ 0	79.667	1.0396
Rotating machinery model	≈ 0	≈ 0	73.171	0.9632

Table 5.3: Comparison between the results of the Lorentz-based and rotating machinery models when the electrodynamic wheel is perfectly coaxial (centered) within a full (360° span) track.

The difference in thrust force could be explained by the non-convergence of the rotating machinery model. For this model, the size of the mesh is an important and penalizing parameter - but one that goes with an increase in computational time.
Keeping the conductor and PMs mesh sizes identical (extremely fine) and by incrementing the mesh size of the air domain separating the two geometries as depicted in Figure 5.10 by the hatched area, Figure 5.11 shows how the model does not reach convergence where the Lorentz-based formulation remains steady. The force still follows a linear increase, and a more refined mesh could not be made possible, due to simulation errors. The computational time for this model, although more robust theoretically, is more than ten time bigger than the Lorentz-based model.

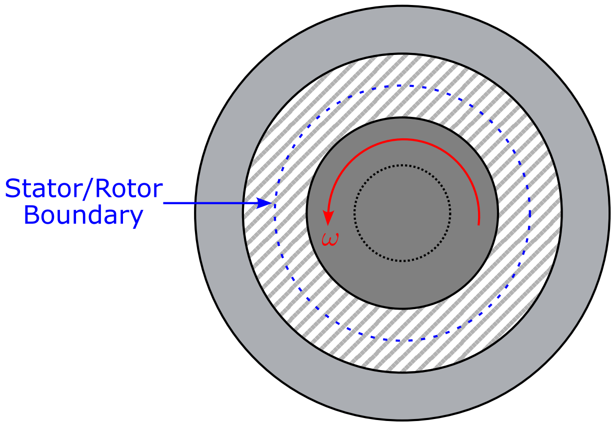

Figure 5.10: Domain of interest (hatched area, air gap) for the analysis of the impact of mesh size on the convergence of the rotating machinery model.

Figure 5.12 shows the evolution of the forces and the drag torque between both model when a displacement of the wheel is introduced. As expected, the difference increases as the displacement increases - reaching up to 25%. The initial offset for F_z and T_{drag} is the one noted previously.

Introducing an opening to the conductor, while keeping the suspension centered, removes part of the current density field from the source magnetic field point of view. Therefore, one should expect the same behavior as for the displacement to occur between both models, increasing with the opening. Comparison is made in Figure 5.13. While the force in the Y-direction seems to match closely between models, a difference is well noted for the other forces components and the drag torque.

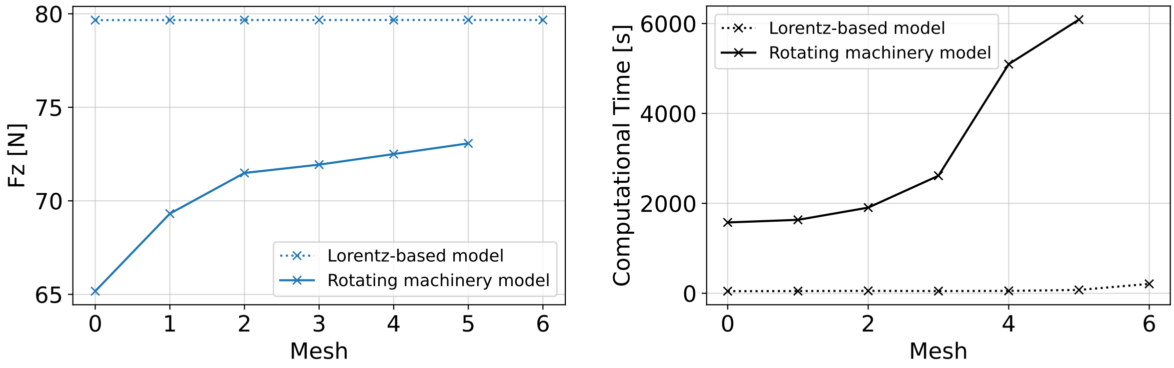

(a) (b)

Figure 5.11: Impact of the air gap mesh size on the convergence of the rotating machinery model. A high mesh value means a more refined mesh. (a) Thrust force. (b) Computational time.

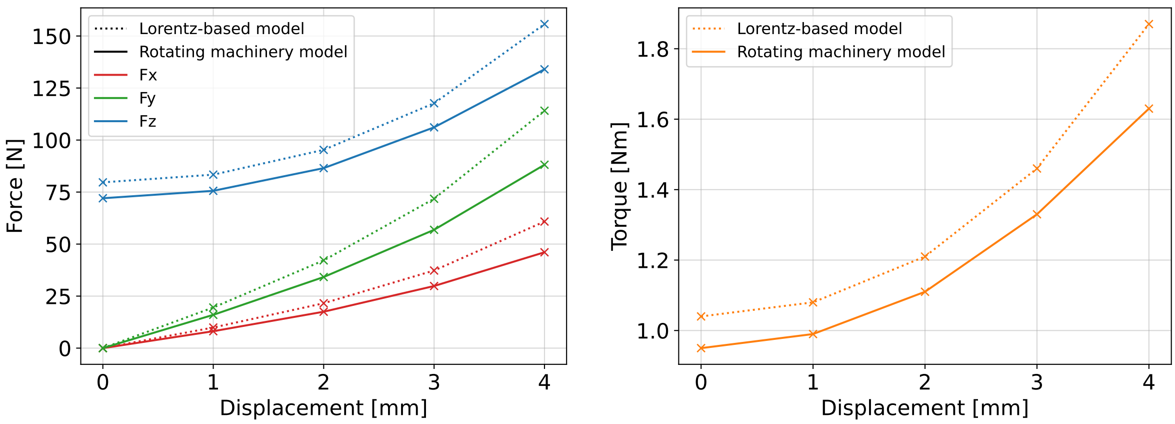

Figure 5.12: Difference between the Lorentz-based model and the rotating machinery model when a displacement of the wheel within the track is considered.

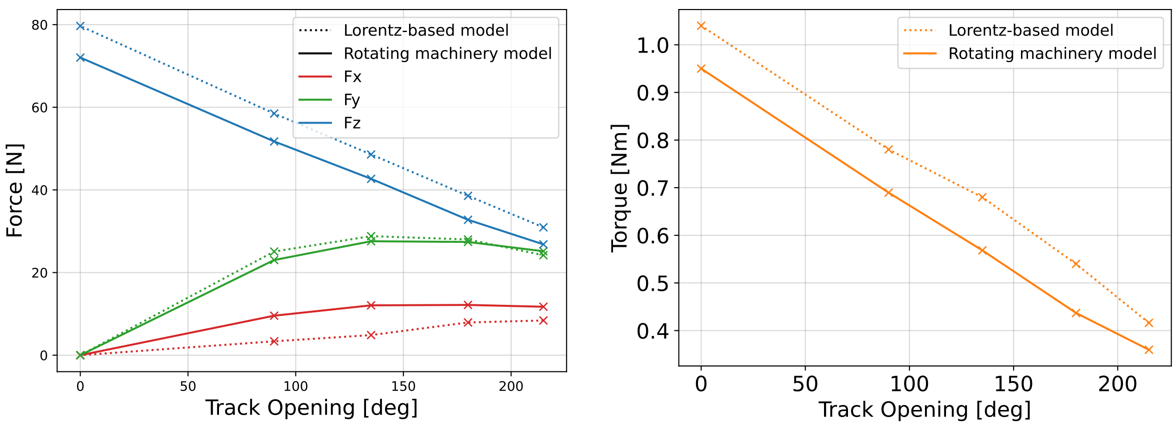

Figure 5.13: Difference between the Lorentz-based model and the rotating machinery model when an opening of the track is considered.

5.6 Conclusions

In this chapter, two 3D FEM models were envisaged - using two different strategies. The Lorentz-based model, as its name suggests, applies the $v \times \mathbf{B}$ of Equation 5.16 to the conductor domain. Since the three components of v must be explicitly defined in the chosen coordinate frame (here Cartesian), rotational and translational movements are possible. However, as this strategy is based on the assumption of a uniform current density in the track, the validity of the results is compromised when a relative displacement of the wheel or an opening in the conductor is considered.

The second model, although first intended for traditional motors or generators, relies on moving meshes between the rotor (the HEDW) and the stator (the track). Its advantage lies in the fact that the wheel can be rotated directly, making it physically accurate to move the wheel or open the track. As the model cannot be guaranteed to converge, because it depends exponentially on the mesh refinement, the results may present a certain offset. No translational motion is possible. Table 5.4 summarizes the characteristics of both models.

	Lorentz-based model	**Rotating machinery model**
Formulation	$\mathbf{A} - \mathbf{E}$	$\mathbf{A} - V$
Study type	Steady-state	Time-dependent
Frame	Fixed	Rotating
Moving domain	Conductor	HEDW
Translational motion	Yes	No
Displacements	No	Yes
Conductor opening	No	Yes
Converged	Yes	No
Computational time	≈ 60s, up to 5min	≈ 1h, up to 24h

Table 5.4: Characteristics of the Lorentz-based and rotating machinery models.

In the literature, different modelling strategies can be found regarding the prismatic EDW. Due to the wheel and flat guideway topologies, analytical models were studied alongside FEM ones. In particular, employment of an equivalent complex current sheet model for the source magnetic field allows spatial and time variations - therefore allowing a Lorentz-based model closer to reality [39, 41–43].

To some extent, the developed models allow a first study and characterization of the HEDW. For further researches and purposes, such as capturing a complete and accurate dynamical behavior, focus should be placed to more robust models. One model being considered is the PEEC (Partial Element Equivalent Circuit) model, an approach adapted to the study of currents induced in a conductor [44]. The main challenge at this level will lie in the application of this method, which is generally used in other fields, to the proposed problem.

6 | Characterization

Contents

The aim of this chapter is to characterize the proposed HEDW, based on the previously presented FEM models. The analyses focus on the evolution of the fundamental forces and drag torque generated, as well as on various performance criteria. These latter will be introduced in the first section.

This characterization mainly relies on parametric sweeps performed on the Lorentz-based model, due to its low computational cost and ability to take into account a longitudinal travel speed V_T. To remain in the validity assumptions of this specific model, the HEDW is evaluated with a small vertical displacement $\delta_y = 0.5mm$ (in order to generate lift and guidance forces), and a 360° conductive track. The rotating machinery model is used only to assess impact of large displacements δ_x, δ_y or the guideway opening angle β.

The first subset of analyses is based on the impact of dimensional parameters - such as the thickness of the track, or the radius, length, number of pole pairs, helical angle and magnet thickness of the wheel. Finally, the second subset of analyses is based on the effects of so-called mechanical or control variables. These include the rotational and longitudinal speeds, the displacements of the wheel or the track opening angle.

6.1 Performance Criteria

In a first approach, two ratios relate the three forces together. Among them, the lift-to-thrust ratio (LTR), that can be often found in the literature for the prismatic EDW, is defined as :

$$LTR = \frac{F_{lift}}{F_{thrust}} = \frac{F_y}{F_z} \tag{6.1}$$

The second ratio, the guidance-to-thrust ratio (GTR), is defined as :

$$GTR = \frac{F_{guidance}}{F_{thrust}} = \frac{F_x}{F_z} \tag{6.2}$$

These two performance criteria describe how the total amount of forces generated by a single wheel are distributed along the three directions of motion (guidance, lift and thrust).

In a subsequent approach, the drag torque T_{drag} is normalized by the outer magnet radius R_{out} to express an equivalent drag force :

$$F_{drag} = \frac{T_{drag}}{R_{out}} \tag{6.3}$$

With this drag force, performance criteria can now be introduced in relation to it, specifically the guidance-to-drag (GDR), lift-to-drag (LDR) and thrust-to-drag (TDR) ratios.

$$GDR = \frac{F_{guidance}}{F_{drag}} = \frac{F_x}{F_{drag}} \tag{6.4}$$

$$LDR = \frac{F_{lift}}{F_{drag}} = \frac{F_y}{F_{drag}} \tag{6.5}$$

$$TDR = \frac{F_{thrust}}{F_{drag}} = \frac{F_z}{F_{drag}} \tag{6.6}$$

For clarity, these three ratios will be associated to the specific colors corresponding to the concerned force (guidance in red, lift in green and propulsion in blue - as defined in Figure 5.3). Together, they provide insight on the efficiency of the considered suspension by quantifying how much of the desired forces are generated relative to the undesirable drag.

The final performance criterion relates the lift to the weight of the suspension. This lift-to-weight ratio (LWR) is defined as :

$$LWR = \frac{F_{lift}}{F_{weight}} = \frac{F_y}{F_{weight}} \tag{6.7}$$

The parameters of the reference candidate for this parametric characterization are summarized in Table 6.1.

Parameter	**Value**
Outer magnet radius R_{out}	$20mm$
Inner magnet radius R_{in}	$10mm$
Length L	$50mm$
Number of pole pairs p	2
Helical angle α	45°
Azimuthal pole pitch τ_θ	$31.416mm$
Axial pole pitch τ_z	$15.708mm$
Magnet ratio t_m	0.5
Nominal air gap e	$5mm$
Track opening angle β	0° (full track)
Track thickness t_t	$5mm$
Rotational speed ω	$1047rad/s$ ($10000rpm$)

Table 6.1: Parameters (primary and secondary) of the reference candidate for the parametric characterization of the suspension.

6.2 Dimensional Parameters

This section characterizes how the dimensional parameters affect the suspension. For each analysis, the variable of interest is swept between a lower and upper bound, whereas all the other primary parameters are kept constant.

6.2.1 Track Thickness

The conductor thickness must be sufficient in order not to truncate the induced currents generating the electrodynamic forces. By definition, the skin depth corresponds to the depth at which the amplitude of the eddy currents falls to approximately $\frac{1}{e} \approx 37\%$. Generally speaking, currents above this value no longer account for a significant change in the forces. In other words, the thickness t_t of the track should be greater than the skin depth δ, defined as :

$$\delta = \sqrt{\frac{2}{\mu\sigma\omega_e}} \tag{6.8}$$

Where μ is the magnetic permeability of the conductor, σ its electrical conductivity and ω_e the electrical pulsation of the field generated by the suspension. This electrical frequency is related to the wheel's mechanical angular speed ω and the number of pole pairs p via the relationship :

$$\omega_e = p\omega \tag{6.9}$$

As the rotational speed ω increases, the skin depth δ decreases and currents are more concentrated near the surface of the conductor. This is depicted in Figure 6.1. Additionally, to the skin depth, the diffusion angle of the induced currents increases with the speed and is a consequence of the longitudinal motion of the suspension.

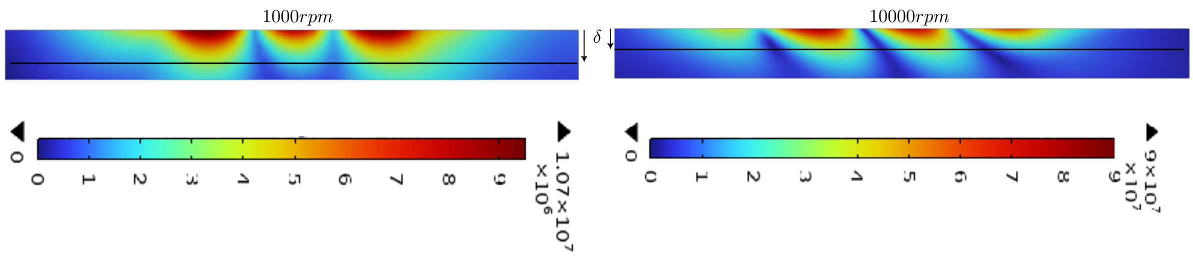

Figure 6.1: Skin depth difference with rotational speed. (a) 1000rpm. (b) 10000rpm.

In Figure 6.2, it is shown that all forces truly converge when the conductor thickness reaches two or three times the skin depth δ, or when the amplitude of the currents falls to $\approx$ 14% to 5%. Each vertical dotted line represents an increment in skin depth.

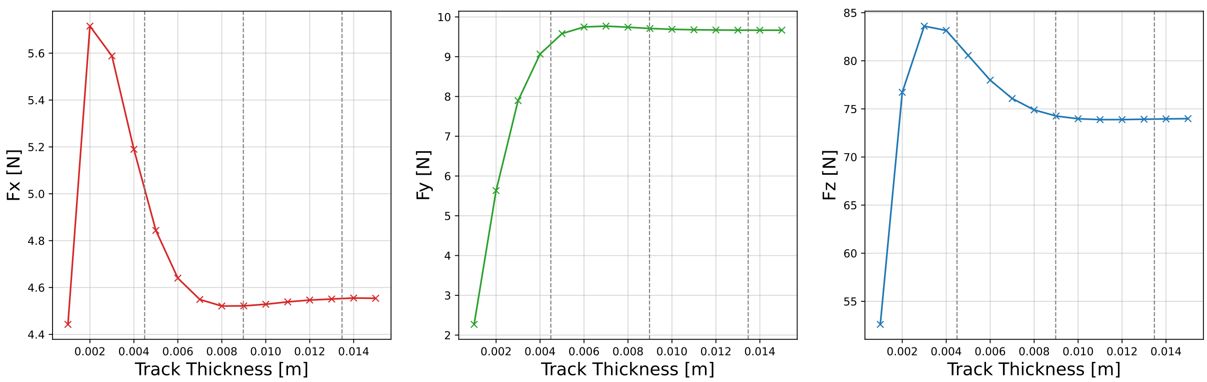

Figure 6.2: Evolution of the forces with regard to the track thickness. Each vertical dotted line represents an increment in skin depth.

6.2.2 Radius and Length

Radius

The impact of the outer magnet radius R_{out} is depicted in Figure 6.3. Since the magnet ratio t_m is kept constant, the inner magnet radius increases proportionally with the outer one. The greater the outer radius, the greater the forces generated. This can be attributed to two phenomena.

First, the increase in permanent magnets volume results naturally in a corresponding increase of the forces. Second, given Equation 4.4, with a constant number of pole pairs the azimuthal pole pitch τ_θ increases with the radius. A larger pole pitch reduces the frequency of the magnetic field (due to the greater distance between alternating magnetic poles), leading to a reduction in the skin effect and allowing a greater penetration of the currents into the conductor - and thus greater forces.

In terms of performance metrics, the lift-to-thrust ratio (LTR) increases, while the guidance-to-thrust ratio (GTR) decreases. This indicates that with a larger outer radius, more of the force generation is directed toward lift, whereas the relative contribution to guidance decreases.

The higher the forces generated, the higher the drag torque. Despite this, the three performance criteria related to drag (GDR, LDR and TDR) show a decreasing trend, suggesting that the suspension becomes less efficient. Indeed, more power is required to overcome the additional drag while maintaining the desired amount of forces levels.

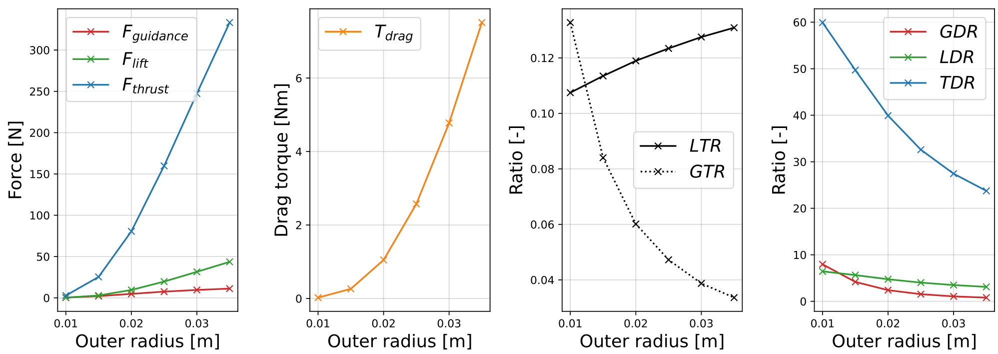

Figure 6.3: Impact of the wheel outer radius R_{out}.

As the magnet's volume increases, particular attention must be paid to the lift-to-weight ratio (LWR), since a ratio below one indicates that levitation cannot be assured. Figure 6.4 illustrates the evolution of the LWR. This latter increases, until it converges towards an upper bound, indicating diminishing gain in lift relative to the additional mass introduced.

Length

The impact of the wheel length is illustrated in Figure 6.5. The first row of subfigures depicts the absolute forces generated, while the second row presents these forces normalized by the length (force per unit length).

By the same principle as previously with the radius, the volume of permanent magnets increases with the length, which in turn proportionally increases the generated forces, as shown in the first subfigure.

However, for the proposed electrodynamic helical suspension, end-effects have been proven to be highly significant when the wheel is short. Ideally, a wheel of infinite length is

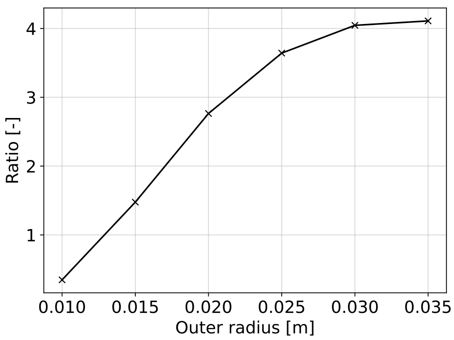

Figure 6.4: Lift-to-weight ratio (LWR) with regard to increase in outer magnet radius R_{out}.

preferable to eliminate these edge-related disturbances. This behavior is captured in the normalized forces subfigure, where the forces per unit length initially increase until converging towards a maximum value. Beyond this limit, each additional unit of length contributes linearly to the generation of forces.

In line with this trend, the lift-to-thrust (LTR) and guidance-to-thrust ratios (GTR) also converge towards stable values. This suggests that the share of guidance, lift and thrust remains constant for the given primary parameters (number of pair of poles and helical angle) as the wheel becomes longer.

The absolute drag torque increases proportionally with the wheel length. Nevertheless, since the normalized drag force also tends to a constant, the drag-related performance ratios (GDR, LDR and TDR) stabilizes at constant values.

As all ratios converge towards constant values as the wheel tends to be infinitely long, the lift-to-weight (LWR) likewise converges also, as shown in Figure 6.6. This reflects a balanced and scalable behavior of the system in relation to its length.

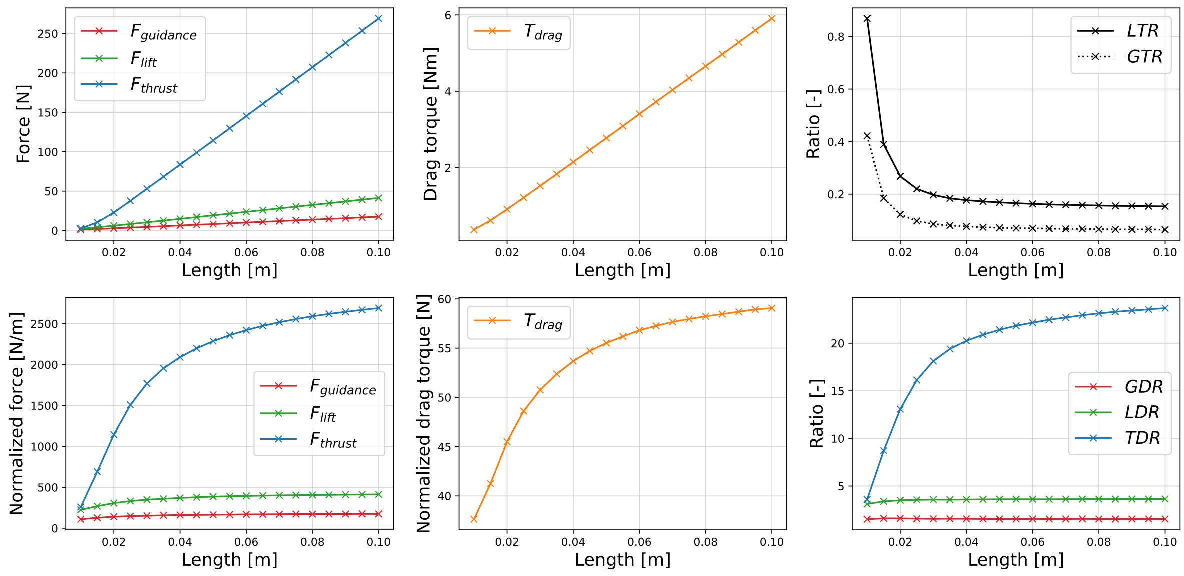

Figure 6.5: Impact of the wheel length L.

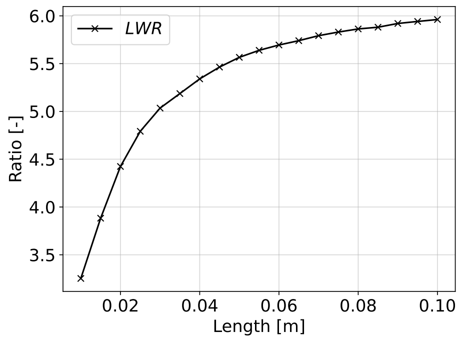

Figure 6.6: Lift-to-weight ratio (LWR) with regard to increase in wheel length L.

6.2.3 Pole Pairs and Azimuthal Pole Pitch

To assess the impact of the number of pole pairs p, it is important to note how this primary parameter influences both the azimuthal pole pitch τ_θ and the axial pole pitch τ_z. In this analysis, τ_z is kept constant. As a result, increasing p requires a corresponding decrease of $tan(\alpha)$, as expressed in Equation 4.5. Therefore, this implies an adjustment of the helical angle α accordingly.

Results of a parametric sweep over p are presented in Figure 6.7. The first row illustrates the evolution of the forces and corresponding performance criteria as a function of the primary parameter p, whereas the second row of subfigures describes these as a function of the secondary parameter τ_θ.

According to Equation 4.4, a smaller number of pole pairs leads to a larger azimuthal pole pitch. As discussed previously, a larger τ_θ increases the skin depth. This enhances current penetration into the track, and thus improves force generation.

The observed decrease in lift-to-thrust ratio (LTR) and guidance-to-thrust ratio (GTR) indicates that a larger share of the total force is being directed toward thrust. This is further reflected in the increasing trend of the thrust-to-drag ratio (GDR), indicating greater propulsion efficiency. In contrast, the lift-to-drag (LDR) and guidance-to-drag (GDR) ratios remain relatively stable.

Figure 6.8 highlights the existence of an optimum value for the azimuthal pole pitch τ_θ, beyond which the lift-to-weight ratio (LWR) is negatively impacted.

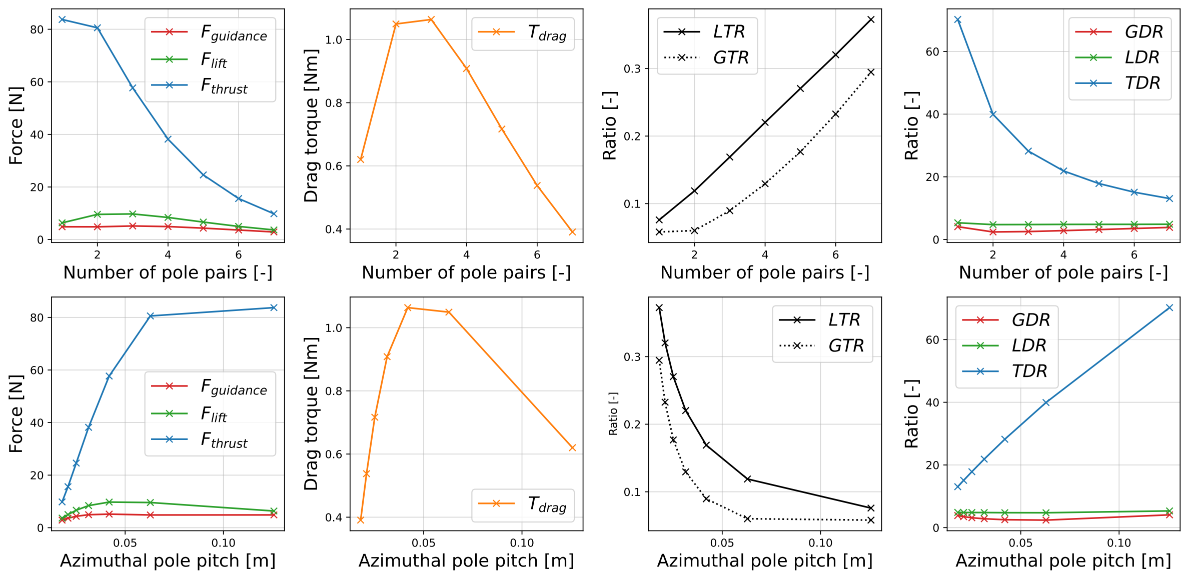

Figure 6.7: Impact of the number of pole pairs p (first row) and the azimuthal pole pitch τ_θ (second row).

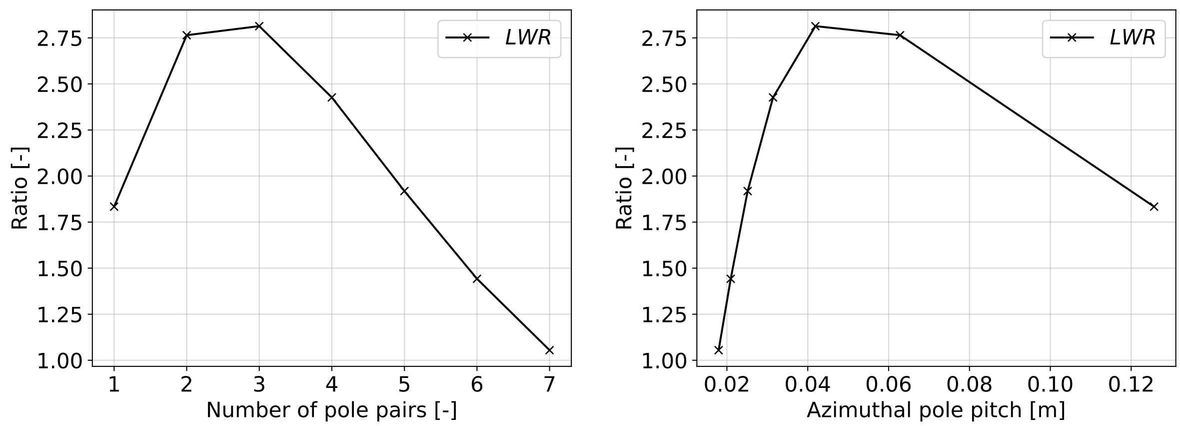

(a)

(b)

Figure 6.8: Evolution of the lift-to-weight ratio (LWR). (a) With respect to the number of pole pairs p. (b) With respect to the azimuthal pole pitch τ_θ.

6.2.4 Helical Angle and Axial Pole Pitch

The variation of the helical angle α is directly related to the axial pole pitch τ_z, as previously defined by Equation 4.5. The greater α, the more wound the helix, and thus the shorter the axial pole pitch τ_z. The impact of the helical angle is illustrated in the first row of Figure 6.9, whereas the influence of the axial pole pitch τ_z is represented in the second row of subfigures.

Similarly to the azimuthal pole pitch τ_θ, the greater the axial pole pitch τ_z, the deeper the eddy currents induced in the conductor. As the helical angle approaches 90°, meaning the helices are tightly wound around the core and that the axial pole pitch approaches zero (0° being the prismatic EDW), the forces decline toward negligible values, making these topologies inefficient. However, there exists an optimum value of α leading to a maximum in the thrust force. The evolution of this optimal angle with different magnet thicknesses and number of pole pairs is further investigated in Appendix C.

The final subfigures of Figure 6.9 highlight the presence of optimal operating points by the existence of a maxima for the thrust-to-drag ratio (TDR), and similarly a minimum for the lift-to thrust (LTR) and guidance-to-thrust (GTR) ratios. However, these extrema occur at different values of the helical angle α. Optimizing the helical arrangement involves trade-offs between maximizing the thrust efficiency and balancing the force distribution among guidance and lift.

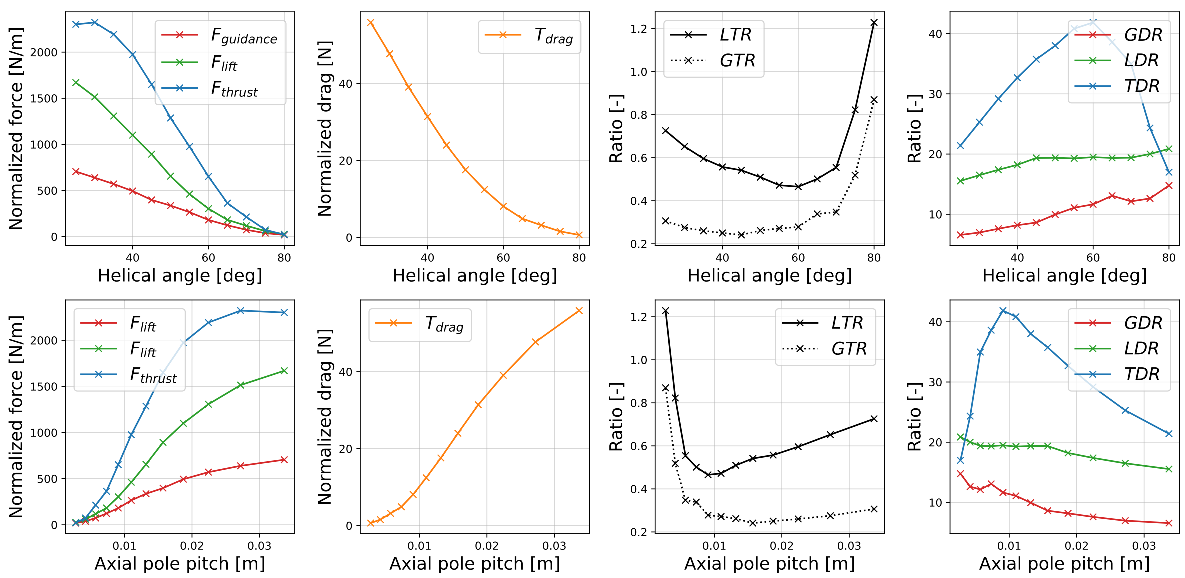

Figure 6.9: Impact of the helical angle α (first row) and the axial pole pitch τ_z (second row).

6.2.5 Magnet Thickness Ratio

The magnet thickness ratio t_m, defined as $\frac{R_{in}}{R_{out}}$, is a significant design variable determining the flux produced by the suspension. Moreover, this thickness ratio is directly linked to the weight of the wheel. With these two considerations, one should find the optimal thickness such as to maximize the lift-to-weight ratio LWR.

Figure 6.10 clearly depicts the existence of an optimal value for which the forces are maximum. While the guidance-to-thrust (GTR), lift-to-thrust (LTR), guidance-to-drag (GDR) and lift-to-drag (LDR) ratios keep increasing the more thin the wheel is, the thrust-to-drag ratio (TDR) reaches an upper bound. Figure 6.11 shows the existence of an optimum thickness for the lift-to-weight ratio (LWR).

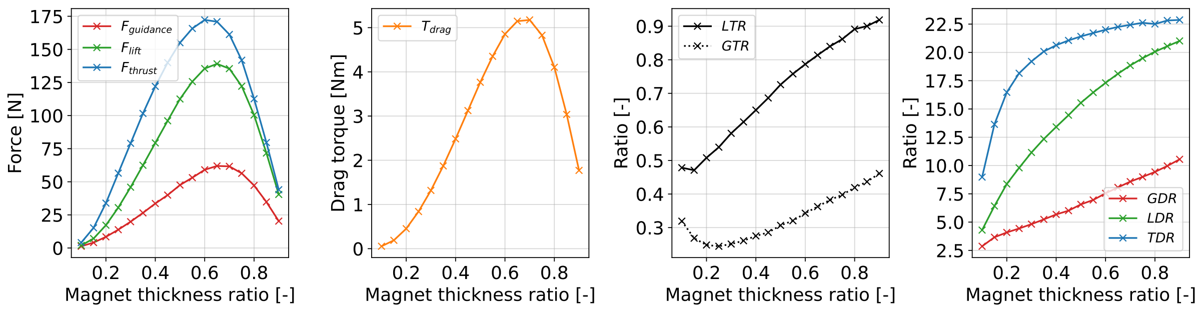

Figure 6.10: Impact of the magnet thickness ratio t_m.

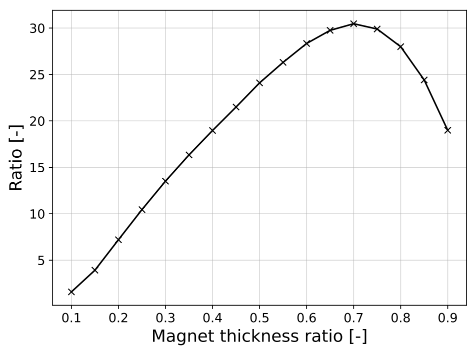

Figure 6.11: Lift-to-weight ratio with regard to the magnet thickness ratio t_m.

In his characterization of the prismatic EDW, J. Bird highlighted how this optimum thickness for the lift-to-weight ratio LWR increases with the number of pole pairs p. Additionally, the ratio between the azimuthal pole pitch τ_θ and the real thickness $R_{out} - R_{in}$ remains relatively constant across all values of p [5]. This ratio can be computed as:

$$\frac{\tau_\theta}{R_{out} - R_{in}} = \frac{\frac{2\pi R_{out}}{2p}}{R_{out} - R_{in}} = \frac{\pi}{p(1 - t_m)} \tag{6.10}$$

Table 6.2 depicts the results of this analysis for the HEDW.

Poles pairs p	2p	3p	4p
Optimum t_m for LWR	0.7	0.82	0.86
Ratio $\frac{\tau_\theta}{R_{out}-R_{in}}$	5.24	5.7	5.7

Table 6.2: Evolution of the optimum magnet thickness ratio t_m for the lift-to-weight ratio LWR.

6.3 Mechanical Variables

This section focuses on the impact of mechanical variables such as the rotational speed ω or the longitudinal travelling speed V_T of the suspension. Moreover, the impact of wheel displacements (δ_x, δ_y) in the track is investigated, as is the angular opening β of this latter. These parameters are the keys to the theoretical control of the vehicle.

6.3.1 Rotational Speed

The evolution of the absolute forces with the rotational speed ω is illustrated in Figure 6.12. This characteristic is similar to the one of traditional linear EDS, as shown in Figure 1.2.

The track can be assimilated to a RL circuit. At low speeds, the resistive impedance dominates - resulting in a linear increase of the forces with the speed. At some point, the inductive impedance of the track ωL dominates, damping the forces until they converge towards a stable value.

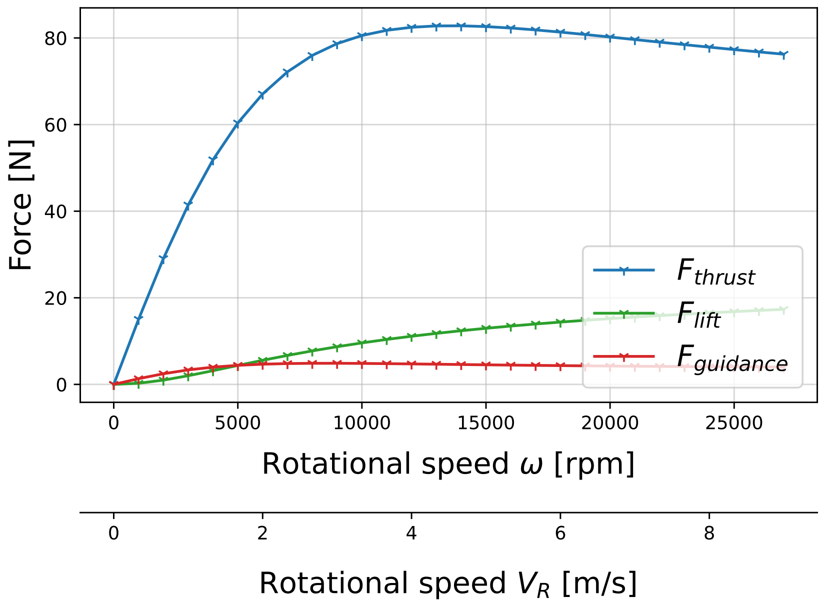

Figure 6.12: Evolution of the forces with the rotational speed ω.

6.3.2 Longitudinal Speed

The study of the impact of a longitudinal travelling speed V_T in the z-direction alongside the rotation ω of the suspension itself necessitates the introduction of the slip γ.

Similarly to asynchronous machines, the slip is defined as the normalized difference between the actual travelling speed V_T and a synchronous speed V_S. For the HEDW, this synchronous speed is related to the helical angle α and defined as :

$$V_S = V_R \, cot(\alpha) \tag{6.11}$$

Therefore, the expression for the dimensionless slip γ is :

$$\gamma = \frac{V_S - V_T}{V_S} = \frac{V_R \, cot(\alpha) - V_T}{V_R \, cot(\alpha)} \tag{6.12}$$

The evolution of the forces is illustrated in Figure 6.13. Theoretically, as the slip tends towards $\gamma = 0$, the pod travels at synchronous speed and there is no relative motion of the magnetic field anymore - therefore no induced currents and thus no forces. Nevertheless, the circumferential speed V_R is defined with regard to the physical radius of the wheel, but the effective radius (from the center of the suspension to the skin depth of the eddy currents in the track) is greater. This concept is similar to a paddlewheel, and explains the shift of the zero forces point towards a slightly lower slip value. The greater the nominal air gap e, the greater this offset will be. The difference between the radius of the wheel and the considered radius of action of the track is illustrated in Figure 6.15.

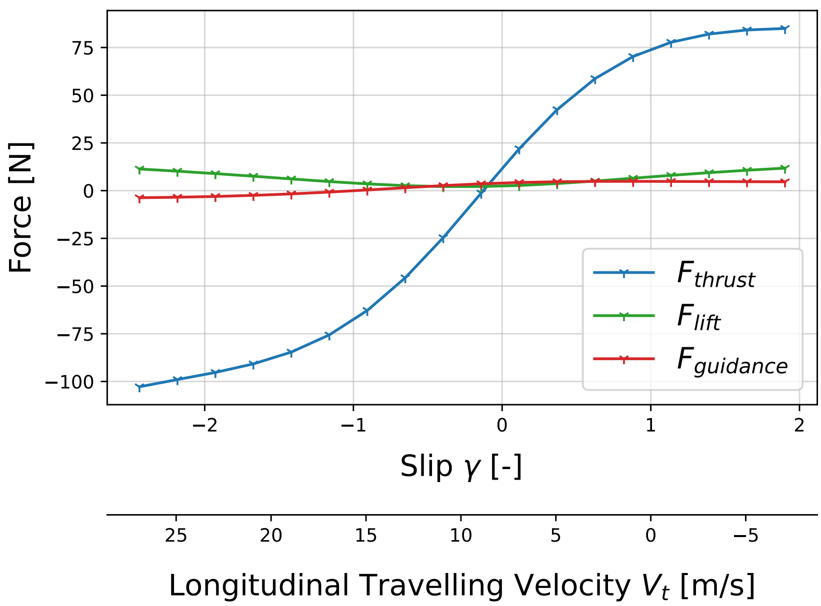

Figure 6.13: Evolution of the forces with the slip γ.

As the slip becomes negative, the relative motion of the travelling magnetic field is reversed, changing the directionality of the guidance force.

The continuing decrease of the thrust force at negative slips (beyond $\gamma = -2$) is due to the end-effects of the suspension. An infinitely long wheel would converge towards upper and lower bounds. This impact is shown in Figure 6.14, where the thrust force has been normalized by the length.

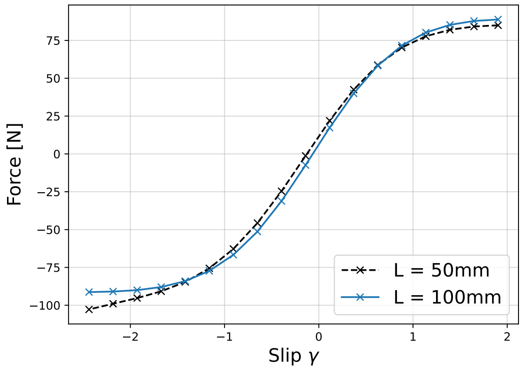

Figure 6.14: Impact of the end-effects on the thrust force.

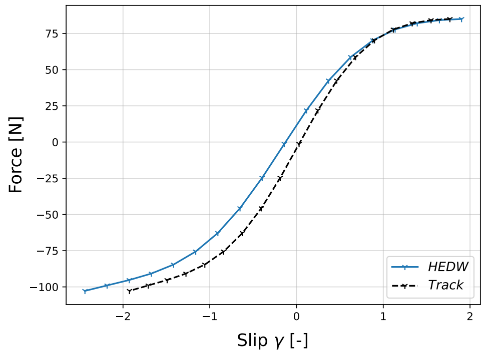

Figure 6.15: Paddlewheel effect : offset of the zero-force crossing on the considered radius of action.

6.3.3 Displacements

The evolution of the fundamental forces and drag torque with displacements inside the track is assessed based on the rotating machinery model, capturing more effectively the phenomenon. Since this model relies on time-dependent simulations, the average value over a period has been taken to constitute the following figures.

The impact of a displacement δ_x is illustrated in Figure 6.16 for a 180° track. Due to the directionality of the guidance force, this latter is the source of dynamical instabilities. If the wheel is decentered towards the opposite direction of the guidance force, the force increases and tends to bring back the wheel to its centered position. This behavior is typical to a positive stiffness and to traditional EDS.

However, if the wheel is decentered towards the initial direction of the guidance force, the resulting opposing force must first cancel the initial guidance before pushing the wheel back. This principle is shown in Figure 6.17. Until a large enough shift, the guidance force suffers from a negative stiffness - a positive displacement results in a force in that direction, although smaller.

The levitation force suffers from the same directionality with respect to the guidance : when one increases, the other decreases. The dynamical analysis in the next chapter will focus on the consequences of this behavior.

The thrust force and drag torque, however, depict symmetrical trends with regard to the centered position. Both increase with the lateral displacement, no matter the direction.

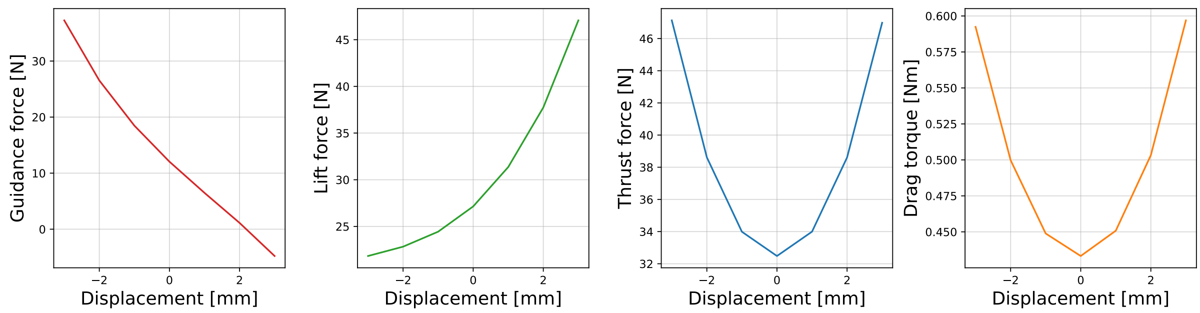

Figure 6.16: Impact of lateral displacements δ_x.

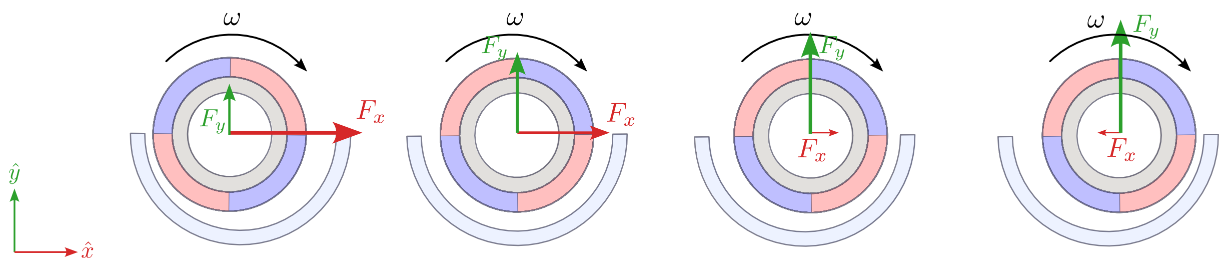

Figure 6.17: Evolution of the guidance and lift forces with lateral displacements.

The evolution of the forces for a vertical displacement δ_y is illustrated in Figure 6.18. When the air gap decreases (when δ_y is negative), all the forces and drag torque increase. When the wheel is moved towards the opening of the track (positive δ_y), all forces decrease.

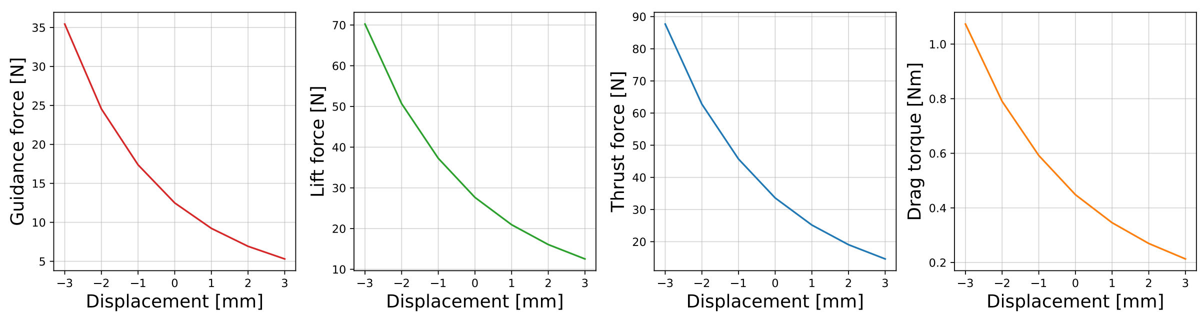

Figure 6.18: Impact of vertical displacements δ_y.

6.3.4 Track Opening

The evolution of the forces and drag torque with the track opening angle β is depicted in Figure 6.19. As this analysis is based on the time-dependent rotating machinery model, the first few seconds of the simulation relates to the transient. Table 6.3 summarizes the average value of these time-dependent simulations.

An opening in the track introduces periodic oscillations in the guidance and levitation forces, caused by the periodic contact of the peaks of the static magnetic field (shown in Figure 4.10a) with the edges of the conductor.

The 145°, 180° and 225° guideways converge towards close values for the guidance and lift forces - but depict different amplitudes of oscillations over time. As the conductor spans a larger angle (close to 360°), this tends to impact negatively both forces - because induced currents belonging to the superior half circle of the track cancel the forces generated by the lower half.

The thrust force and drag torque decrease as the opening angle increases. The more volume of conductive material, the bigger the thrust and drag.

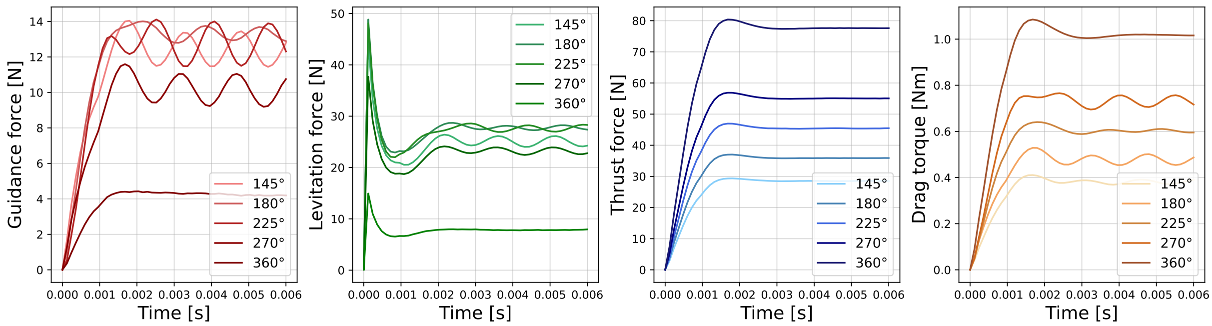

Figure 6.19: Evolution of the forces and drag torque with the track opening β (time-dependent simulations).

Opening angle	Fx [N]	Fy [N]	Fz [N]	Tdrag [Nm]
145°	11.6802	25.0239	26.7109	0.3582
180°	12.4911	27.6519	33.5928	0.4482
225°	12.0129	27.4475	42.5047	0.5659
270°	9.5282	22.9197	51.5159	0.6864
360°	4.84	9.958	80.56	1.05

Table 6.3: Evolution of the forces and drag torque with the track opening β (average values of the time-dependent simulations).

6.4 Conclusions

This chapter studied and characterized the evolution of the forces and various performance criteria with respect to dimensional and mechanical parameters.

A first observation is the importance of the generated thrust force compared to the lift and guidance forces, making the HEDW an effective propulsion device - and there exists an optimum value of the helical angle α for which this thrust force is maximum. Furthermore, the characterization highlighted the influence of end-effects, notably related to the length of the wheel. The ideal HEDW, as mentioned in [11], is of infinite length - but practically infeasible.

The greater the pole pitches, the greater the forces. However, there exist an optimum value for the azimuthal pole pitch τ_θ with respect to the lift-to-weight ratio (LWR), beyond which this latter is degraded. Similarly, the magnet thickness ratio t_m has a significant role on the generated flux and mass of the system, resulting in an optimum value for the LWR. Following this characterization, real optimization within the framework of a specific case study would enable the optimal values for the various dimensional parameters of the wheel to be obtained.

Regarding the mechanical variables, the linear zone of the thrust force with respect to the travelling velocity V_T $(-1 < \gamma < 1)$ represents the range of interest for the control of the pod. The dynamical instabilities related to the guidance force with lateral displacements δ_x is further investigated in the next chapter. The volume of conductive material is tightly related to the amount of thrust force and drag torque, an observation made with the impact of the opening angle β of the track.

Additional figures regarding the characterization of the suspension are provided in Appendix C. A short sensitivity analysis was investigated in Appendix D.

7 | Dynamical Analysis

Contents

The aim of this chapter is to provide a first insight into the dynamical behavior of a pod equipped with four HEDWs. As illustrated in Figure 3.2, these wheels are placed in sets of two in parallel tracks on either side of the capsule. Each of them is supposed to have its own driving motor, and are thus independent.

This pod, assimilated to a free body in the air, has thus six degrees of freedom (DoFs): three translational motions (guidance in $\hat{x}$, levitation in $\hat{y}$ and thrust in $\hat{z}$), along with three rotational motions around these axis (respectively the pitch Θ, yaw Ψ and roll Φ). These DoFs are illustrated in the Cartesian reference frame in Figure 7.1a. First, the steady-state equilibrium conditions to keep the pod centered and stationary (while still achieving levitation) will be stated.

Subsequently, the dynamical analysis will be divided into two parts. At first, the lateral behavior of two wheels placed in different tracks will be analyzed, as represented by the purple cross-sectional plane in Figure 7.1b. This analysis, not involving a longitudinal travel speed V_T along the z-direction, will be based on the rotating machinery model capturing more effectively displacements phenoma. The considered track as an opening angle β of 180°.

Then, the longitudinal behavior, this time involving a travel speed V_T, will be analyzed with two wheels placed in series in a unique track, as framed by the green plane in Figure 7.1b. Since the rotating machinery model does not allow such longitudinal speed

V_T, this analysis will be conducted on the results of the Lorentz-based model.

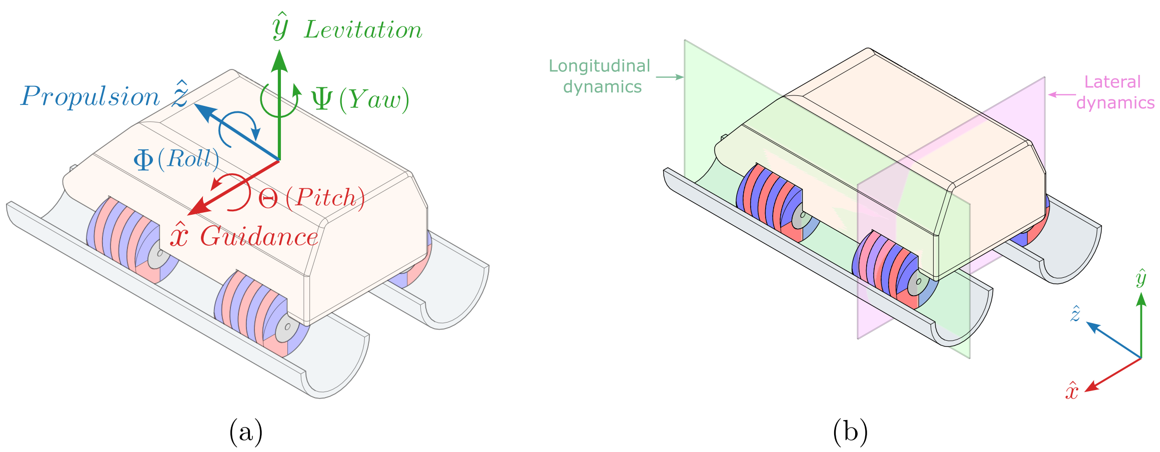

Figure 7.1: References for the dynamical analysis of the pod. (a) Coordinate frame. (b) Cross-sectional (purple) plane for the lateral analysis and longitudinal plane (green) for travel speed V_T analysis.

7.1 Steady-State Stability

7.1.1 Stability Regarding Guidance

Among the three forces generated by the HEDW (guidance, lift and thrust), the direction of the guidance and thrust forces depends on the rotational direction of the wheel.

Therefore, to achieve steady-state equilibrium regarding the guidance force, each pair of wheels in independent tracks must rotate in opposite directions, as represented in Figure 7.2. The relative direction of rotation of the left and right wheel is not significant for lateral stability, as long as they are opposite.

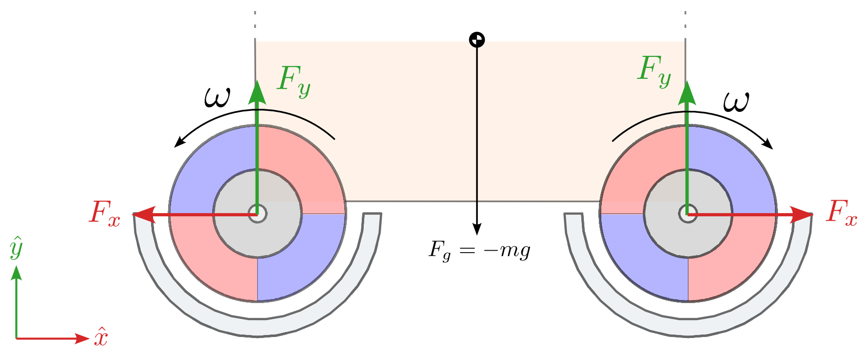

Figure 7.2: Condition for steady-state stability of the guidance force : wheelsets in different track must rotate in opposite direction.

Furthermore, as analyzed in subsection 6.3.3, the guidance force is subject to dynamical instabilities when a displacement δ_x occurs in the same direction as that force when the wheel is centered, and for a 180° track. When the pod veers sideways, the guidance force is not assured to reverse direction and have enough magnitude in order to push the wheel back to its centered position.

To help ensure stability in the case of a 180° conductor, the guideway can be inclined by an angle ϕ from one section of track to another, as illustrated in Figure 7.3. The left schematic represents the reference configuration modeled in COMSOL Multiphysics®, where the guidance and lift forces are respectively aligned with the y and x-axis in the Cartesian coordinate frame. Introducing the terms of parallel $F_{//}$ and perpendicular $F_{\perp}$ forces - aligned with the lift $F_{lift} = F_y = F_{//}$ and the guidance $F_{guidance} = F_x = F_{\perp}$ in the COMSOL reference model - we are able to compute resulting F_x and F_y forces for an inclined track with the help of a rotation matrix around the z-axis :

$$\begin{bmatrix} F_x \\ F_y \end{bmatrix} = \begin{bmatrix} cos(\phi) & -sin(\phi) \\ sin(\phi) & cos(\phi) \end{bmatrix} \begin{bmatrix} F_{\perp} \\ F_{//} \end{bmatrix} \tag{7.1}$$

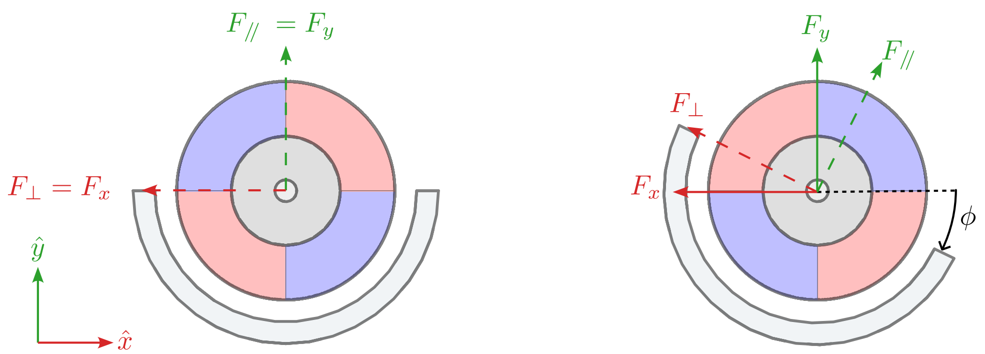

Figure 7.3: Inclination of the track to achieve positive stiffness regarding the guidance force. (a) COMSOL Multiphysics® reference configuration, where $F_{//}$ is aligned to F_y and $F_{\perp}$ is aligned to F_x. (b) Inclined track of an angle ϕ.

To achieve positive stiffness for F_x, we would like it to change sign - so that a displacement δ_x induces a negative repelling force in the opposite direction. However, we would like for F_y to not change sign. As a result, the magnitude of the forces are also impacted.

The minimum track tilt angle is therefore given by :

$$F_x = 0 \Rightarrow \phi = tan^{-1}\left(\frac{F_{\perp}}{F_{//}}\right) \tag{7.2}$$

7.1.2 Stationary Levitation

To remain stationary while still achieving levitation, a first approach would be to impose the wheels in independent tracks to turn in different directions, as to cancel thrust forces, such as illustrated in Figure 7.4a. However, in this configuration, these thrust forces result in a yaw Ψ motion around the y-axis. To avoid this phenomenon, each set of wheels in series must rotate in opposite directions - while maintaining the condition that the mirror wheel in the parallel track also rotates in an opposite direction to cancel unwanted guidance forces. This stable configuration is depicted in Figure 7.4b.

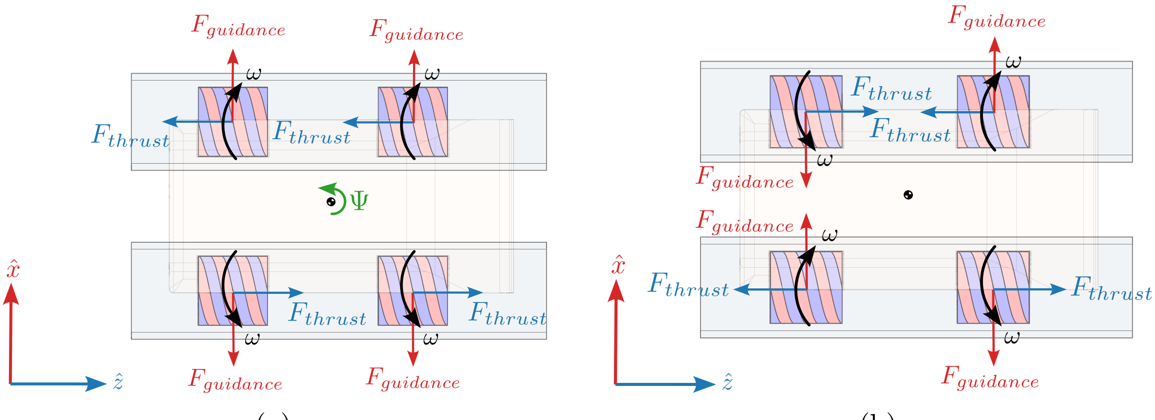

Figure 7.4: Equilibrium conditions for stationary levitation, based on the direction of rotation of the four wheels independently. (a) Thrust forces inducing a yaw movement. (b) Equilibrium.

7.2 Lateral Dynamics

The lateral dynamics is analyzed in the purple cross-sectional xy-plane represented in Figure 7.1b. In this plane, only the levitation and the guidance can be framed, along with the roll Φ around the z-axis. Denoting the forces generated by the left and right wheels with L and R respectively, the set equations of motion are thus :

$$\begin{cases} m\frac{d^2x}{dt^2} = F_{x,L} + F_{x,R} \\ m\frac{d^2y}{dt^2} = F_{y,L} + F_{y,R} - mg \\ I_r\frac{d^2\Phi}{dt^2} = (F_{y,L} - F_{y,R})\frac{D}{2} \end{cases} \tag{7.3}$$

Where m is the total mass of the pod, and I_r the roll inertia. D denotes the lateral distance between the center of both wheels in separated tracks.

Based on the rotating machinery model, the forces acting on a single wheel can be computed given its position (δ_x, δ_y). Knowing that the direction of the guidance and thrust forces are reversed when rotating in opposite direction, the forces for the second wheel can be computed from the first's model as :

$$\begin{cases} F_{x,R}(\delta_x, \delta_y) = -F_{x,L}(-\delta_x, \delta_y) \\ F_{y,R}(\delta_x, \delta_y) = F_{x,L}(-\delta_x, \delta_y) \end{cases} \tag{7.4}$$

For the following simulations, the mass m was determined such as to achieve stable levitation when the two wheels are centered and coaxial with their guideway. A small disturbance is applied, either in the y or x-direction.

7.2.1 Vertical Displacements

The positive stiffness of the levitation force results in an undamped mass-spring system when a displacement δ_y occurs. When the pod is pushed down, the air gap decreases and the force F_y increases. This force carries the pod beyond the centered equilibrium position, where the force F_y decreases and thus initiate an oscillatory movement. The guiding forces always compensate and cancel each other out, resulting in a purely vertical movement. This evolution of the position is illustrated in Figure 7.5.

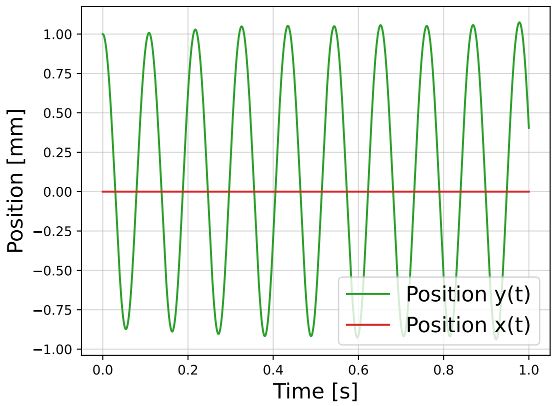

Figure 7.5: Evolution of the x and y position of the pod over time when both wheels are subject to an initial perturbation $\delta_y = 1mm$.

7.2.2 Lateral Displacements

The force distribution when a displacement δ_x occurs is represented in Figure 7.6. Due to the directionality of the guidance force F_x, asymmetry in the resulting forces arises. The resulting guidance force is such that the pod is pushed back towards the center, but the difference in lift forces induces a roll motion given Equation 7.3. As for the previous case, the guidance is subject to an undamped mass-spring system. This evolution of the position is illustrated in Figure 7.7.

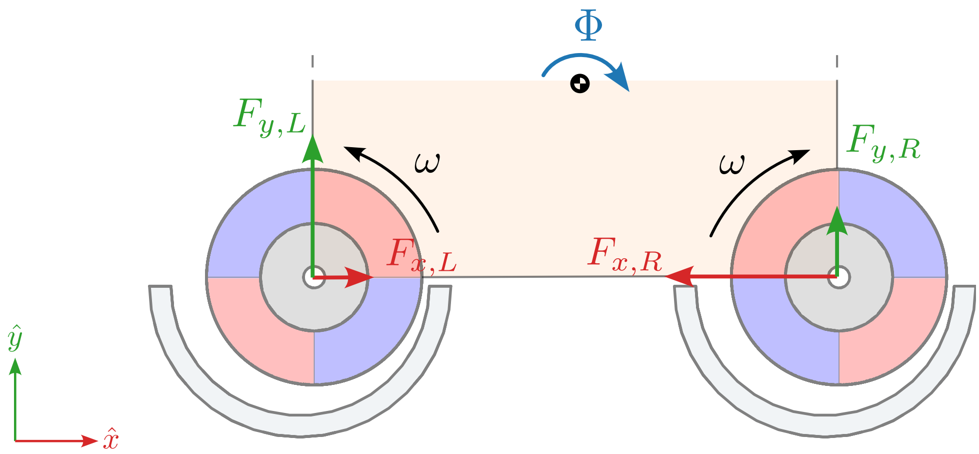

Figure 7.6: Distribution of the forces when the pod is subject to a displacement δ_x. The asymmetry in lift forces leads to a roll motion of the vehicle.

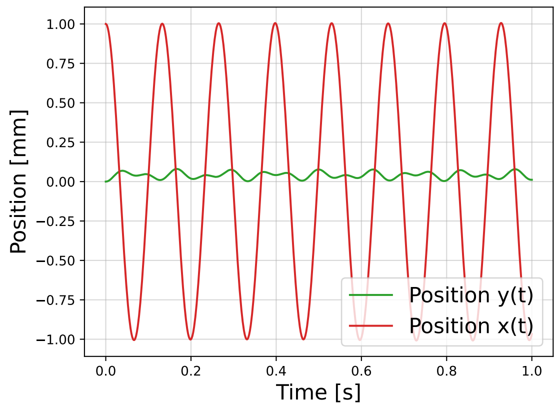

Figure 7.7: Evolution of the x and y position of the pod over time when both wheels are subject to an initial perturbation $\delta_x = 1mm$.

7.3 Longitudinal Dynamics

The longitudinal dynamics is analyzed in the green yz-plane depicted in Figure 7.1b. In this plane, only the levitation and the propulsion can be framed, along with the pitch motion Θ around the x-axis. Once again denoting the forces generated by the left and right wheels with L and R respectively, the set equations of motion are :

$$\begin{cases} m\frac{d^2y}{dt^2} = F_{y,L} + F_{y,R} - mg \\ m\frac{d^2z}{dt^2} = F_{z,L} + F_{z,R} - \frac{1}{2}\rho C_D A V_T^2 \\ I_p\frac{d^2\Theta}{dt^2} = (F_{y,L} - F_{y,R})\frac{D'}{2} \end{cases} \tag{7.5}$$

where D' denotes the longitudinal distance between the centers of both wheels and I_p the pitch inertia. The second term in the forward equation of movement represents aerodynamic drag, for which ρ denotes the air density, C_D a drag coefficient and A the reference front area of the pod.

7.3.1 Acceleration and Deceleration

To achieve a forward movement, both wheels in the same track must rotate in the same direction. This analysis focuses on the impact of applying a positive or negative differential speed $\Delta\omega$ to the wheelset, as illustrated in Figure 7.8.

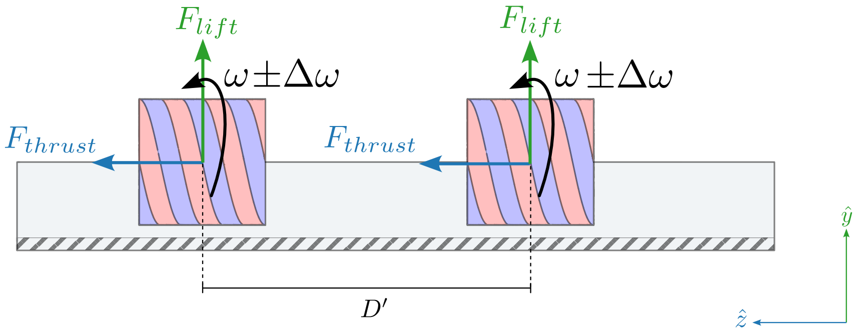

Figure 7.8: Reference configuration for the longitudinal dynamical analysis.

When both suspensions rotate at the same speed ω, the pod accelerates until it reaches a constant travelling speed V_T. Both wheels provide the same magnitude of thrust and lift, stabilized at a given slip γ, as defined previously with regards the synchronous speed.

In order to accelerate or decelerate, both wheels must respectively increase or decrease their rotational speed by a term $\Delta\omega$. Figure 7.9 illustrates the evolution of the speed and the lift forces for an acceleration occurring at t=2s.

At start-up, the slip $\gamma = 1$. As the speed increases, this slip decreases towards the synchronous speed ($\gamma = 0$). As seen in the characterization, as we near this synchronous speed, the relative movement between the HEDW and the track decreases, also leading to a decrease in the forces produced. When the rotational speed ω increases, the slip increases again to stabilize at a higher value given the new cruising speed V_T. Therefore, more lift is generated.

In the deceleration scheme, the reasoning is reversed and the levitation forces decrease. Evolution of the slip and lift force for an acceleration and deceleration cases are represented in Figure 7.11. The evolution of the speed is depicted in Figure 7.10.

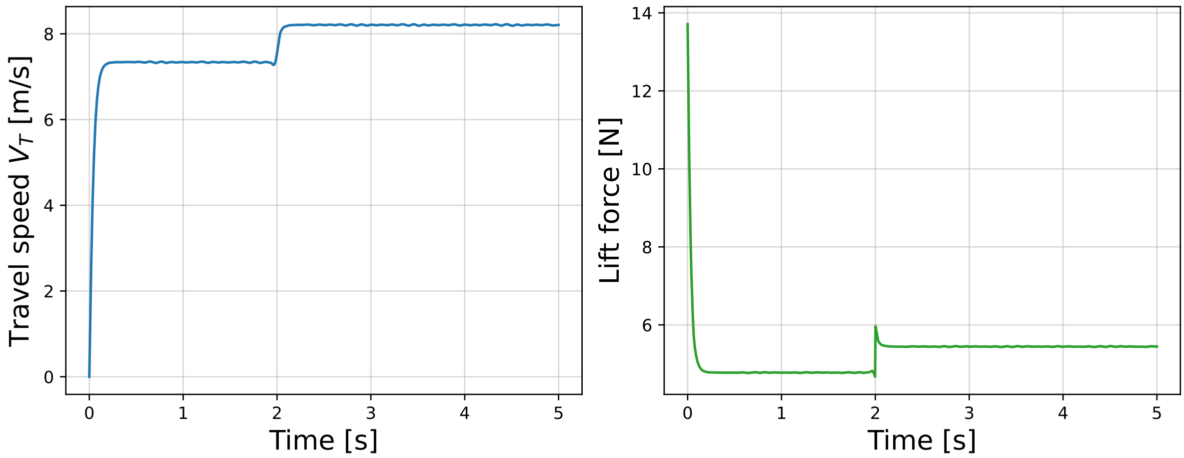

Figure 7.9: Evolution of the travel speed V_T and the total lift force for an acceleration occuring at t=2s.

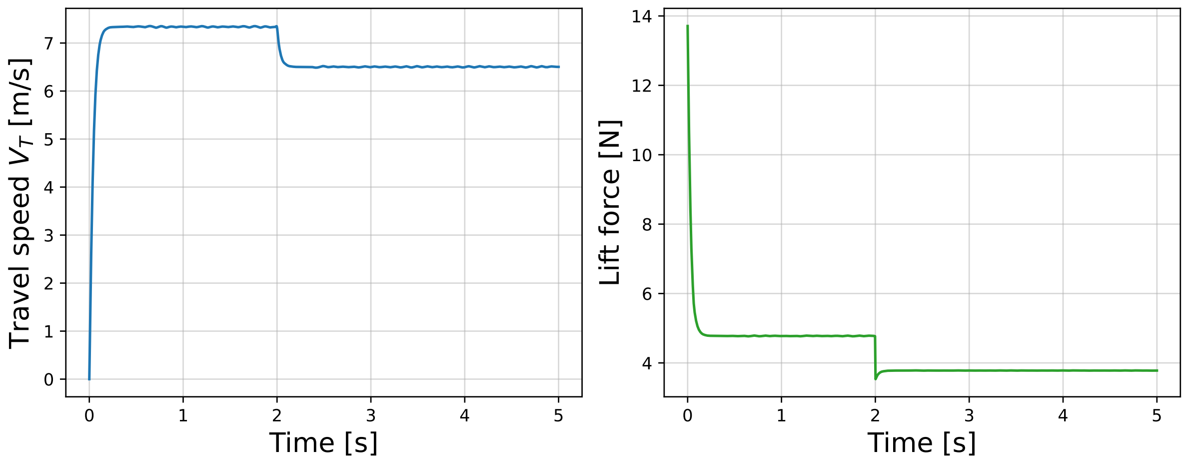

Figure 7.10: Evolution of the travel speed V_T and the total lift force for a deceleration occurring at t=2s.

7.3.2 Increasing Lift at Constant Speed

To keep a constant travelling speed V_T but increase lift, one can increase the rotational speed ω of the front wheel and decrease the one of the rear wheel - or inversely. The evolution of the speed and total lift force is depicted in Figure 7.12.

In this scenario, since we are still in the linear control zone of the thrust force, both increase and decrease cancel each other. The slip γ does not change, and the new resulting lift forces for each suspension can be found by vertically projecting the operating point in the slip-lift characteristic, such as shown in Figure 7.13. However, due to the asymmetry of the forces, although the total lift is increased, pitch takes place as illustrated in Figure 7.14.

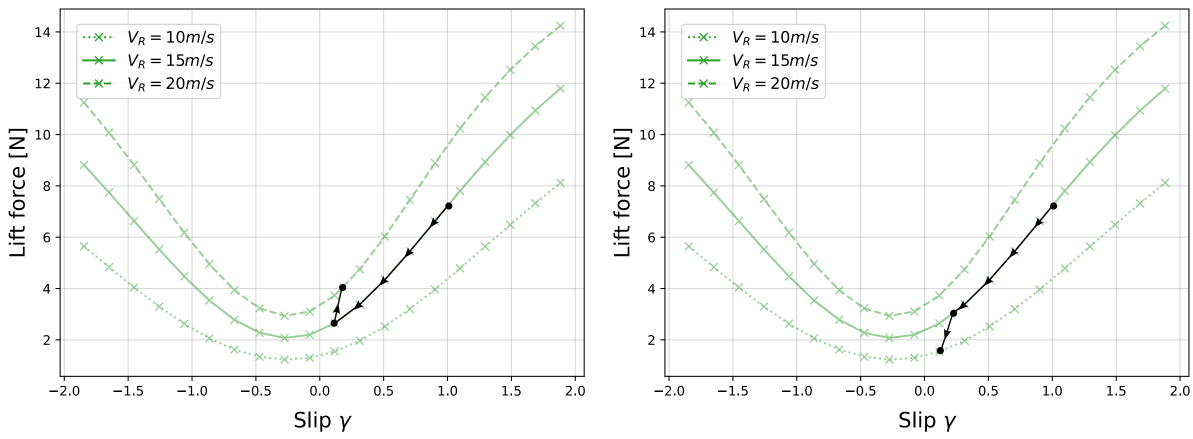

(a) (b)

Figure 7.11: Evolution of the lift forces along with the slip. (a) Acceleration of the pod. (b) Deceleration of the pod.

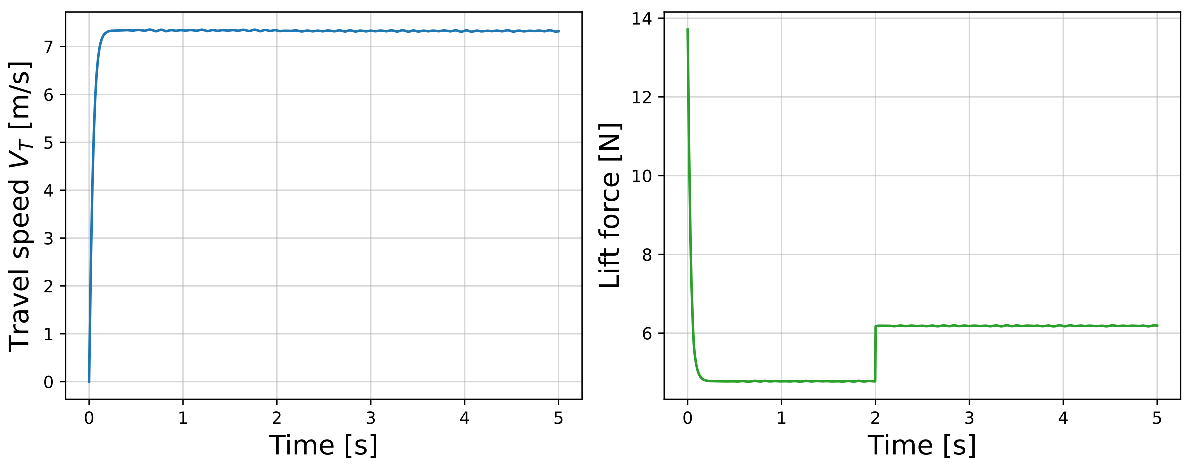

Figure 7.12: Evolution of the travel speed V_T and the total lift force for an increase of the rotational speed for the front wheel and a decrease for the rear wheel, occurring at t=2s. This results in increasing lift while keeping constant travelling speed.

7.4 Conclusions

The pod equipped with four HEDW has six DoFs. The first three are translational movements: the guidance, the lift and the propulsion. Along these axis, three rotational movements take place: the roll, the pitch and the yaw. Since the proposed vehicle is composed of only four wheels for six DoFs - and that each of them provide coupled guidance, lift and thrust - the vehicle is underactuated, leading to a complex control system.

The aim of this chapter was to provide a first insight of the dynamical behavior of such vehicle, in two distinct frames: the lateral frame taking into account two wheels in separated tracks, and the longitudinal frame analyzing two wheels within the same conductor.

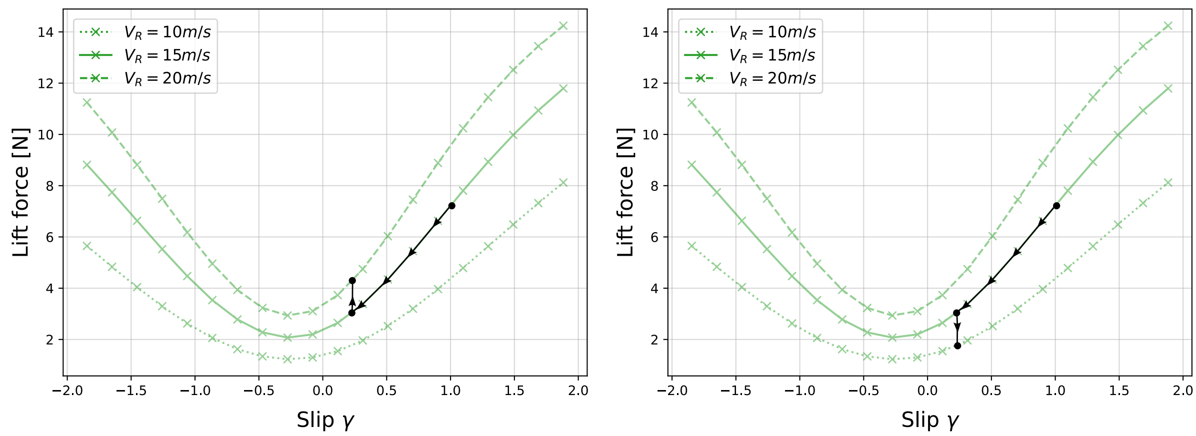

(a) (b)

Figure 7.13: Evolution of the lift forces along with the slip. (a) Front wheel (+ $\Delta\omega$) (b) Rear wheel (- $\Delta\omega$).

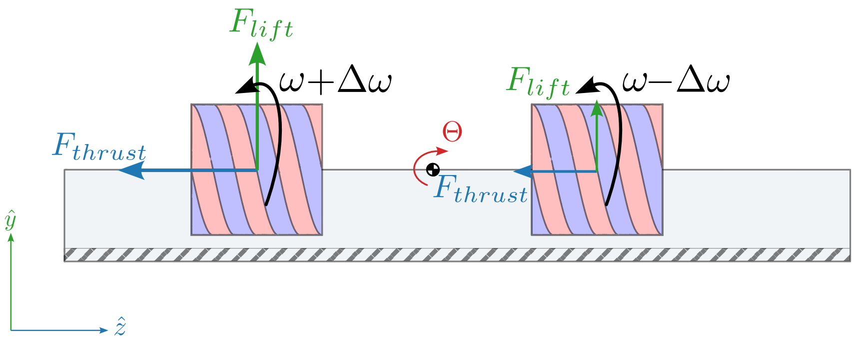

Figure 7.14: Distribution of the forces with an increase of the front wheel rotational speed, and a decrease of the rear one. The asymmetry in lift forces generates a pitch motion.

Unlike linear electrodynamic suspensions, the helical topology ensures stationary levitation thanks to rotation by external motors. Moreover, by increasing the rotational speed of the forward wheel while decreasing the speed of the rear one, the vehicle can achieve greater lift while keeping a constant travel speed. Nevertheless, if higher lift is achieved with acceleration, this force decreases when the vehicle brakes, compromising its stability.

To overcome problems of unstable guiding forces for 180° tracks, the conductor can be inclined from one section to another. Furthermore, the lateral analyses resulted in an undamped mass-spring system, leading the pod to oscillate when subject to a displacement in the vertical or lateral direction. To compensate for this, secondary damping systems should be considered.

The coupled generation of guidance, lift and thrust forces for each HEDW, and more specifically the imbalance of one of them when a perturbation or change in control occurs, is the source of the rotational pitch, yaw and roll.

8 | Discretized Helical Wheel

Contents

The ideal helix, forming a magnetic pole of the HEDW, is based on the extrusion of a section of circle along the helical path as defined by Equation 4.1. The resulting ideal wheel, represented in Figure 4.1, has been the case study so far - throughout the characterization and the first dynamical analyses.

In practice, such a continuous helical PM is almost impossible to manufacture - or would be laborious and cost greatly. This chapter therefore focuses on discretization techniques and the non-idealities that have to be taken into account when creating a HEDW based on conventional magnet shapes. To this purpose, two possibilities where envisaged : the azimuthal and axial discretizations, illustrated in Figure 8.1. First, the principles of both discretization techniques are explained.

Finally, the built prototype and its dedicated discretization are presented. This prototype will serve to validate the FEM models experimentally, for which the results will be presented in the next chapter. These algorithms are explained in details in Appendix E.

In this chapter, each magnet segment of given polarization is called an element. The dimensions of this so-called element are the variables of interest behind the developed discretization algorithms, where the goal is to minimize the deviation of the discretization with regard to the ideal helix.

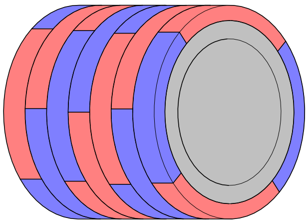

(a)

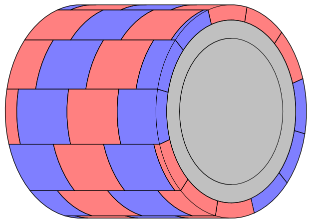

(b)

Figure 8.1: Discretization methods. (a) Azimuthal discretization. (b) Axial discretization.

8.1 Azimuthal Discretization

The azimuthal discretization is initially intended for ring PMs, although it could be suitable for tiled-shaped magnets also. These rings must already be magnetized with the desired number of pole pairs and magnetization direction. The inner and outer radius of the rings are constrained by the dimensions of the wheel. Such magnets are represented in Figure 8.2.

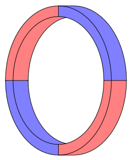

Figure 8.2: Azimuthal discretization : ring element.

In order to create the helical pattern, each ring must be turned by a constant angle $\Delta\theta$ with regard to the previous one. A representation of an azimuthal discretization pattern can be found in Figure 8.3, in the unwound 2D-plane of the wheel. In such a representation, the width of each element is defined as w in the axial z-direction , whereas the height is defined as h in the azimuthal θ-direction. Since the magnets are rings, cut rectangles at the top and bottom of a column represent parts of the same constitutive element in reality.

As for the definition of the suspension in chapter chapter 4, such a 2D plane is defined for a given radius R in the magnets' thickness span only, that is $R_{in} \leq R \leq R_{out}$. Therefore, since such rings are prismatic, the helical angle is fixed throughout the thickness of the wheel, as opposed to the ideal helix. For this reason, the helical angle must be chosen such as to respect the desired axial pole pitch τ_z.

The goal of the discretization is to minimize the error committed by each constitutive element. This error is computed as the area that do not contribute to the desired ideal helix. Naturally, the more total magnets we consider, the smaller each element and thus the lower the induced error will be.

In the case of the azimuthal discretization, the element height is fixed to the pole height - or azimuthal pole pitch τ_θ. Therefore, the free parameter regarding the dimensions of the

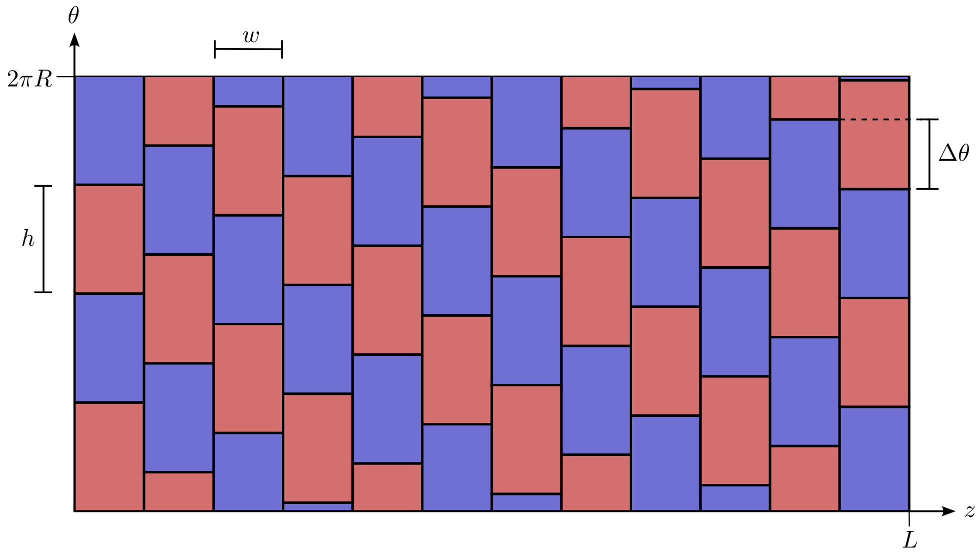

Figure 8.3: Azimuthal discretization : 2D-plane representation.

element for this type of discretization is the width w. This width is constrained given the maximum number of magnets we impose for the discretization.

8.2 Axial Discretization

The axial discretization scheme is very similar to the azimuthal one described above. In this case, the elements are shifted axially of a distance Δz between each row. The magnets used for this technique are tiled-shaped, as illustrated in Figure 8.4. Desired inner and outer radius of the wheel define both radius of curvature of the magnet. Due to the shape considered, magnets and elements are synonyms in this particular case.

Figure 8.4: Axial discretization : tile elements.

The unwound 2D-plane of the wheel is represented in Figure 8.5. As defined previously, w and h respectively denote the width and height of an element. In reality, h will therefore define the opening angle covered by the magnet.

In the case of the axial discretization, the element width is fixed to the axial pole pitch τ_z. Therefore, the free parameter regarding the dimensions of the element for this type of discretization is the height h. Similarly, the height is determined given the maximum number of magnets we consider for the discretization. One disadvantage of this technique is the need to cut the magnets at the edge of the wheels in order to achieve straight finishes.

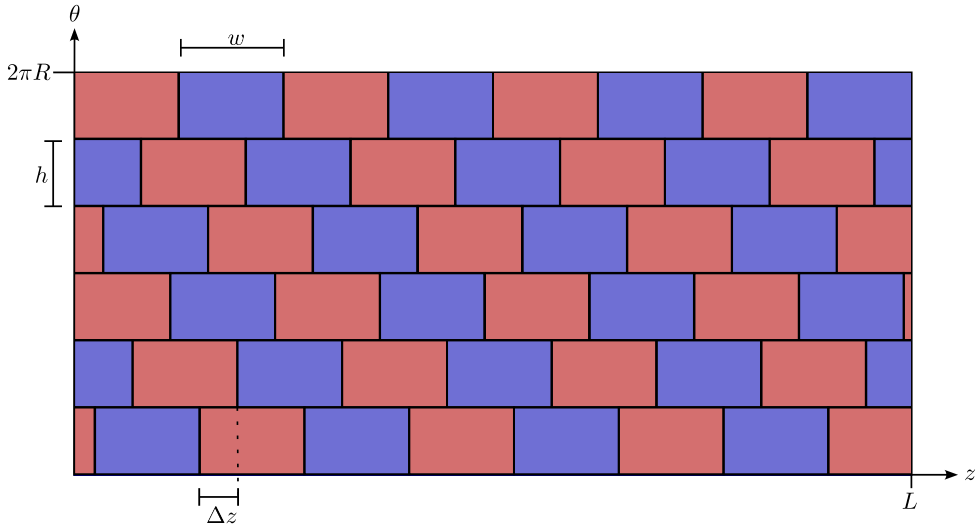

Figure 8.5: Axial discretization : 2D-plane representation.

8.3 Impact of Discretization

The impact of the discretization, either axial or azimuthal, over the ideal helix is represented in Figure 8.6, regarding the magnetic flux norm $|\mathbf{B}|$. Both discretization techniques result in a slightly less magnitude for the peaks of the magnetic field, upon adding some imperfections.

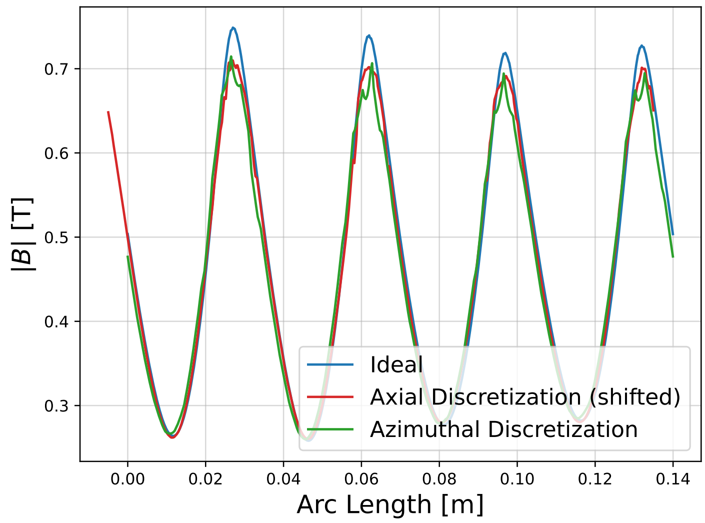

Figure 8.6: Impact of the different discretization (axial and azimuthal) on the magnetic flux norm in a circumferential path.

As both discretization algorithms result in the same error for a given set of primary parameters of the wheel, the variations in performance matter more than the shape of the source flux. The impact over the quantities of interest - the forces and drag torque generated - is summarized in Table 8.1.
Discretization, although necessary, reduces the expected performances. Both techniques

are close to each other, and if the azimuthal choice results in a higher guidance, the axial choice gives higher lift and thrust.

	Fx [N]	**Fy [N]**	**Fz [N]**	**Tdrag [Nm]**
Ideal	7.74	18.76	98.81	2.38
Axial Discretization	6.8	18.07	96.56	2.33
Azimuthal Discretization	7.23	17.36	94.58	2.19

Table 8.1: Impact of the different discretization (axial and azimuthal) on the generated forces and torque.

8.4 Prototype

This section focuses on the built prototype - its dimensions, discretization and assembly process.

Despite their existence on the market, ring magnets are rare and expensive. Attention has therefore been focused on an axial discretization scheme. Subsequently, due to the high cost of manufacturing custom magnets and, above all, delivery times, the ideal discretization was adapted to use prismatic magnets available from a supplier within a few days.

This idea followed the observation that the elements resulting from an axial discretization had a small opening angle and a large width - making it possible to approximate their circular section by a rectangle one instead, resulting in needle-like shaped magnets, as illustrated in Figure 8.7. To make it easier to fit the magnets, the ferromagnetic core of the wheel was built on a polygonal cross-sectional area.

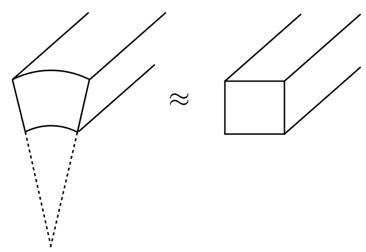

Figure 8.7: From tiled-shaped to prismatic magnets.

8.4.1 Polygonal Core

The polygonal cross-sectional area of the core, and more especially its number of sides, determines the number of rows in the equivalent unwound 2D-plane. In order not to constraint the height of an element, an algorithm determines the optimal radius of the circumscribed circle of the polygon to minimize the error caused by the discretization.

In the same way as increasing the total number of magnets reduces the induced error, increasing the number of sides of the polygon has the same effect. Therefore, this chosen number of sides is the driving parameter behind this adapted discretization.

The chosen magnets have dimensions 4x17x3mm. The resulting dimensions of the prototype can be found in Table 8.2, where the number of sides of the polygon has been fixed to 20. The wheel length has been chosen to be equal to three times the width of the prismatic magnets. This choice allows using both ends of cut magnets at each row extremity - and therefore reduces the number of magnet units used. A representation of the final polygonal core of the prototype is illustrated in Figure 8.8.

The axial discretization of the prototype is shown in Figure 8.9, whereas the discretization parameters are summarized in Table 8.3. The choice to constrain the number of sides of the polygonal core to 20 allows 5 magnets per magnetic pole along the circumference.

Parameter	**Value**
Inner Magnet Radius R_{in}	$13.5mm$
Outer Magnet Radius R_{out}	$16.5mm$
Wheel length L	$51mm$
Helical angle α	$49.4°$
Number of pole pairs p	2

Table 8.2: Dimensions of the prototype.

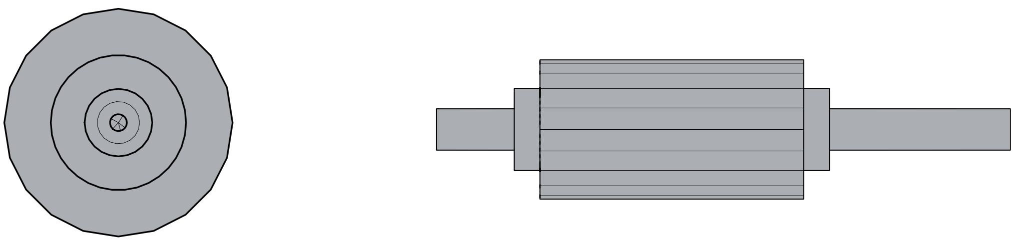

Figure 8.8: Prototype : final ferromagnetic polygonal core.

Parameter	**Value**
Element Width w	$17mm$
Element Height h	$4mm$
Number of sides of the polygon	20
Axial shift Δz	$3.4mm$

Table 8.3: Parameters of the axial discretization for the prototype.

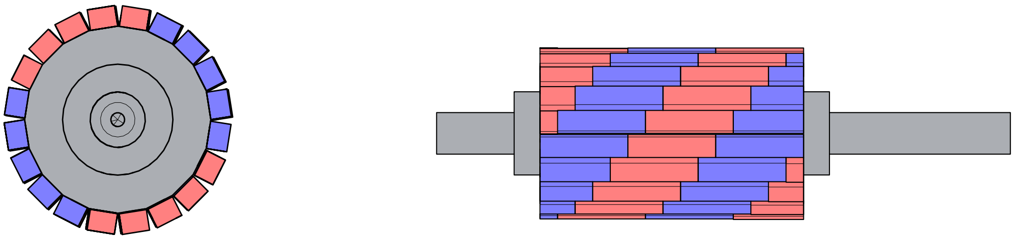

Figure 8.9: Final axial discretization of the prototype.

8.4.2 Assembly

This part aims at describing the process behind the assembly of the prototype.

Cutting Magnets

To obtain straight wheel edges, the magnets at both extremities need to be cut. This operation is carried out before the magnets are glued to the core, by electro discharge machining (EDM). To maintain the magnets in place during operation, a cutting tool must be designed, which is illustrated in Figure 8.10.

The tool is made of a ferromagnetic material, in order for the magnets to stick to the plate and facilitate the process. Each notch is offset from the cutting line regarding the discretization parameters considered. The wire of the EDM passes through the middle slot.

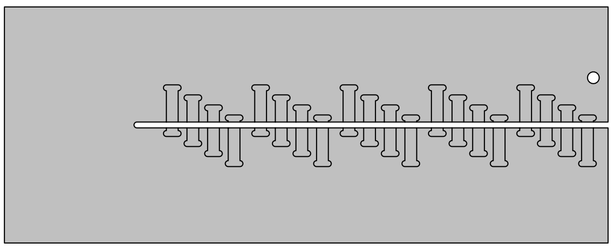

Figure 8.10: Plate maintaining the magnets for the EDM cutting.

Gluing Magnets

The helical arrangement of PMs elements is, by nature, unstable. Therefore, in order to facilitate the process of gluing the magnets to the core, guides were designed.

Assembly was proceeded in two steps. First, the magnets in alternating rows are glued to the core, thus leaving one free row in between them. The used 3D-printed guide, and the resulting wheel after this step, are illustrated in Figure 8.11. During this stage, the magnets line up naturally.

The guide for the second step was designed such as to encircle the magnets already glued, leaving the empty rows accessible. At this stage, the guide helps to push the magnets into each line, as they tend to turn and stick to the PMs in adjacent filled rows. The guide and final magnet arrangement is illustrated in Figure 8.12.

(a) (b)

Figure 8.11: First step of gluing magnets. (a) Guide. (b) Result.

(a) (b)

Figure 8.12: Second step of gluing magnets. (a) Guide. (b) Result.

Finally, to ensure mechanical integrity at high rotational speeds, the rotor was sleeved using Kevlar fiber.

8.4.3 Impact of Magnetization Direction

The ideal HEDW is radially magnetized. When performing discretization, either azimuthal or axial, the considered magnets are generally diametrally magnetized. This difference is depicted in Figure 8.13. For a diametral or parallel magnetization, the field is directed towards a fixed general direction (from one side to the other, passing through the diameter).

The used prismatic magnets for the prototype are magnetized with parallel field lines. Figure 8.14 shows the impact of the magnetization on the magnetic flux norm $|\mathbf{B}|$, along a circumferential path as illustrated in Figure 4.9. The polygonal-shaped discretization seems

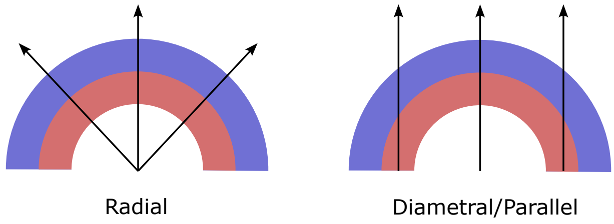

Figure 8.13: Magnetization directions.

to increase the magnitude of the peaks. The parallel instead of ideal radial magnetization deteriorates the smoothness of the field.

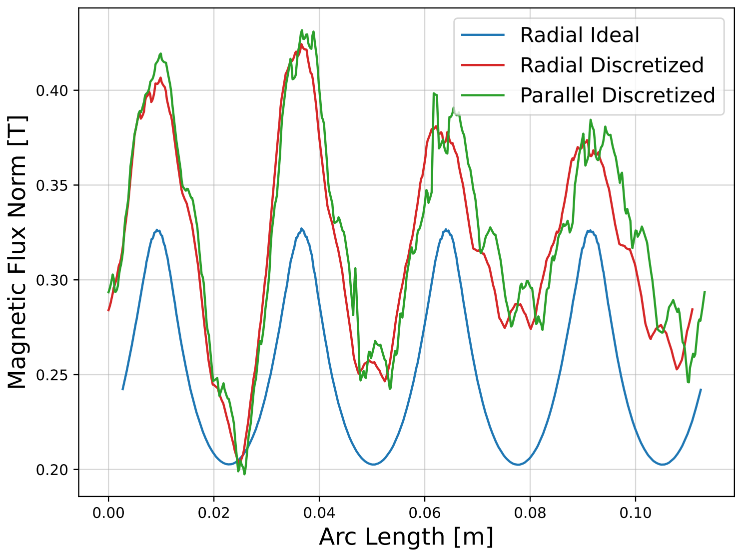

Figure 8.14: Comparison of different magnetization regarding the magnetic flux norm of the prototype.

Impact of the discretization and parallel magnetization on the forces generated are summarized in Table 8.3. A decrease around 25% can be noted for the discretization, whereas the magnetization (parallel instead of radial) appears to be less critical. This can be explained by the high magnet thickness ratio t_m of the considered magnets (≈ 0.82), where a shift from radial to parallel magnetization does not affect significantly the field distribution.

	Fx [N]	**Fy [N]**	**Fz [N]**	**Tdrag [Nm]**
Radial Ideal	13.36	21.9	47.6	0.61
Radial Discretized	9.7	16	34.6	0.45
Parallel Discretized	9.2	15.4	33.7	0.43

Table 8.4: Impact of the discretization and parallel magnetization on the forces generated for the considered prototype.

8.5 Conclusions

This chapter presented two possible choices for the discretization of the wheel : either azimuthal, by shifting ring magnets by an angle, or axial, by shifting tile-shaped magnets by a distance. This discretization is a mandatory step between the ideal HEDW and the real one, because of the manufacturing issues of magnet helices.

The objective of this discretization is to reduce the error committed, in the sense of minimizing the area of the magnets that do not contribute to the ideal helical pattern. Naturally, as more magnets are considered, the lower the total error will be. As both techniques rely on the same objective, the error will remain the same for all helical angles. The particular case of $\alpha = 45°$ results in elements of same dimensions for both discretizations.

The prototype was built following an axial scheme, with rectangular magnets glued upon a polygonal ferromagnetic core. In addition to the initial discretization error, the parallel magnetization and the geometry of the prototype result in an expected performance reduced by 25% compared with the ideal model. This will be further assessed in the next chapter, through an experimental validation of the developed 3D FEM models. The ideal discretization algorithms, based on tile-shaped magnets instead of rectangles, could have lead to better results regarding the prototype. The choice of adapting these ideal techniques was driven by the cost, availability and delivery times of suppliers - but allowed a deeper study of the impacts of the discretization with respect to the ideal HEDW.

9 | Experimental Validation

Contents

This chapter aims at validating the FEM models developed in chapter 5 and confirm the characterization of the suspension based on these latter, conducted in chapter 6. To achieve this, a test bench was designed in order to study the prototype described herein above.

First, this test bench and its limitations are presented. Finally, experimental results are compared to the models predictions. The characteristic evolution of the forces with the rotational speed ω is reproduced, as well as the characteristics relative to displacements δ_x, δ_y of the wheel in the guideway. Four tracks have been conceived, allowing to validate the impact of the opening angle β of the conductor as well.

9.1 Test Bench

The test bench is illustrated in Figure 9.1. A high-frequency motor spindle (1) is used to rotate the HEDW (2). Within this conception, no longitudinal travelling speed V_T is possible - therefore limiting the validation only to the impact of ω or relative displacements.

The track (3) is placed on a six-axis force-torque sensor (5) with the help of an interface plate (4). Therefore, all three forces and drag torque can be measured. The sensor itself is placed on a millimetric linear slide (7) through a second interfacing plate (6). The slide allows the displacement of the sensor and the track, whereas the spindle and the wheel remain fixed.

A frequency inverter allows the control of the rotational speed of the spindle. As the spindle is an asynchronous motor, it never reaches synchronous speed and some slip introduces a difference between the set frequency of the inverter and the true rotational

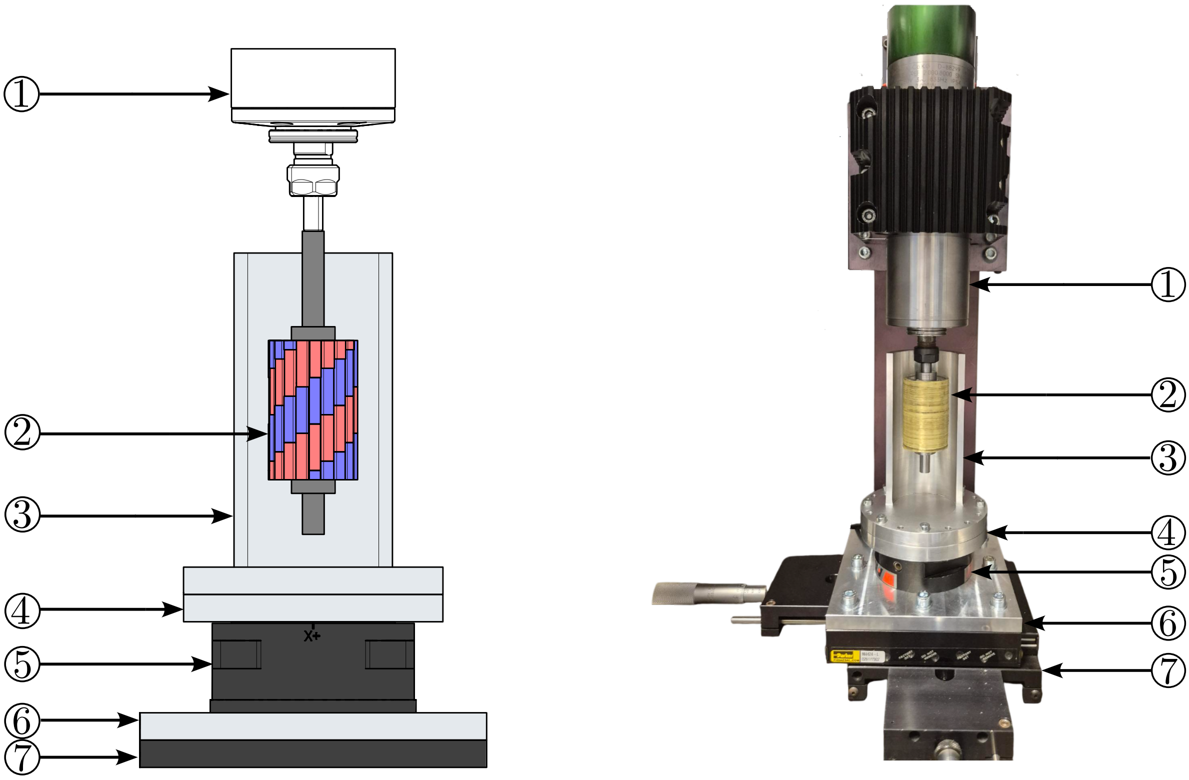

(a) (b)

Figure 9.1: Dedicated test bench. (1) Spindle. (2) HEDW. (3) Track. (4) Track-sensor interface. (5) Force-torque sensor. (6) Sensor-slide interface. (7) Millimetric linear slide.

speed. Measurements with a tachymeter allow to map the effective rotational speed with the control command.

The set of conceived tracks are represented in Figure 9.2. The first track is completely closed (360°) while the last has a 180° opening (half-track). The two intermediate guideways have spanning angles of 270° and 225° respectively, or in other words an opening β of 90° and 135°. Each track has a nominal air gap e of 8mm, and a thickness of 5mm.

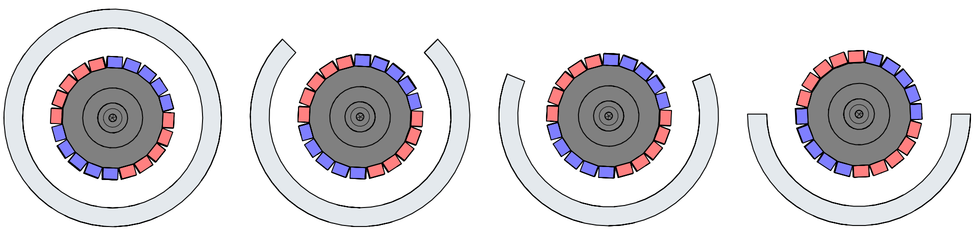

Figure 9.2: Top view of the set of tracks span angles : 360° (full), 270°, 225°, 180° (half).

9.2 End-Effects

Before continuing with the experimental characterization, the impact of end-effects was measured - to ensure conditions similar to the convergence analysis carried out in Appendix C. From the reference placement along the z-direction taken from the convergence analysis, the wheel was moved up and down by 5mm. Resulting measurements are summarized in Table 9.1.

	Fx [N]	**Fy [N]**	**Fz [N]**	**Tdrag [Nm]**
$\delta z = -5mm$	1.41482	1.2246	2.78898	0.03994
$\delta z = 0$	1.40262	1.26134	2.895792	0.04076
$\delta z = 5mm$	1.37823	1.20011	2.867309	0.04096

Table 9.1: Characterization of the end-effects for the experimental validation.

It is observed that the forces do not vary significantly. The difference is explained by instability of the measurement method (oscilloscope). With regard to the analysis made in Figure B.2, a slight offset of 5mm remains in the convergence zone of the Lorentz-based model.

9.3 Rotational Speed

Maintaining the suspension at a given position, we are able to reproduce Figure 6.12 by gradually increasing the rotational speed of the HEDW. Figure 9.3 shows the experimental results for a centered position in a full 360° track, compared with the Lorentz-based model valid in these conditions. Centered, no levitation and guidance forces occur, due to the symmetry in the induced currents.

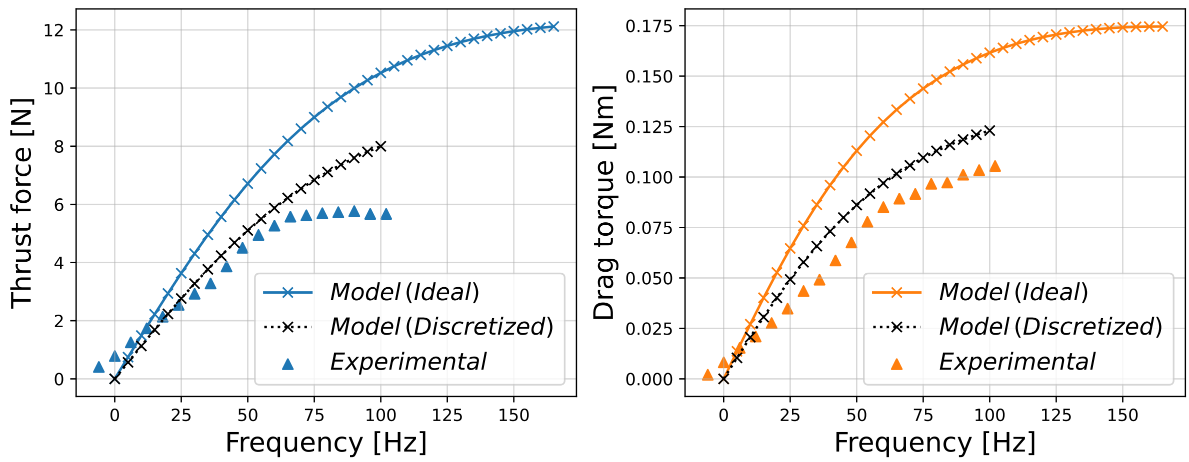

Figure 9.3: Experimental speed characteristic for a full (360°) track, compared with the Lorentz-based model.

The ideal model is the one described in chapter 5 (with the wheel embodied as a plain cylinder), whereas the discretized model uses the true prototype geometry and parallel magnetization as described in the previous chapter.

At low speeds, the experimental results follow the slope of the discretized model characteristic. Beyond 50Hz, the thrust force saturates. Although this behavior is typical of the propulsion force, the elbow arises earlier than expected. This phenomenon was observed for all tracks, and around the same frequency.

This phenomenon could be due to the increasing drag torque, that in turn could slightly increase the slip of the spindle - leading to a bigger difference between the control command and the actual rotational speed of the wheel. Moreover, the considered material in COMSOL Multiphysics® is pure aluminum, whereas the tracks were made of aluminum alloy, which has a lower electrical conductivity σ. This lower conductivity increases Joule heating locally, and consequently reduces the amount of forces generated. Nevertheless, these possible explanations were not confirmed to describe the force's behavior.

Results for the 180° track are illustrated in Figure 9.4. The experimental data are compared both to the Lorentz-based model and the rotating machinery model for a centered position of the wheel inside the conductor. The lift and thrust force results are closer to the rotating machinery model (RMM), although they still do not fit perfectly. The guidance force and drag torque results lie between both numerical characteristics. Similar to the behavior of the thrust force previously, the continuous growth of the guidance force beyond 50Hz could not be explained.

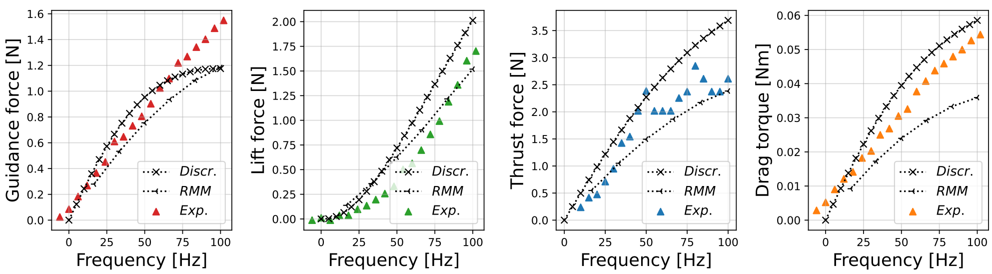

Figure 9.4: Experimental speed characteristic for a half (180°) track, compared with the Lorentz-based model and rotating machinery model.

9.4 Displacements

The forces-displacements characteristics were reproduced experimentally. By moving the track from the centered position thanks to the millimetric linear slide, a precise displacement either in the x or y-direction was achievable.

Experimental results for displacements in the y-direction with a half 180° track are shown in Figure 9.5. A negative displacement results in the wheel closer to the conductor, whereas a positive displacement means the wheel goes toward the opening and thus out of the track. As expected, for an open guideway, the forces tend to zero as the wheel goes out, whereas they grow exponentially when the air gap is reduced - matching the behavior established in subsection 6.3.3.

While the rotating machinery results match closely experimental ones, Figure 9.5 proves once again the increasing divergence of the Lorentz-based model with displacements, limiting its validity to centered positions and closed tracks only.

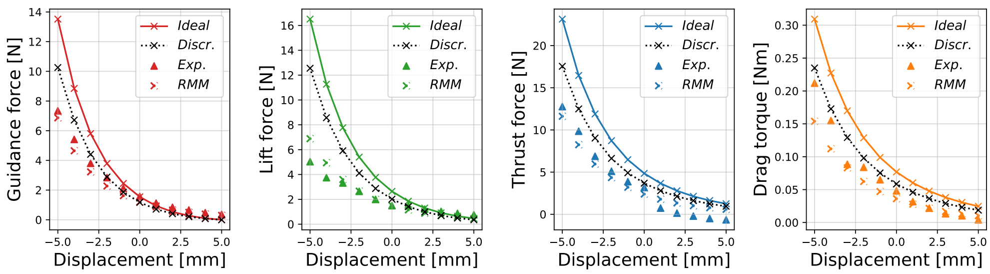

Figure 9.5: Experimental y-displacement characteristic for a half (180°) track, compared with the Lorentz-based model and rotating machinery model.

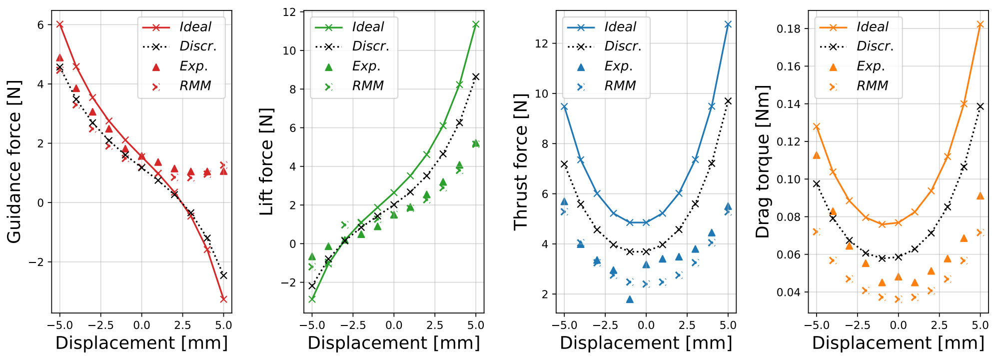

Figure 9.6: Experimental x-displacement characteristic for a half (180°) track, compared with the Lorentz-based model and rotating machinery model.

The results for displacements in the x-direction are shown in Figure 9.6. While the Lorentz-based model predicts a change of sign for the guidance force beyond a threshold displacement, this phenomenon never occurs with the experimental results and the rotating machinery model. Instead, the force remains uni-directional, meaning that no matter the direction of displacement the guidance force remains aligned with its initial direction, although reduced in magnitude. This confirms the instable lateral behavior of a single wheel within a half-track.
The rotating machinery results fit closely the experimental data.

9.5 Track Opening

With the four spanning angle described in Figure 9.2, the impact of the track opening angle β could be assessed experimentally. Both characteristics, related to the rotational speed ω and to δ_x or δ_y displacements, were reproduced.

The speed characteristic is depicted in Figure 9.7. Similar to the results obtained through the numerical characterization, no significant difference in magnitude can be noted for the guidance and lift forces. The thrust force and drag torque increase with the amount of conductive material (the more closed the guideway) as predicted.

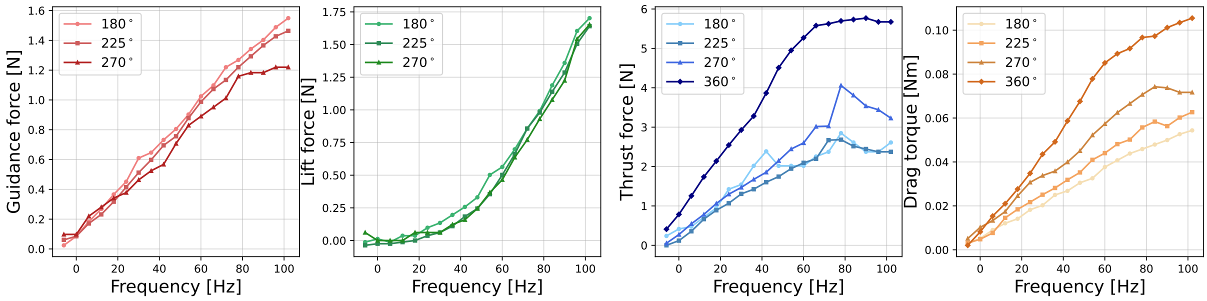

Figure 9.7: Experimental speed characteristic for the following track series : 180°, 225°, 270° and 360°

The comparisons between displacement characteristics, both in the x and y-directions, for different track openings are illustrated in Figure 9.8 and Figure 9.9. As the spanning angle of the conductor increases beyond 180°, the guidance force depicts a more stable behavior. Indeed, the characteristic changes sign, implying a positive stiffness no matter the direction of lateral displacement.
As predicted, the more open the guideway, the bigger the guidance and lift forces. This phenomenon is due to the cancelling effect that occurs between the upper and lower half-circle of the track when a spanning angle greater than 180° is considered.
The thrust force and drag torque increase with the amount of conductive material, similarly to the results obtained with the rotational speed characteristic.

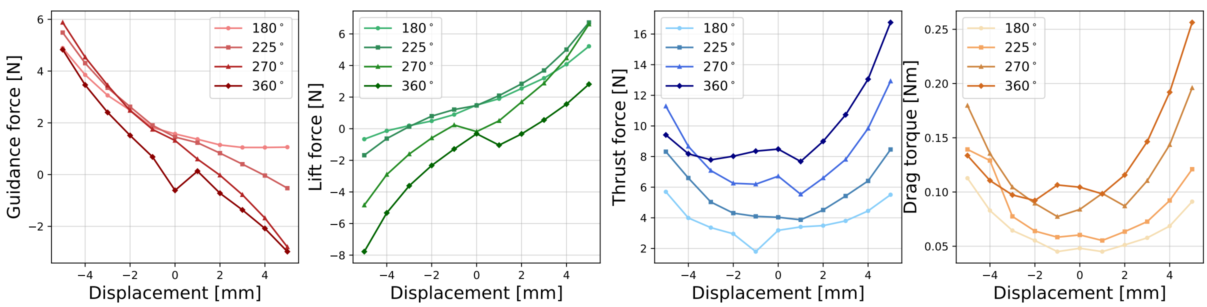

Figure 9.8: Experimental x-displacement characteristic for the following track series : 180°, 225°, 270° and 360°

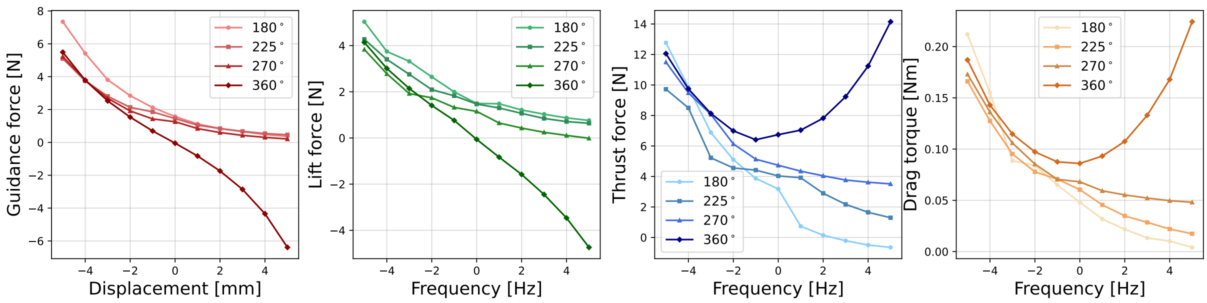

Figure 9.9: Experimental y-displacement characteristic for the following track series : 180°, 225°, 270° and 360°

9.6 Conclusions

This chapter presented the test bench that allowed to carry out an experimental validation of the FEM models and numerical characterization, developed respectively in chapter 5 and chapter 6. The convergence analysis carried out for the Lorentz-based model was confirmed by measuring the impact of end-effects.

Two characteristics were reproduced : the evolution of the forces with the rotational speed ω, and the evolution with displacements δ_x, δ_y inside the track. Furthermore, different track openings β allowed to perform an experimental characterization of the impact of this mechanical parameter.

Given the physical phenomena that were not taken into account in simulations, namely the exact electrical conductivity σ of the aluminum alloy of the tracks or the considerable heating that increases the resistivity of the material, the rotating machinery model still captures quite well the behavior of the proposed helical suspension. The increasing difference of the Lorentz-based model with displacements or track opening was further proven, although the advantage of this model rely on its ability to take into account a longitudinal travelling speed V_T.

The comparison of different track openings β highlighted the trade-off between volume of material considered and stability of the guidance force. Indeed, a spanning angle of the conductor greater than 180° depicts a positive stiffness for this force. This opening angle β is thus an alternative solution to improve stability of the vehicle, along the inclination of the track ϕ proposed in chapter 7.

All the experimental results can be found in Appendix F. The technical drawings related to the test bench and prototype can be found in Appendix G.

10 | Conclusion

Contents

The research behind this master's thesis aimed to design a helical electrodynamic suspension for MAGLEV vehicles, providing levitation, propulsion and guidance simultaneously.

First, it started with the state of the art regarding combined propulsion and levitation devices, as well as existing devices based on helical arrangement of PMs. The history of patents regarding helical wheels intended for MAGLEV transportation systems was traced. This led to the proposed topology studied in this work, as defined in chapter 4.

Beyond this design aspect, the development of 3D FEM models in chapter 5, using the software COMSOL Multiphysics®, has allowed a first numerical characterization of the suspension in chapter 6 - highlighting how the dimensional and mechanical parameters have an impact on the generated forces and performance criteria.

Two models, based on different strategies, were developed. The first, the Lorentz-based model, relies on steady-state simulations. The second, the rotating machinery model, relies on moving meshes and time-dependent simulations. Although the second model was proven to be more robust with respect to various displacements and track openings, it does not offer the possibility to take into account a travelling velocity. This key aspect motivates the use of the Lorentz-based model, valid for wheels centered within a completely closed conductor only.

Based on the results of both models, a first analysis of the dynamical behavior of a pod equipped with four HEDWs was conducted in chapter 7. This analysis highlighted the ability to achieve stationary levitation, as well as acceleration and deceleration. The undamped behavior of the suspension, when subject to lateral or vertical displacements within the track, leads to believe that a secondary system allowing damping should be considered. Moreover, the coupled generation of guidance, lift and thrust force with a single wheel, leads to coupled dynamics regarding the six DoFs of the vehicle. The inevitable unbalance of the forces generate rotational motions, such as pitch, roll or yaw along the principal directions of motion.

In chapter 8, the compulsory transformation from an ideal wheel to a discretized one for manufacturing purposes was investigated. Two different techniques were proposed: the first based on angular shifting of ring magnets, and the second based on axial shifting of tile-shaped magnets. In order to validate the developed models, a prototype was conceived. This latter used an axial discretization, formed with rectangular magnets upon a polygonal ferromagnetic core. The experimental results and characterization following this prototype was further presented in chapter 9.

All together, these different steps of the study successfully allowed a first insight into the feasibility and applications of HEDWs for MAGLEV ground transportation systems : by the design, the modelling and the experimental characterization.

10.1 Future Work

Due to the helical arrangement of PMs and the curved track topology considered, traditional analytical models are difficult to apply to this suspension. The developed models having proven their inability to span the complete dynamics, focus should be placed to the development of more robust ones. The idea under consideration is that of the PEEC (Partial Element Equivalent Circuit) model. The development of such model will enable the complete and coupled dynamics of the vehicle to be studied, along with the development of a control law for effective control of the speed, lift and guidance of the vehicle.

The initial characterization provided in this master's thesis paved the way for the optimization of the suspension regarding specific case studies. Although this characterization highlighted the main dimensional and mechanical parameters impacting the performances, it does not take into account the coupling that could occur between these parameters. Further characterization, both local and global, should be considered.

In conclusion, future work should focus on the development of more robust models and the extensive characterization of the HEDW, allowing for an accurate dynamical analysis of the proposed vehicle. These efforts would contribute to the development of more effective solutions - providing levitation, propulsion and guidance simultaneously - intended for MAGLEV systems.

Bibliography

[1] C. Lu, Z. Ren, and C. Ma, "Study on the technologies development trend of high speed emus," *High-speed Railway*, vol. 1, no. 1, pp. 1–5, 2023, ISSN: 2949-8678.

[2] W. D. H. do Amaral, G. V. L. Brandão, and J. A. B. Castañon, *Maglev Technology Review for Improving Urban Mobility*, F. Rebelo and M. M. Soares, Eds. Cham: Springer International Publishing, 2019, pp. 268–275, ISBN: 978-3-319-94706-8.

[3] T. Litman and D. Burwell, "Issues in sustainable transportation," *International Journal of Global Environmental Issues*, vol. 6, pp. 331–347, Feb. 2006.

[4] H.-W. Lee, K.-C. Kim, and J. Lee, "Review of maglev train technologies," *IEEE Transactions on Magnetics*, vol. 42, no. 7, pp. 1917–1925, 2006.

[5] J. Bird, "An investigation into the use of electrodynamic wheels for high-speed ground transportation," *University of Wisconsin-Madison*, 2007.

[6] Transrapid International, "High-tech for flying on the ground," Technical Brochure, 2003.

[7] L. SIU, "Innovative lightweight transit technologies for sustainable transportation," *Journal of Transportation Systems Engineering and Information Technology*, vol. 7, no. 2, pp. 63–70, 2007, ISSN: 1570-6672.

[8] R. Ahmed, Y. Jun, M. Azhar, and N. Junejo, "Comprehensive study and review on maglev train system," *Applied Mechanics and Materials*, vol. 615, pp. 347–351, Aug. 2014.

[9] L. Beauloye and B. Dehez, "Permanent magnet electrodynamic suspensions applied to maglev transportation systems: A review," *IEEE Transactions on Transportation Electrification*, vol. 9, no. 1, pp. 748–758, 2023.

[10] J. K. Nøland, "Prospects and challenges of the hyperloop transportation system: A systematic technology review," *IEEE Access*, vol. 9, pp. 28 439–28 458, 2021.

[11] R. H. Borcherts and L. C. Davis, "The superconducting paddlewheel as an integrated propulsion levitation machine for high speed ground transportation," *Electric Machines & Power Systems*, vol. 3, no. 3-4, pp. 341–355, 1979.

[12] L. C. Davis and R. H. Borcherts, "Superconducting paddle wheels, screws, and other propulsion units for high-speed ground transportation," *Journal of Applied Physics*, vol. 44, no. 7, pp. 3294–3299, Jul. 1973, ISSN: 0021-8979.

[13] J. Bird and T. Lipo, "An electrodynamic wheel: An integrated propulsion and levitation machine," vol. 3, 1410–1416 vol.3, 2003.

[14] J. Bird and T. Lipo, “A preliminary investigation of an electrodynamic wheel for simultaneously creating levitation and propulsion,” *18th International Conference on Magnetically Levitated Systems and Linear Drives*, 2004.

[15] C. Bruce et al., “An electrodynamic wheel maglev vehicle with a passive u-guideway,” pp. 1–6, 2022.

[16] Y. Yuan et al., “Working principle and primary electromagnetic characteristics of a permanent magnet electrodynamic wheel for maglev car application,” *IEEE Transactions on Applied Superconductivity*, vol. 31, no. 8, pp. 1–5, 2021.

[17] X. Sang et al., “Analysis and experiment on the levitation force and thrust force characteristics of a permanent magnet electrodynamic wheel for maglev car application,” *IEEE Transactions on Applied Superconductivity*, vol. 31, no. 8, pp. 1–4, 2021.

[18] J. Bird and T. Lipo, “A study of the effect of using electrodynamic wheels in series,” *8th International Symp. On Magnetic Suspension Technology*, 2005.

[19] A. Kushwaha, N. Endla, and B. G. Fernandes, “Motor integrated rotating permanent magnet based electrodynamic suspension device: Part i— concept and comparison,” *IEEE Transactions on Energy Conversion*, vol. 38, no. 3, pp. 1701–1714, 2023.

[20] Z. Zhang et al., “Design and operating mode study of a new concept maglev car employing permanent magnet electrodynamic suspension technology,” *Sustainability*, vol. 13, no. 11, 2021, ISSN: 2071-1050.

[21] H. Shi et al., “An effective optimization method and implementation of permanent magnet electrodynamic wheel for maglev car,” *IEEE Transactions on Vehicular Technology*, vol. 72, no. 7, pp. 8369–8381, 2023.

[22] P. Lin, Z. Deng, Z. Ke, W. Lei, X. Wang, and K. Ren, “Dynamic characteristics and working modes of permanent magnet electrodynamic suspension vehicle system based on six wheels of annular halbach structure,” *Technologies*, vol. 11, no. 1, 2023.

[23] N. Fujii, G. Hayashi, and Y. Sakamoto, “Characteristics of magnetic lift, propulsion and guidance by using magnet wheels with rotating permanent magnets,” vol. 1, 257–262 vol.1, 2000.

[24] K. Jung, “Parametric design of contact-free transportation system using the repulsive electrodynamic wheels,” *Journal of the Korea Academia-Industrial cooperation Society*, vol. 17, pp. 310–316, Mar. 2016.

[25] J. H. Park, J. H. Choi, D. H. Kim, and Y. S. Baek, “Parametric design of the levitation mechanism for maglev planar transportation vehicle,” *IEEE Transactions on Magnetics*, vol. 40, no. 4, pp. 3069–3071, 2004.

[26] J. Bird and T. Lipo, “An electrodynamic wheel with a split-guideway capable of simultaneously creating suspension, thrust and guidance forces,” *Research Report, Wisconsin Electric Machines and Power Electronics Consortium*, 2005.

[27] T. Sakamoto, A. Eastham, and G. Dawson, “Induced currents and forces for the split-guideway electrodynamic levitation system,” *IEEE Transactions on Magnetics*, vol. 27, no. 6, pp. 5004–5006, 1991.

[28] D. L. Atherton and A. R. Eastham, “Flat guidance schemes for magnetically levitated high-speed guided ground transport,” *Journal of Applied Physics*, vol. 45, no. 3, pp. 1398–1405, Mar. 1974, ISSN: 0021-8979.

[29] D. Mustafa and H. A. Hussain, “A review and comparative study on the design and analysis of magnetic lead screws,” *IEEE Transactions on Industry Applications*, vol. 59, no. 4, pp. 4108–4119, 2023.

[30] J. Wang, K. Atallah, and W. Wang, “Analysis of a magnetic screw for high force density linear electromagnetic actuators,” *IEEE Transactions on Magnetics*, vol. 47, no. 10, pp. 4477–4480, 2011.

[31] J. Ji, Z. Ling, J. Wang, W. Zhao, G. Liu, and T. Zeng, “Design and analysis of a halbach magnetized magnetic screw for artificial heart,” *IEEE Transactions on Magnetics*, vol. 51, no. 11, pp. 1–4, 2015.

[32] R. K. Holm, N. I. Berg, M. Walkusch, P. O. Rasmussen, and R. H. Hansen, “Design of a magnetic lead screw for wave energy conversion,” pp. 618–626, 2012.

[33] W. Li and K.-M. Lee, “Design and parametric analysis of a magnetic leadscrew with an embedded displacement sensor,” *IEEE/ASME Transactions on Mechatronics*, vol. 28, no. 4, pp. 1797–1806, 2023.

[34] Z. Ling, W. Zhao, J. Ji, and G. Liu, “Design of a new magnetic screw with discretized pms,” *IEEE Transactions on Applied Superconductivity*, vol. 26, no. 4, pp. 1–5, 2016.

[35] W. Herbert, *Production (generation) of travelling fields by means of rotating magnet arrangements*, DE. Patent 31 20328, 1982.

[36] P. Schuster, *Magnetic helix non-contacting linear drive*, U.S. Patent 5 079 458, 1992.

[37] I. Subotic, T. Arda, and J. W. Kolar, *Device for electromagnetic levitation and propulsion*, CH. Patent 714 405, 2022.

[38] COMSOL, *Acdc module user’s guide*, Version 6.3, Software Documentation, COMSOL AB, Sweden, 2023.

[39] J. Bird and T. A. Lipo, “A 3-d magnetic charge finite-element model of an electrodynamic wheel,” *IEEE Transactions on Magnetics*, vol. 44, no. 2, pp. 253–265, 2008.

[40] COMSOL. “Rotating machinery, 3d tutorial. ”[Online]. Available: `https://www.comsol.com/model/rotating-machinery-3d-tutorial-10437`.

[41] J. Bird and T. A. Lipo, “Calculating the forces created by an electrodynamic wheel using a 2-d steady-state finite-element method,” *IEEE Transactions on Magnetics*, vol. 44, no. 3, pp. 365–372, 2008.

[42] J. Bird and T. A. Lipo, “Modeling the 3-d rotational and translational motion of a halbach rotor above a split-sheet guideway,” *IEEE Transactions on Magnetics*, vol. 45, no. 9, pp. 3233–3242, 2009.

[43] N. Paudel, J. Bird, S. Paul, and D. Bobba, “A transient 2d model of an electrodynamic wheel moving above a conductive guideway,” in *2011 IEEE International Electric Machines and Drives Conference (IEMDC)*, 2011, pp. 545–550.

[44] G. Antonini, A. E. Ruehli, D. Romano, and F. Loreto, “The partial elements equivalent circuit method: The state of the art,” *IEEE Transactions on Electromagnetic Compatibility*, vol. 65, no. 6, pp. 1695–1714, 2023.

A | Topologies

As for the magnetic lead screws, several topologies of HEDW can be envisaged. The choice of material for the cylindrical core (ferromagnetic or not) will depend on the topology choice. Figure A.1 serves as color legend for the magnetization direction of the helices in the following presentation of the possible topologies, considering a cylindrical coordinate frame (r, θ, z).

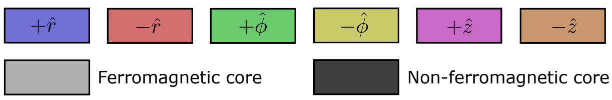

Figure A.1: Color legend for magnetization direction and core material.

Alternate Surface Mounted

The alternate topology, used as model in this work, requires a ferromagnetic core - also called back-iron, in order to guide the flux and reduce flux leakages. The high magnetic permeability of the material allows for a low-reluctance return path for the magnetic flux to travel through. Since flux leakages are greatly reduced, this increases the overall efficiency of the topology. The magnets are radially magnetized, and mounted on the surface of the cylindrical core with no gaps between the helices.

This topology is once again illustrated in Figure A.2.

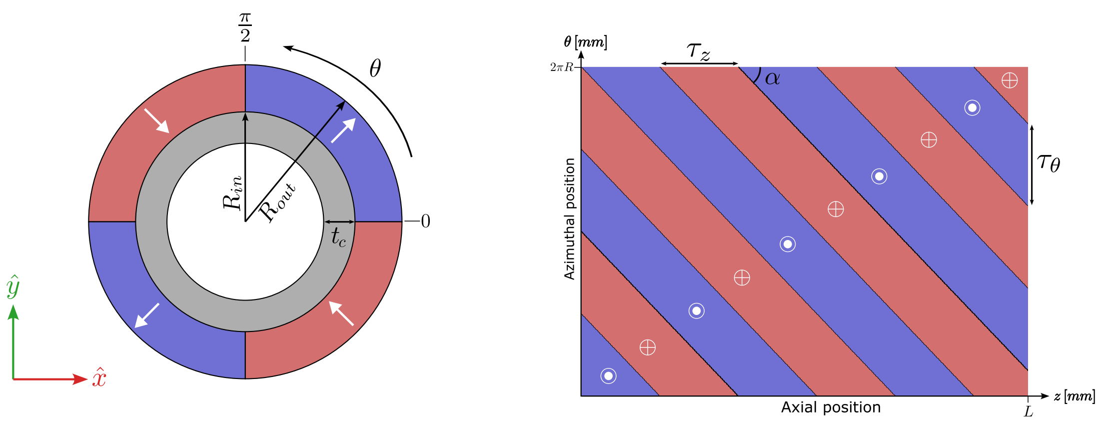

(a) (b)

Figure A.2: Ideal alternate HEDW. (a) Cross-sectional view in Cartesian coordinate frame. (b) Unwound 2D-plane in cylindrical coordinate frame.

Halbach Surface Mounted

The Halbach topology strengthen the external magnetic flux of the wheel through a particular arrangement of magnets, while almost cancelling it at the inside. Since the magnetic circuit is entitled to the magnet's arrangement, there is no particular need of a ferromagnetic core to reduce flux leakages or improve performances, and if not managed properly it could even cause short-circuiting of the field.

Depending on the pole pitch (τ_θ or τ_z) that we wish to strengthen, two Halbach configuration can be envisaged, as first proposed in [37].
The first configuration depicts radially and azimuthally polarised magnets, seen from a cross-section of the wheel. This strengthens the azimuthal pole pitch τ_θ, and is illustrated in Figure A.3.

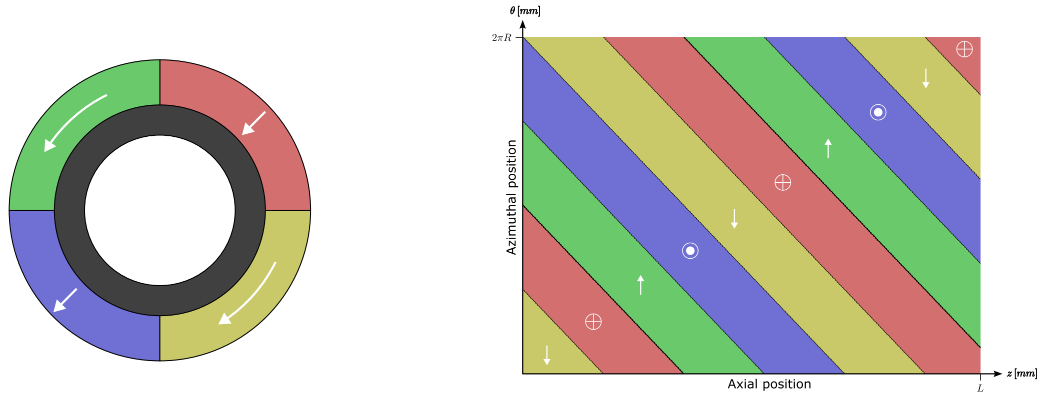

(a) (b)

Figure A.3: Halbach topology strenghtening the azimuthal pole pitch τ_θ. (a) Cross-sectional view. (b) Unwound 2D-place in cylindrical coordinate frame.

The second possible configuration uses radially and axially polarised magnets, thus strengthening the axial pole pitch τ_z. This topology is illustrated in Figure A.4. Comparison between these Halbach configurations and the alternate one is made in chapter Appendix C.

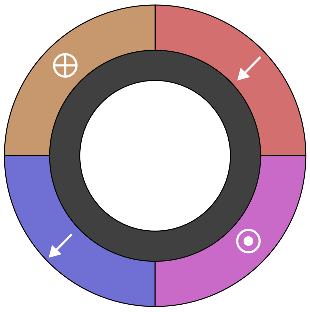

(a)

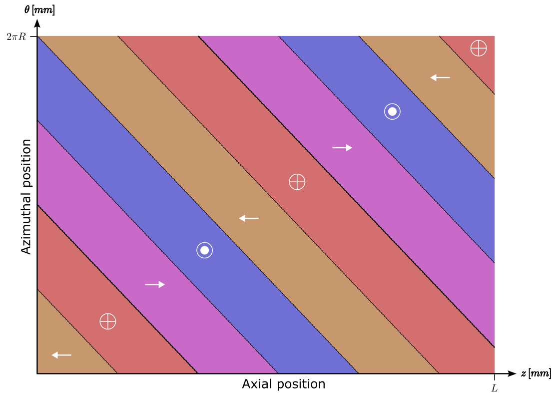

(b)

Figure A.4: Halbach topology strengthening the axial pole pitch τ_z. (a) Cross-sectional view. (b) Unwound 2D-place in cylindrical coordinate frame.

Spoke-type

The spoke-type or buried topology, opposed to surface mounted ones like alternate or Halbach, considers magnets trapped between ferromagnetic salliances. As for the Halbach topologies, depending on the pole pitch we wish to act on, we can consider two different types of spoke-type configuration. These are illustrated in Figure A.5 and Figure A.6.

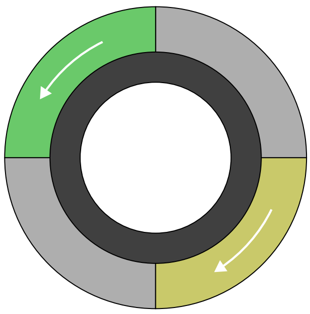

(a)

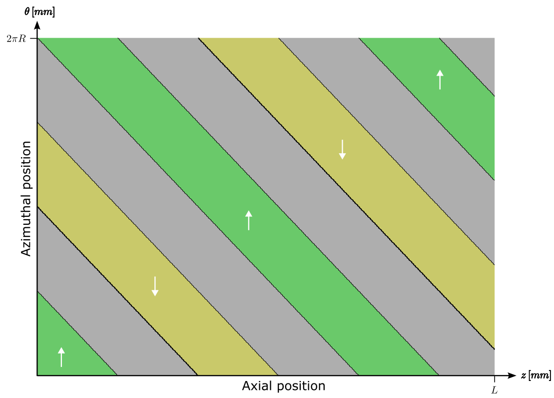

(b)

Figure A.5: Spoke-type topology enhancing the azimuthal pole pitch τ_θ. (a) Cross-sectional view. (b) Unwound 2D-place in cylindrical coordinate frame.

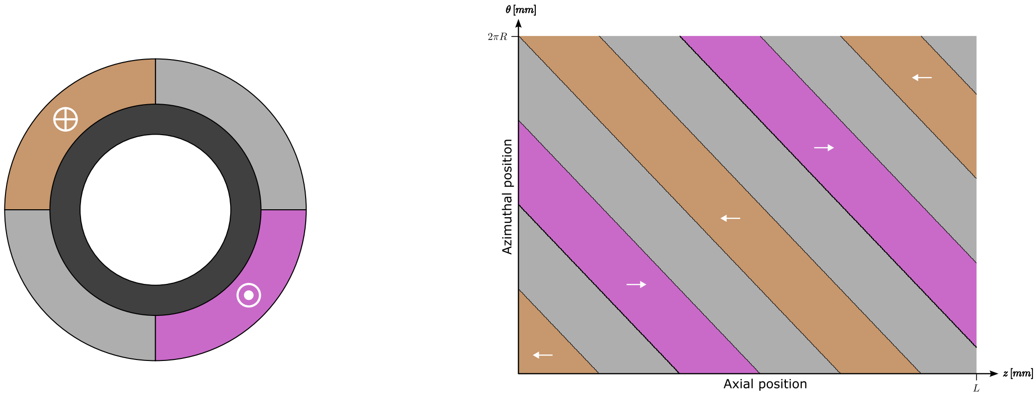

(a) (b)

Figure A.6: Halbach topology enhancing the axial pole pitch τ_z. (a) Cross-sectional view. (b) Unwound 2D-place in cylindrical coordinate frame.

Magnetization Rule for Mathematical Formulation

Table A.1 summarises the different magnetization rules for the possible topologies, regarding the mathematical formulation for the helical PMs pattern developed in subsection 5.1.1.

Alternate	
(k%2) = 0	$+\hat{r}$
(k%2) = 1	$-\hat{r}$

Halbach 1 Azimuthal	
(k%4) = 0	$+\hat{r}$
(k%4) = 1	$-\hat{\theta}$
(k%4) = 2	$-\hat{r}$
(k%4) = 3	$+\hat{\theta}$

Halbach 2 Axial	
(k%4) = 0	$+\hat{r}$
(k%4) = 1	$-\hat{z}$
(k%4) = 2	$-\hat{r}$
(k%4) = 3	$+\hat{z}$

Burried 1 Azimuthal	
(k%4) = 0	$+\hat{\theta}$
(k%4) = 1	0
(k%4) = 2	$-\hat{\theta}$
(k%4) = 3	0

Burried 2 Axial	
(k%4) = 0	$+\hat{z}$
(k%4) = 1	0
(k%4) = 2	$-\hat{z}$
(k%4) = 3	0

Table A.1: Magnetization rule for the mathematical function of the helical pattern.

B | Convergence Criteria for the FEM Models

Meshing and Convergence

The meshes of the various domains, and especially their size, has a significant impact on the numerical results of the models. Similarly, the limits of the air cylinder surrounding the suspension and the guideway play a crucial role in the behavior of the magnetic field lines and therefore greatly influence the results. These two aspects are investigated in this section, in order to guarantee model convergence while minimizing computational costs.

The convergence analysis was performed on the Lorentz-based model - because of the long simulation time which makes it difficult to analyze the rotating machinery magnetic model.

Geometrical Convergence Criteria

Size of the Air Cylinder

Two parameters define the aspect ratio of the air cylinder surrounding the geometry with regard to the considered wheel dimensions : the radius R_{air} and the longitudinal cleared space L_{air} at both ends, illustrated in Figure 5.2. The aim is to capture end-effects and truncate the length of the track to the section contributing to the generation of forces only, as an excessively large geometry implies more simulation efforts.

Figure B.1 represents the three force components F_x, F_y, F_z when increasing the radius of the air capsule. The aim is to find the value of a parameter α in a proportional relationship such as $R_{air} = \alpha R_{out}$ that guarantees convergence of the forces no matter the radius of the wheel considered. Beyond $\alpha = 2$, convergence is reached for the three components of forces.

Similarly, Figure B.2 illustrates the forces when increasing the lateral clearance at both ends of the wheel, following the relationship $L_{air} = \beta L$, for various wheel lengths. For both figures, the forces have been normalized with regard to the parameter of interest (radius

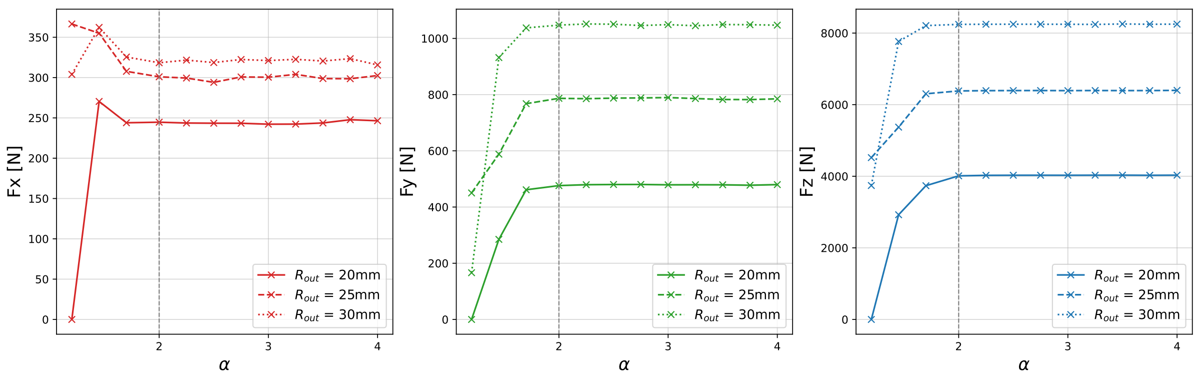

Figure B.1: Convergence of the forces with regard to the air radius R_{air}.

or length). Beyond $\beta = 0.4$, convergence is reached for the thrust and lift force. However, assuring perfect convergence for the guidance force for longer wheels seems compromised.

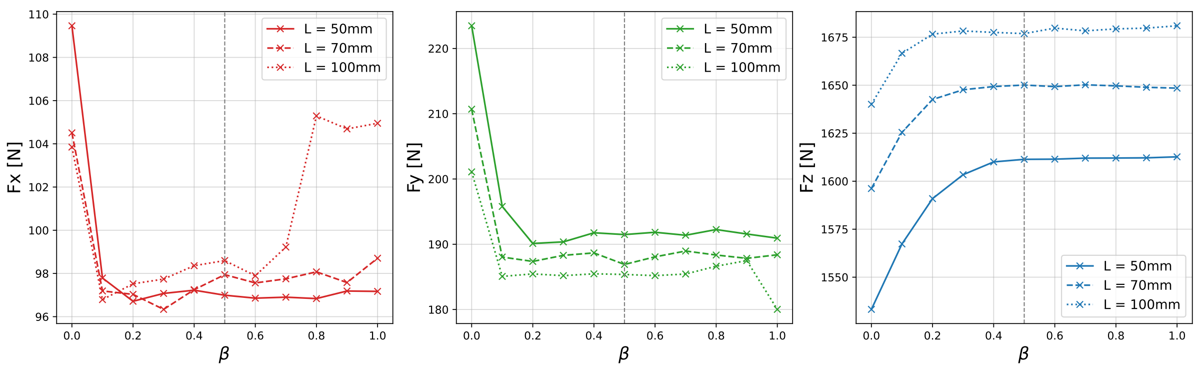

Figure B.2: Convergence of the forces with regard to the lateral air L_{air}.

Meshing Convergence Criteria

Track Mesh

Naturally, the domains of interest - such as the track, should be meshed more finely with regard to the surrounding air. A penalizing condition for the numerical convergence of the model is to have an element size smaller than the skin depth of the induced currents. Therefore, the conducting domain should be meshed such as to ensure the respect of this condition.

PMs Mesh

The impact of PMs mesh refinement on the three force components is shown in Figure B.3. Zero denotes an extra coarse mesh size, whereas 8 represents an extremely fine meshing.

The values are slightly oscillating around a mean convergence value, illustrating numerical artifacts. Therefore, this implies that the wheel mesh size is less critical than the mesh size of the track.

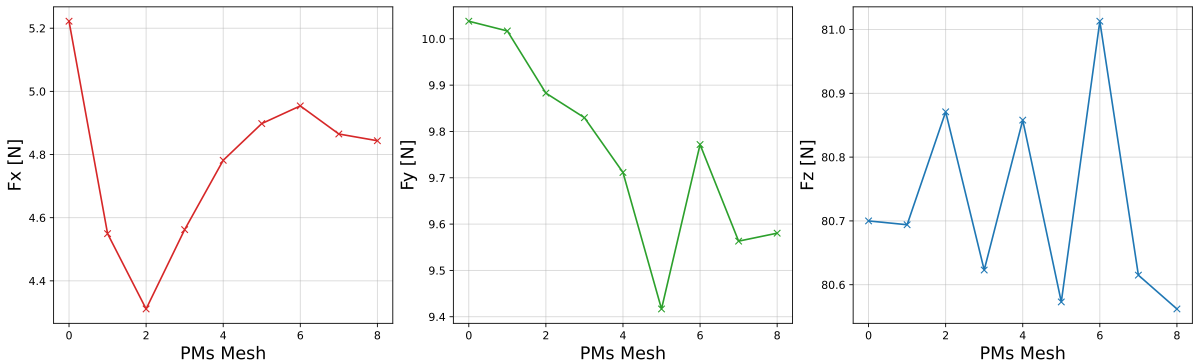

Figure B.3: Impact of PMs mesh size on the forces convergence.

Figure B.4 depicts the impact of this meshing on the magnetic field in the air gap, probed at the circumference of the wheel as presented in section 4.3. Therefore, an extremely fine mesh is chosen as safety measure. It must be noted that, for dimensional parameters leading to very fine helices, this parameter could become more significant since a coarser mesh could not match the pattern accordingly.

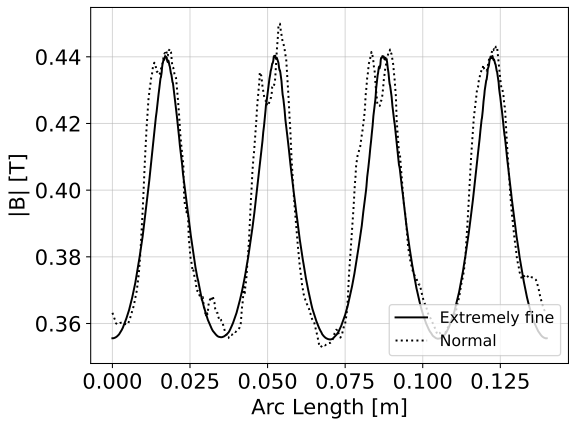

Figure B.4: Impact of the PMs mesh size on the smoothness of the static magnetic field.

General Mesh

Finally, Figure B.5 illustrates the impact of the global mesh size in the air domains. Since the observed variations are very small (on the order of 0.001 N), a default mesh size setting (4, normal) has been kept throughout all future simulations.

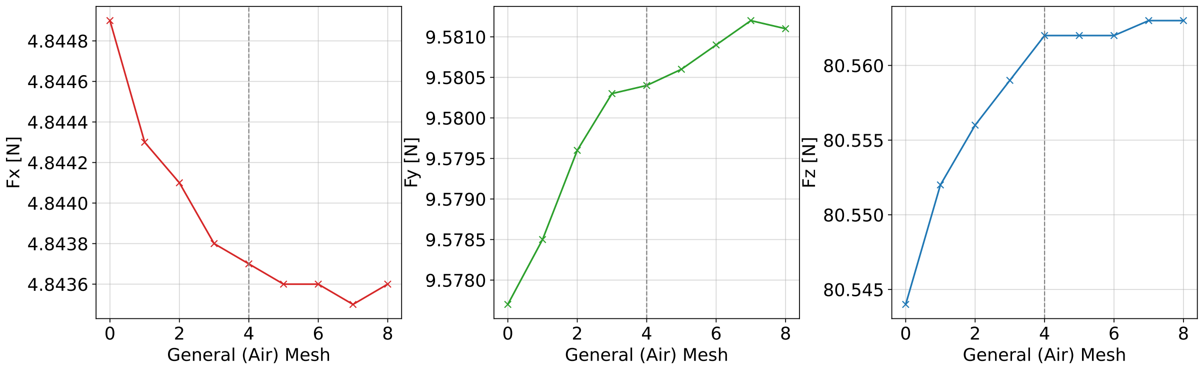

Figure B.5: Impact of the general (air) mesh size on the convergence of forces.

C | Characterization (Suite)

This appendix provides some additional characterization analyses to chapter 6.

Helical angle

Lift-to-Weight (LWR) for Helical Angle

Figure C.1 illustrates the impact of the helical angle α and the axial pole pitch τ_z on the lift-to-weight ratio (LWR). The higher the helical angle, resulting in a tightly wound helix, the worst the LWR. This confirms the inefficiency of such wheels.

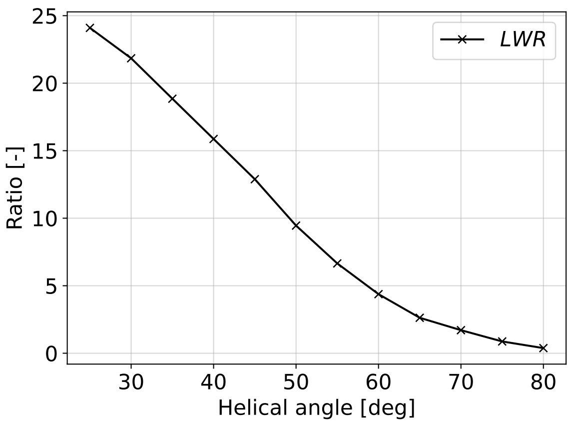

(a)

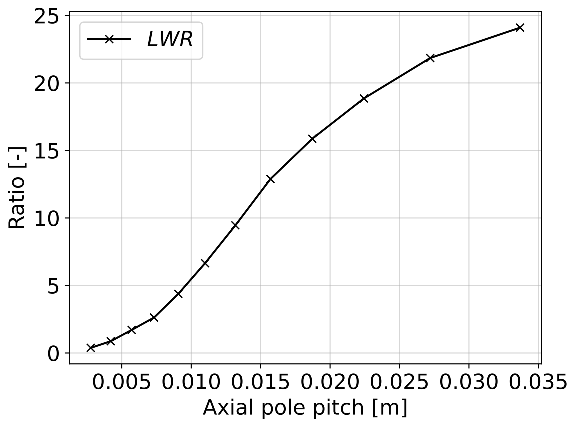

(b)

Figure C.1: Evolution of the lift-to-weight ratio (LWR). (a) With respect to the helical angle α. (b) With respect to the axial pole pitch τ_z.

Optimal Angle for Thrust

Table C.1 summarizes how the optimal helical angle α for the maximum thrust force evolves with the magnet thickness ratio t_m and the number of pole pairs p. This optimal angle does not always exist - when the magnets are thick, the characteristic only decreases with α.

This optimal angle increases with the magnet thickness ratio, and decreases with the number of pole pairs. This is further illustrated in Figure C.2.

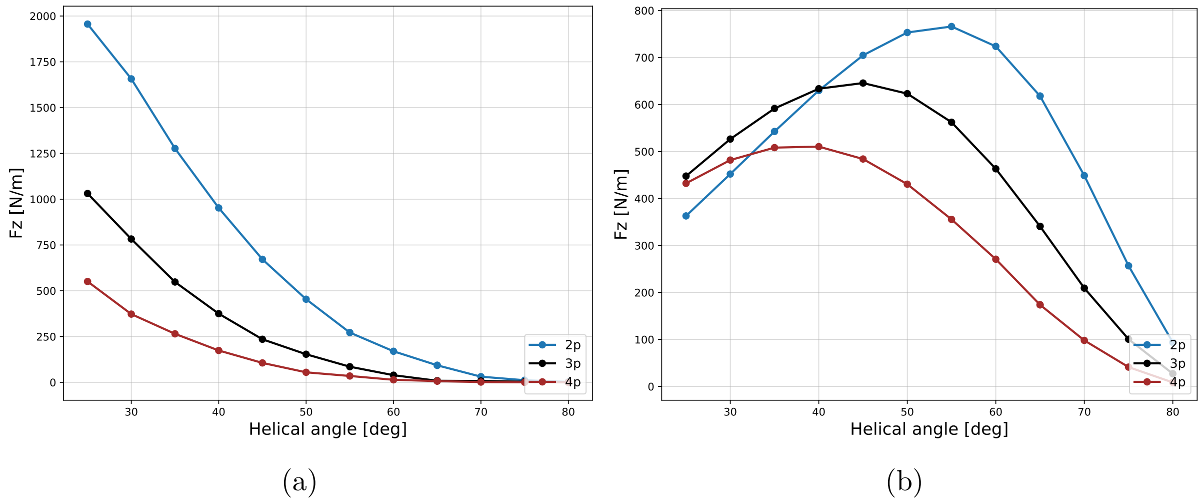

Figure C.2: Evolution of the helical angle α leading to the maximum thrust force with respect to the number of poles pairs p. (a) $t_m = 0.3$. (b) $t_m = 0.9$.

p / tm	**0.1**	**0.2**	**0.3**	**0.4**	**0.5**	**0.6**	**0.7**	**0.8**	**0.9**
2p	-	-	-	-	30°	35°	40°	45°	55°
3p	-	-	-	-	-	30°	30°	35°	45°
4p	-	-	-	-	-	-	-	30°	40°

Table C.1: Evolution of the helical angle α leading to the maximum thrust force with respect to the number of poles pairs p and the magnet thickness ratio t_m.

Angle for Maximum TDR

Table C.2 summarizes how the optimal helical angle α leading to the maximum thrust-to-drag ratio (TDR) evolves with the magnet thickness ratio t_m and the number of pole pairs p. As for the previous analysis, this optimal angle does not always exist.

This angle increases with the magnet thickness ratio, and decreases with the number of pole pairs. This characteristic is further illustrated in Figure C.3.

p / tm	**0.1**	**0.2**	**0.3**	**0.4**	**0.5**	**0.6**	**0.7**	**0.8**	**0.9**
2p	-	35°	45°	55°	60°	65°	65°	70°	70°
3p	-	-	40°	45°	50°	55°	60°	65°	65°
4p	-	-	35°	40°	45°	50°	55°	60°	65°

Table C.2: Evolution of the helical angle α leading to the maximum TDR with respect to the number of poles pairs p and the magnet thickness ratio t_m.

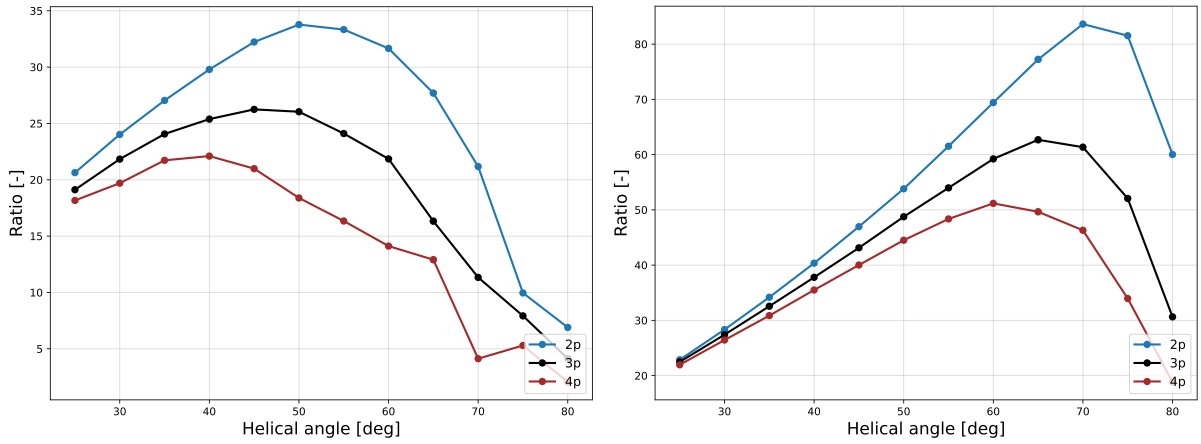

(a) (b)

Figure C.3: Evolution of the helical angle α leading to the maximum TDR with respect to the number of poles pairs p. (a) $t_m = 0.4$. (b) $t_m = 0.9$.

Topologies

The main question to be raised is how to define an equivalent Halbach topology. By definition, a Halbach arrangement needs four individual magnetic poles to form a pair. Therefore, at constant radius, the effective pole pitch (both azimuthal and axial) decreases. Inversely, keeping pole pitches constant but changing the number of pole pairs has an impact on the electrical frequency of the field, and thus the skin depth given Equation 6.8.

As a reminder, two possible Halbach arrangements can be defined, regarding the desired pole pitch to be enhanced.

Table C.3 summarizes the performances for the three considered topologies when all the parameters except the number of pole pairs is kept constant. All are formed with four helices, meaning two pole pairs for the alternate topology but one pole pair for the Halbach ones. Subsequently, this also means that both pole pitches are reduced by half for the Halbach arrangements. Halbach configurations generate more absolute forces - but also more drag torque. The Halbach enhancing the axial pole pitch τ_z seems to deliver better performances.

	Fx [N]	**Fy [N]**	**Fz [N]**	**Tdrag [Nm]**
Alternate	4.84	9.58	80.56	1.05
Halbach τ_θ	5.33	11.17	142.8	1.95
Halbach τ_z	7.73	15.4	208.54	2.27

Table C.3: Comparison of Halbach equivalent topologies. All configurations are based on the same constitutive helices. Number of pole pairs and pole pitches are consequently reduced by half for Halbach arrangements.

Table C.4 summarizes the performances when all topologies share the same number of pole pairs as well as pole pitches. To achieve this, the outer magnet radius R_{out} of the alternate topology was divided by half. A meaningful comparison will thus require a scaling of the generated forces for the reference configuration. Still, both Halbach equivalents seem to deliver more forces - where enhancing the axial pole pitch over the azimuthal one stay favorable.

	Fx [N]	Fy [N]	Fz [N]	Tdrag [Nm]
Alternate	2.88	1.81	19.511	0.13
Halbach τ_θ	4.825	10.14	85.56	1.15
Halbach τ_z	6.49	13.19	121.55	1.38

Table C.4: Comparison of Halbach equivalent topologies. All configurations share the same number of pole pairs and pole pitches, where to achieve this the alternate topology has an outer radius reduced by half.

Air gap

Figure C.4 illustrates the impact of the track inner radius R_t, and thus the nominal air gap e, on the generated forces. Naturally, the greater the air gap (with a greater inner track radius), the lower the forces. In response to this, the lift-to-weight ratio (LWR) also decreases with this dimensional parameter, as depicted in Figure C.5.

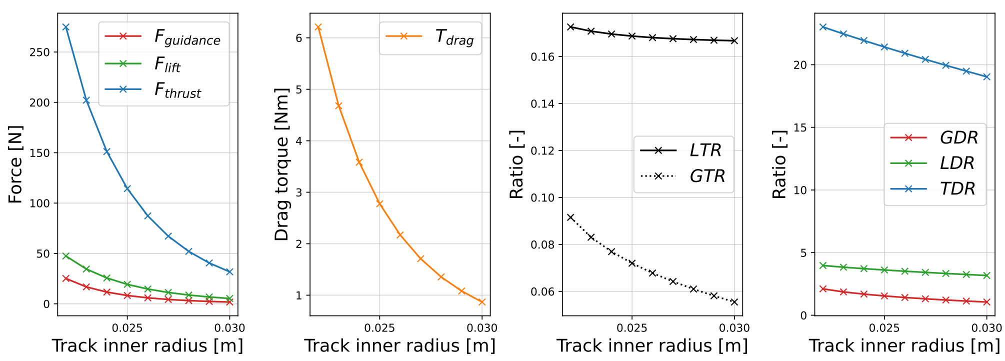

Figure C.4: Evolution of the forces and drag torque with the track inner radius R_t.

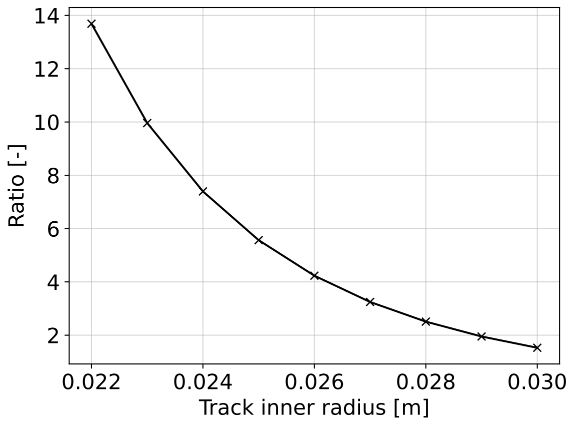

Figure C.5: Evolution of the lift-to-weight ratio (LWR) with the track inner radius R_t.

Longitudinal Speed

Figure C.6 depicts the evolution of the guidance, lift and thrust force with different rotational speeds ω (and consequently different circumferential speeds V_R). These are particularly useful to study the dynamical behavior of the proposed pod.

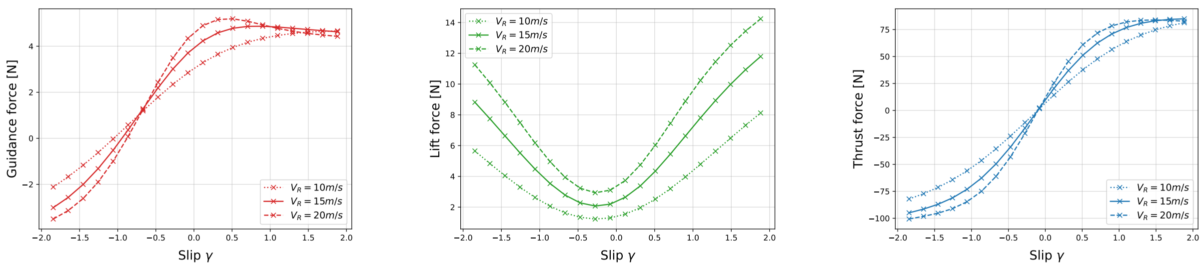

(a) (b) (c)

Figure C.6: Evolution of the forces with different rotational speeds ω (or V_R) with a longitudinal travelling speed V_T. (a) Guidance force. (b) Lift force. (c) Thrust force.

Displacements

Figure C.7 illustrates the evolution of the forces and drag torque with displacements in a 360° track. With this spanning angle of conductor, all forces have positive stiffness : a displacement in a given direction results in a repulsive force that brings back the wheel to its center. Therefore, additionally to tilting the track of an angle ϕ, a conductor with a smaller opening β than 180° could positively contribute to the stability of the guidance force - although reducing its magnitude.

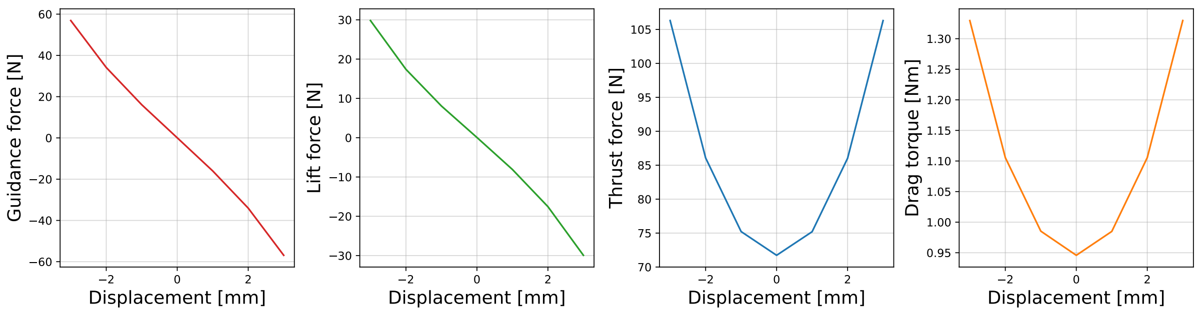

Figure C.7: Evolution of the forces and drag torque with displacements, for a 360° track.

D | Sensitivity Analysis

This appendix provides some additional characterisation analyses, with a particular focus on the global characterisation of a large dataset.

By means of a sensitivity analysis carried out with Optimeed, a tool for data generation, 11 300 different wheels have been evaluated. Table D.1 summarises the range of primary parameters considered for the evaluated HEDWs. Using Sobol sequences, the algorithm aims at filling the design space uniformly with quasi-random points.

Parameter	**Min. Value**	**Max. Value**
Number of pole pairs p	1	6
Helical angle α	10°	80°
Inner magnet radius R_{in}	1mm	29mm
Outer magnet radius R_{out}	10mm	30mm
Wheel length L	30mm	70mm

Table D.1: Ranges of values considered for the dataset.

Histograms of Performance Criteria

Among this large dataset, histograms are a way to visualise the distribution of the performance criteria defined previously, such as ratios defined with regards to the drag (guidance-to-drag GDR, lift-to-drag LDR, thrust-to-drag TDR ratios) or to the weight (lift-to-weight ratio LWR).

For each histogram, the mean and the associated normal distribution is shown - although for most of them, this normal distribution is far from being the best fitted one. The lift-to-weight ratio LWR depicts a flat histogram without real peak tendency, meaning that the values are more or less evenly distributed (uniform distribution).

Table D.2 summarises the mean values for each performance criteria.

	GDR	**LDR**	**TDR**	**LWR**
Mean	4.07	15.91	34.37	10.6

Table D.2: Mean values for the GDR, LDR, TDR and LWR.

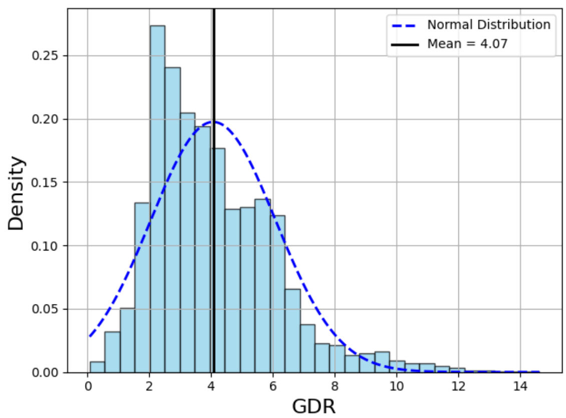

Figure D.1: Histogram for the guidance-to-drag ratio (GDR).

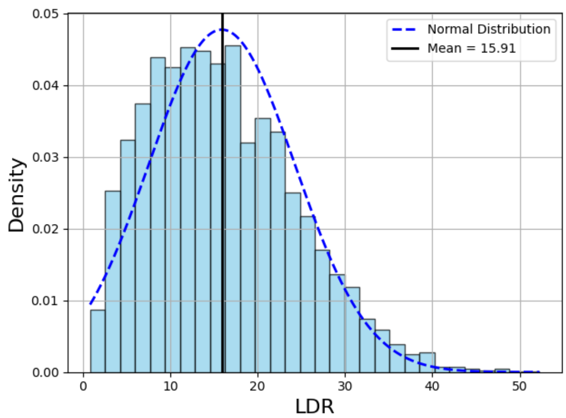

Figure D.2: Histogram for the lift-to-drag ratio (LDR).

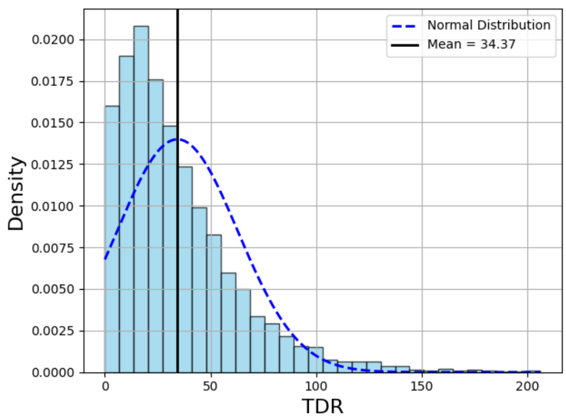

Figure D.3: Histogram for the thrust-to-drag ratio (TDR).

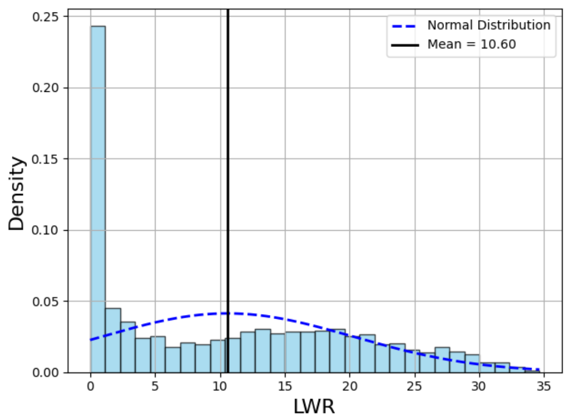

Figure D.4: Histogram for the lift-to-weight ratio (LWR).

Sobol Indices

Sobol indices are global sensitivity analysis variables that express how much an input variable contributes to the output's variance. Therefore, they help to identify which dimensional parameters have the most influence on the performance criteria. First-order indices measure the individual contribution of a given parameter, whereas total Sobol indices account for interactions with other variables, therefore capturing a more accurate influence.

Based on the resulting indices, the magnet thickness ratio t_m, the helical angle α and the outer radius of the wheel R_{out} seem to be the driving parameters behind the considered performance criteria.

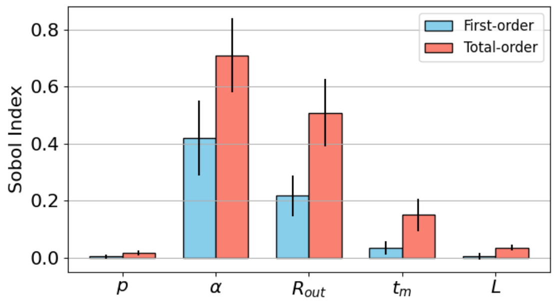

Figure D.5: Sobol indices for the guidance-to-drag ratio (GDR).

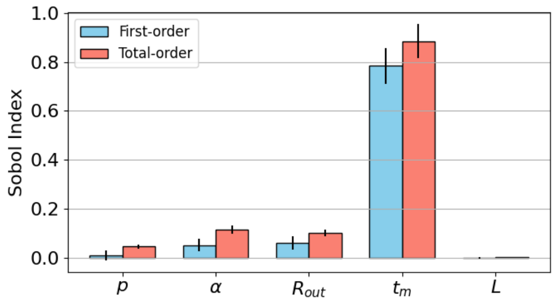

Figure D.6: Sobol indices for the lift-to-drag ratio (LDR).

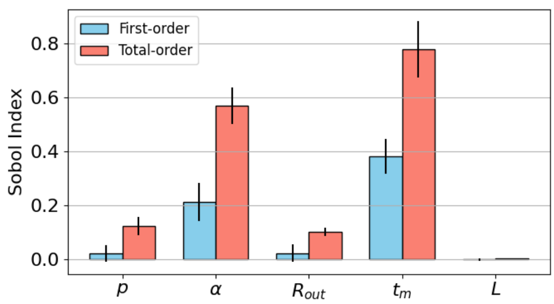

Figure D.7: Sobol indices for the thrust-to-drag ratio (TDR).

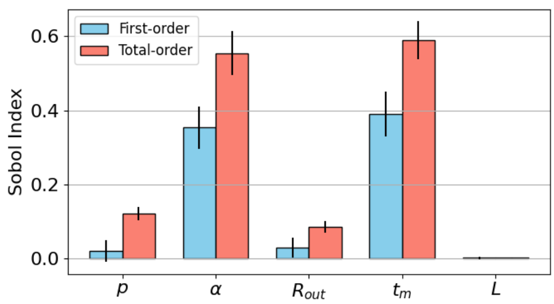

Figure D.8: Sobol indices for the lift-to-weight ratio (LWR).

E | Discretization Algorithms

This appendix presents the equations behind each discretization technique, namely the azimuthal and axial discretizations presented in chapter 8.

Azimuthal discretization

In order to minimize the error, the discretization is performed following a few constraints.

Constraint 1 : Uniformity
Only one type of magnet is considered for the whole discretization of the wheel. That is, all elements have the same width w and height h, resulting in uniform helices. In the same way, the shift $\Delta\theta$ is constant throughout the length of the wheel.

Constraint 2 : Element Height = Pole Height
For the azimuthal discretization algorithm, since the number of pole pairs must be satisfied on each separate ring magnet, the height h of an element in the azimuthal direction must be equal to the ideal azimuthal pole pitch τ_θ, that is :

$$h = \frac{2\pi R}{2p} = \frac{\pi R}{p} = \tau_\theta \tag{E.1}$$

Therefore, the free parameter regarding the dimensions of the element for this type of discretization is the width w.

Constraint 3 : Element Center = Pole Center
In order to minimize the error committed, each element must naturally be centered with regard to the ideal helix. Considering the ideal helix perfectly centered around the helical path that served as reference, each element must be aligned on this path also. This constraint is illustrated in Figure E.1. The dark-blue rectangle represents the discretization element - when properly aligned, the top-right and bottom-left triangles overflow on the neighboring helix. The area of these two triangles, lined in red, is thus the error we wish to minimize.

The centering imposes the element to be split into two rectangles of width $\frac{w}{2}$. The dimension y is defined as the height of the error triangle created. This height can be found with regard to the helical angle α such as :

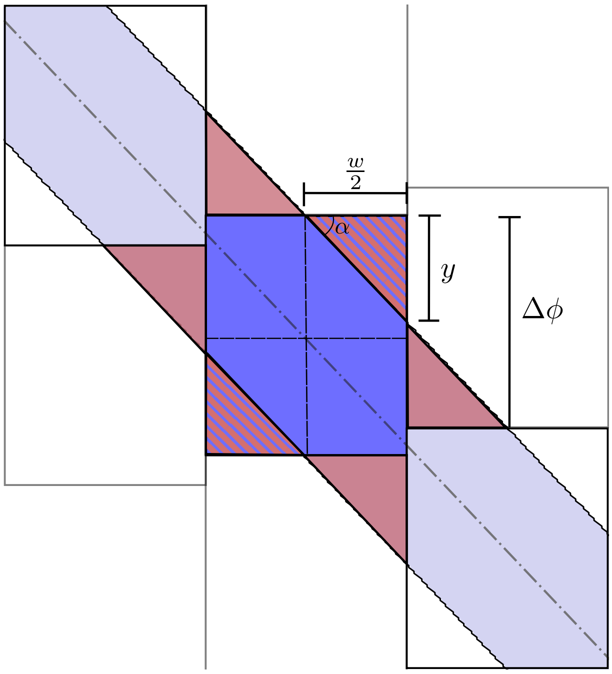

Figure E.1: Element centering on the ideal helical path, for the case of an azimuthal discretization.

$$y = \frac{w}{2} tan(\alpha) \tag{E.2}$$

Since there are no gaps between elements of the discretization, the same error triangle will be defined by the elements of the neighboring helices. This is represented by the plain red triangles on Figure E.1 - whereas lined triangles are the errors committed by the element studied.
Therefore, the angular shift $\Delta\theta$ is imposed by the length of y :

$$\Delta\theta = 2y = w\, tan(\alpha) \tag{E.3}$$

Finally, the area of a single triangle can be computed. Doubling this area gives the total error committed by one element of the discretization.

$$A_{\Delta} = \frac{w\, y}{4} = \frac{w^2\, tan(\alpha)}{8} \tag{E.4}$$

$$A_{\Delta,tot} = 2A_{\Delta} = \frac{w^2\, tan(\alpha)}{4} \tag{E.5}$$

Constraint 4 : Fixed Number of Elements N
As mentioned previously, since the height h of the element is constrained, the free dimensional parameter allowing to reduce the error is the width w. This width is defined by setting a final constraint : the total number of elements - or magnets - we wish to use.

The total number of rows is equal to the number of poles $2p$. Knowing the desired wheel length L, one may estimate the number of elements :

$$N = 2p \left\lfloor \frac{L}{w} \right\rfloor \approx 2p \frac{L}{w} \tag{E.6}$$

By reverting the previous equation, we finally find the width of each element - and in this case the width of the required ring magnet :

$$w = \frac{2\pi L}{N} \tag{E.7}$$

Axial discretization

The discretization is performed following equivalent constraints as for the azimuthal technique, in order to minimize the error.

Constraint 1 : Uniformity
All elements have the same dimensions, and the axial shift Δz is constant from one row to another throughout the whole circumference of the wheel.

Constraint 2 : Element Width = Pole Width
For this discretization algorithm, we impose that the magnet width must be equal to the ideal pole width, that is :

$$w = \frac{2\pi R}{2p\, tan(\alpha)} = \frac{\pi R}{p\, tan(\alpha)} \tag{E.8}$$

Therefore, the free parameter regarding the dimensions of the element for this type of discretization is the height h.

Constraint 3 : Element Center = Pole Center
In the same way as the above development for the azimuthal discretization, each element must naturally be centered with regard to the ideal helix in order to minimize the error committed. This is illustrated in Figure E.2, where the blue rectangle represents the constitutive element of the discretization.

The centering imposes the element to be split into two rectangles of height $\frac{h}{2}$. The dimension x defines the width of the error triangle created. Once again, this width can be defined with regard to the helical angle α such as :

$$x = \frac{h}{2\, tan(\alpha)} \tag{E.9}$$

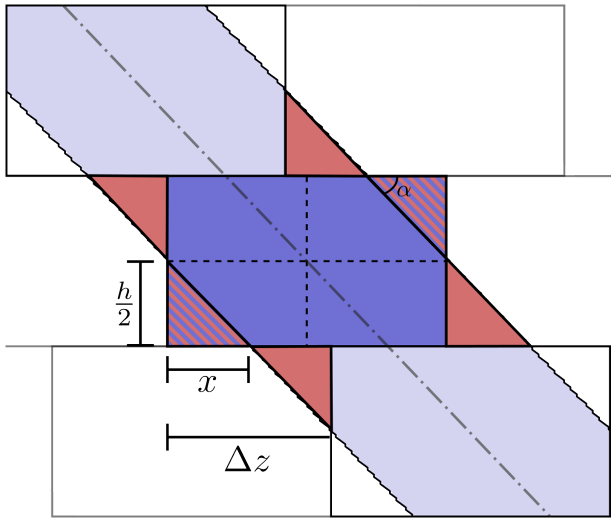

Figure E.2: Element centering on the ideal helical path, for the case of an axial discretization.

Leaving no gaps between magnets, the same error triangle is defined by the elements of the neighboring helices - represented by the plain red triangles in Figure E.2.
The axial shift Δz is thus imposed by the dimension x :

$$\Delta z = 2x = \frac{h}{tan(\alpha)} \tag{E.10}$$

Finally, the area of a single triangle and thus the total error area induced, can be computed :

$$A_{\Delta} = \frac{xh}{4} = \frac{h^2}{8\,tan(\alpha)} \tag{E.11}$$

$$A_{\Delta,tot} = 2A_{\Delta} = \frac{h^2}{4\,tan(\alpha)} \tag{E.12}$$

Constraint 4 : Fixed Number of Elements N
The final constraint allowing us to determine the height h of the magnets is linked to the total number of elements we wish to use.

In a simplified approach, the number of columns and rows in the unwound 2D-plane are respectively $\left\lfloor \frac{L}{w} \right\rfloor$ and $\left\lfloor \frac{2\pi R}{h} \right\rfloor$. Therefore, we can write :

$$N = \left\lfloor \frac{L}{w} \right\rfloor \left\lfloor \frac{2\pi R}{h} \right\rfloor \approx \frac{L}{w}\frac{2\pi R}{h} \tag{E.13}$$

By inverting the previous equation, we find the height of each element :

$$h = \frac{2\pi RL}{wN} \tag{E.14}$$

Polygonal Discretization

Since the magnets where determined beforehand with available stocks, the reasoning behind the discretization has been reversed. Instead of finding the elements' dimensions that would minimize the error, we wish to find the ideal wheel parameters given the constrained size of the constitutive elements.

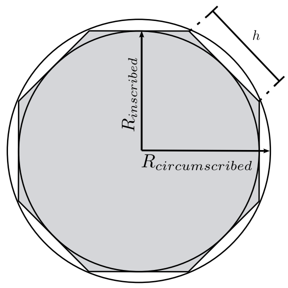

Figure E.3: Polygonal core.

For a regular n-sided polygon, the radius of the inscribed circle can be assimilated to the equivalent inner magnet radius, as shown in Figure E.3. As the number of sides increases, the inscribed and circumscribed radius tend towards each other. This later can thus be estimated as such :

$$R_{inscribed} = \frac{h}{2tan(\frac{\pi}{n})} \tag{E.15}$$

The resulting helical angle can then be computed with the following expression, where p is the chosen number of pole pairs :

$$\alpha = tan^{-1}\left(\frac{\pi R_{inscribed}}{pw}\right) \tag{E.16}$$

F | Experimental Results

This appendix brings together all the experimental results obtained. For each track opening, a force-rotational speed and force-displacement characteristic was measured.

For the 360° track, the speed characteristic established when centered should have no guidance and lift forces. However, these were measured and evolved slightly with the rotational speed. Their magnitude, about 0.3N, is negligeable with regards to the thrust force that reaches 6N.

Inverter-Spindle Frequency

Figure F.1 depicts the linear regression that accounts for the difference between the inverter frequency and the true frequency of the spindle.

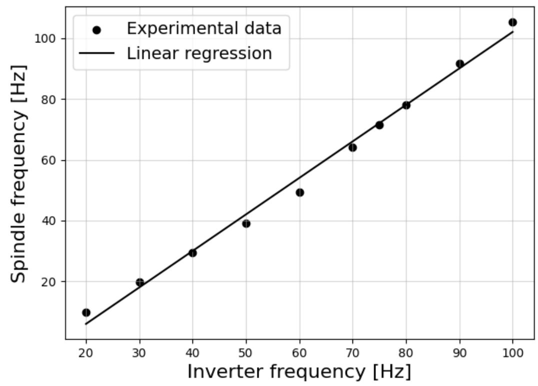

Figure F.1: Linear regression to account for the difference between the set inverter frequency and the real frequency of the spindle.

360° Track

Speed characteristic

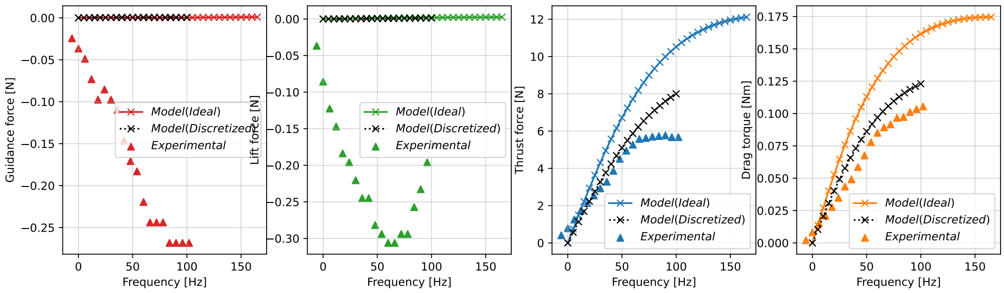

Figure F.2: Speed experimental characterisation for the 360° track.

Displacement characteristic

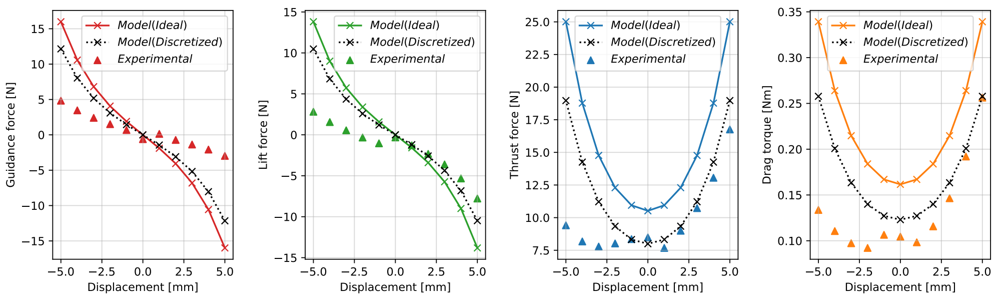

Figure F.3: X-displacement experimental characterisation for the 360° track.

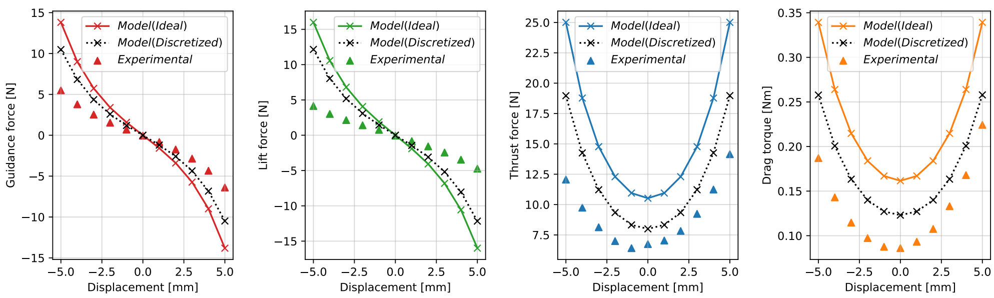

Figure F.4: Y-displacement experimental characterisation for the 360° track.

270° Track

Speed characteristic

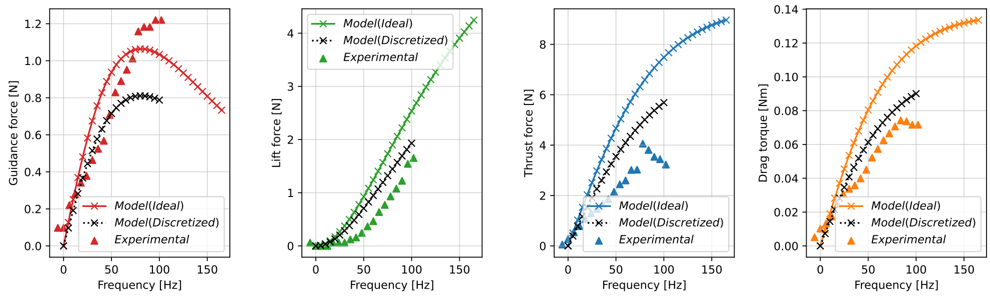

Figure F.5: Speed experimental characterisation for the 270° track.

Displacement characteristic

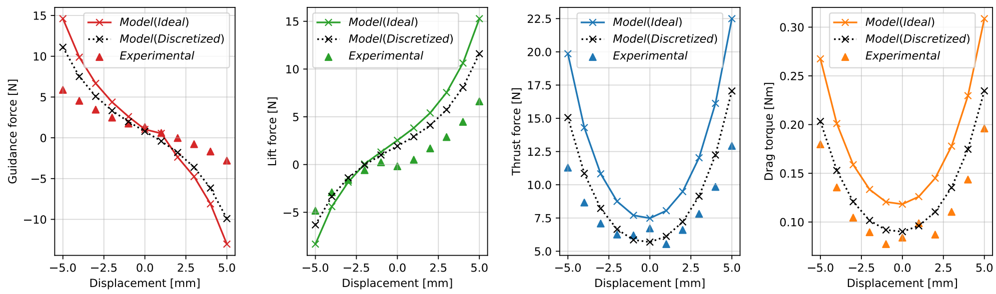

Figure F.6: X-displacement experimental characterisation for the 270° track.

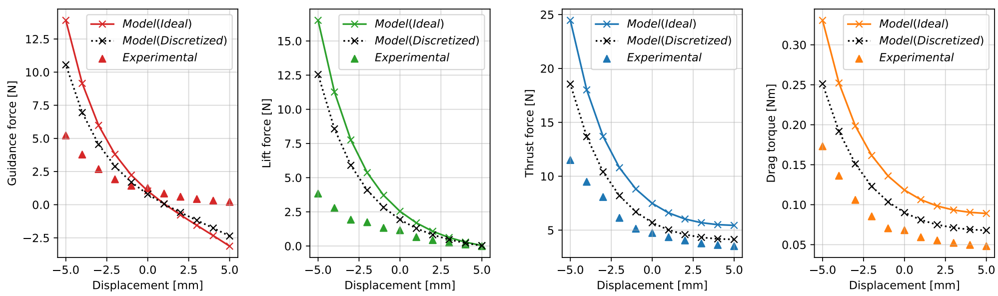

Figure F.7: Y-displacement experimental characterisation for the 270° track.

225° Track

Speed characteristic

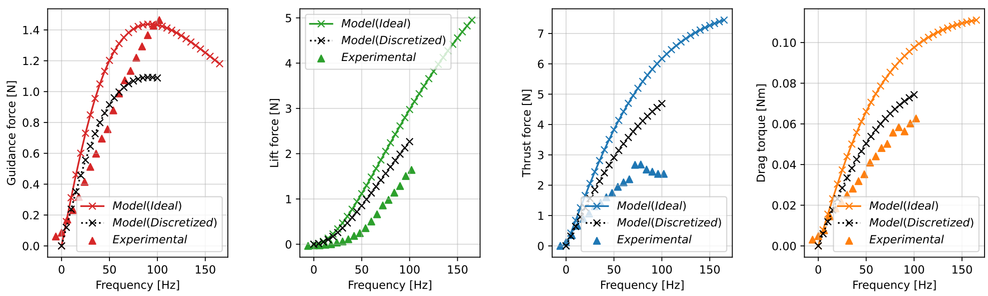

Figure F.8: Speed experimental characterisation for the 225° track.

Displacement characteristic

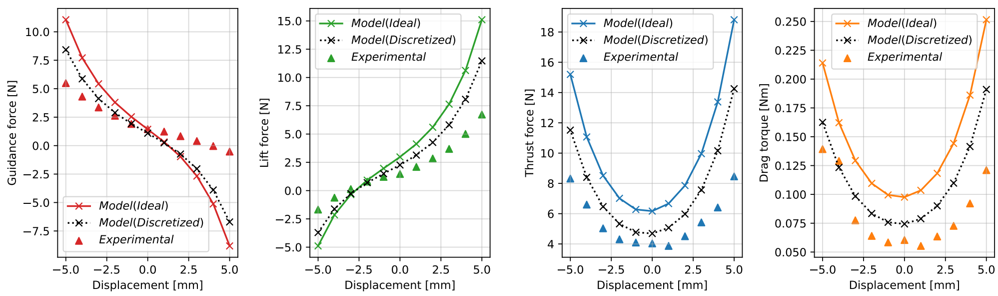

Figure F.9: X-displacement experimental characterisation for the 225° track.

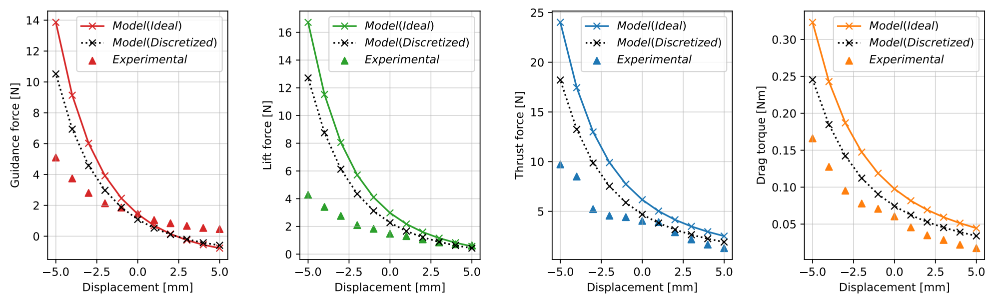

Figure F.10: Y-displacement experimental characterisation for the 225° track.

180° Track

Speed characteristic

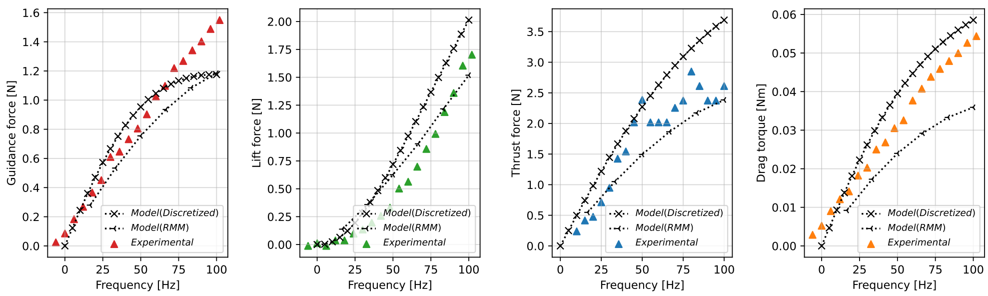

Figure F.11: Speed experimental characterisation for the 180° track.

Displacement characteristic

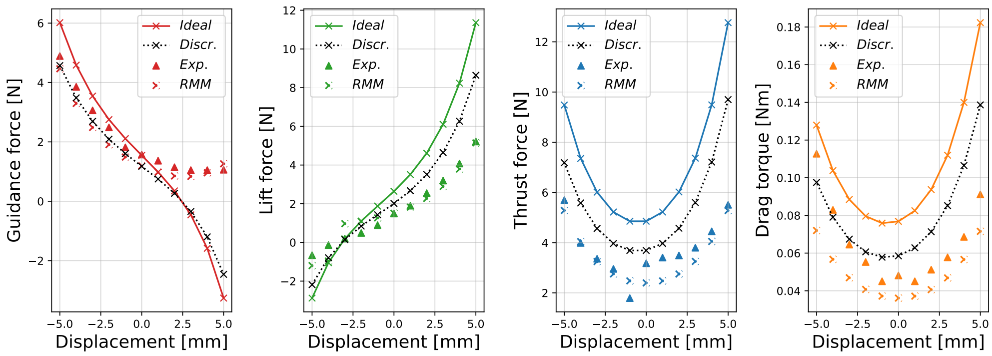

Figure F.12: X-displacement experimental characterisation for the 180° track.

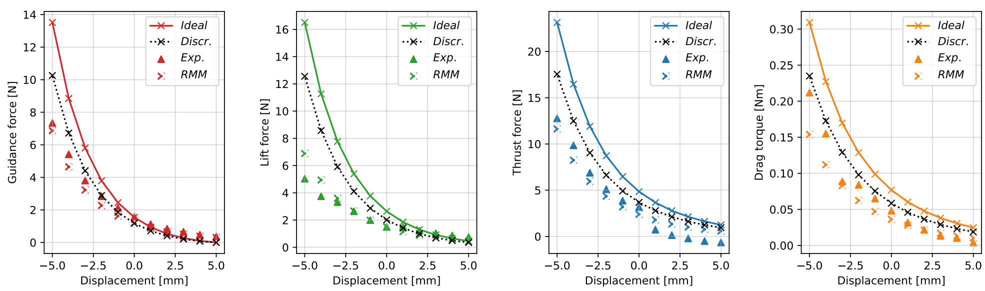

Figure F.13: Y-displacement experimental characterisation for the 180° track.

G | Technical Drawings

This appendix presents the technical drawings used for the manufacturing of the various parts of the test bench.

These technical drawings are, in order :

1. Interface 1 : Sensor-Linear Slide
2. Interface 2 : Sensor-Tracks
3. Track 360°
4. Track 180°
5. Track 270°
6. Track 225°
7. Rotor
8. EDM Plate

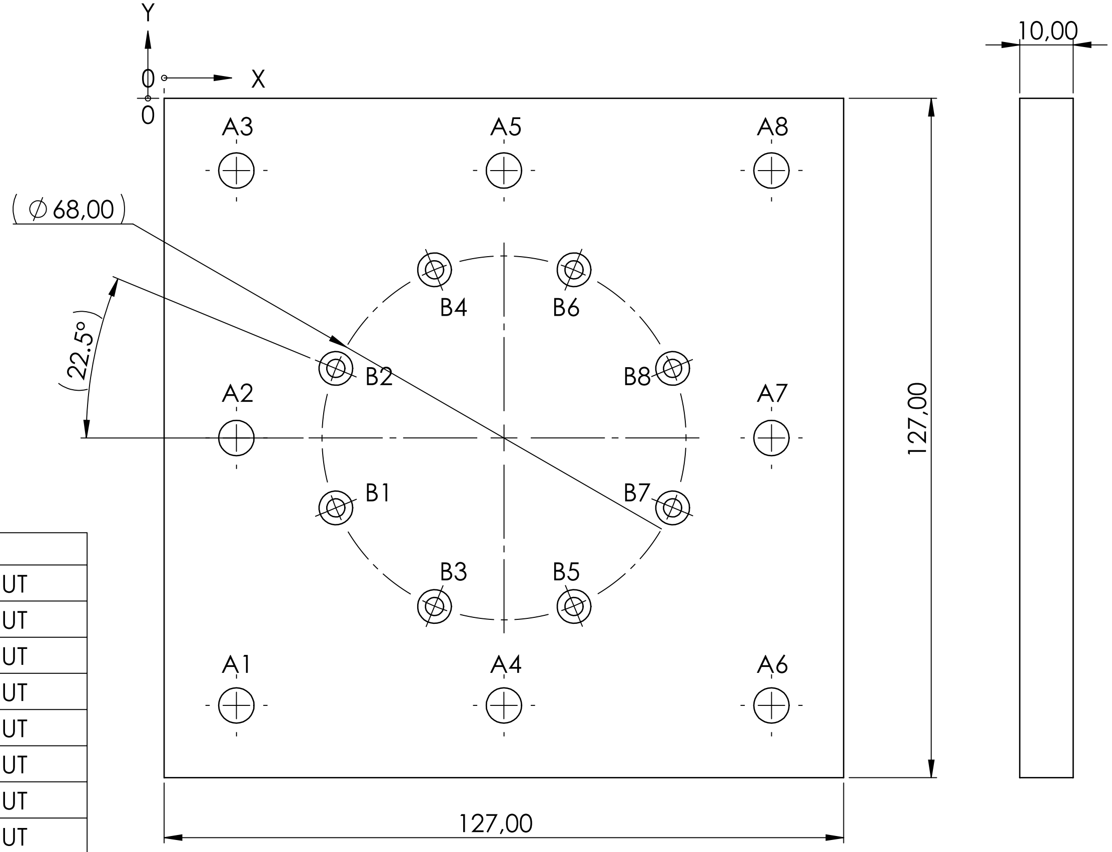

REPERE	POSITION X	POSITION Y	TAILLE
A1	13,50	-113,50	∅ 6,60 A TRAVERS TOUT
A2	13,50	-63,50	∅ 6,60 A TRAVERS TOUT
A3	13,50	-13,50	∅ 6,60 A TRAVERS TOUT
A4	63,50	-113,50	∅ 6,60 A TRAVERS TOUT
A5	63,50	-13,50	∅ 6,60 A TRAVERS TOUT
A6	113,50	-113,50	∅ 6,60 A TRAVERS TOUT
A7	113,50	-63,50	∅ 6,60 A TRAVERS TOUT
A8	113,50	-13,50	∅ 6,60 A TRAVERS TOUT
B1	32,09	-76,56	∅ 3,40 A TRAVERS TOUT ∨ ∅ 6,30 X 90°
B2	32,09	-50,49	∅ 3,40 A TRAVERS TOUT ∨ ∅ 6,30 X 90°
B3	50,52	-95	∅ 3,40 A TRAVERS TOUT ∨ ∅ 6,30 X 90°
B4	50,52	-32,05	∅ 3,40 A TRAVERS TOUT ∨ ∅ 6,30 X 90°
B5	76,60	-95	∅ 3,40 A TRAVERS TOUT ∨ ∅ 6,30 X 90°
B6	76,60	-32,05	∅ 3,40 A TRAVERS TOUT ∨ ∅ 6,30 X 90°
B7	95,03	-76,56	∅ 3,40 A TRAVERS TOUT ∨ ∅ 6,30 X 90°
B8	95,03	-50,49	∅ 3,40 A TRAVERS TOUT ∨ ∅ 6,30 X 90°

SAUF INDICATION CONTRAIRE: LES COTES SONT EN MILLIMETRES TOLERANCES: ISO 2768 - mK

FINITION:

CASSER LES ANGLES VIFS

NE PAS CHANGER L'ECHELLE

REVISION

	NOM	PRENOM	DATE
AUTEUR	Georgopoulos	Alexandra	07/03/25
VERIF.			
APPR.			
FAB.			
QUAL.			

TITRE: TFE POD : Sensor - Table Interface

MATERIAU: Aluminium

No. DE PLAN: 1

A3

MASSE:

ECHELLE:1:2

FEUILLE 1 SUR 1

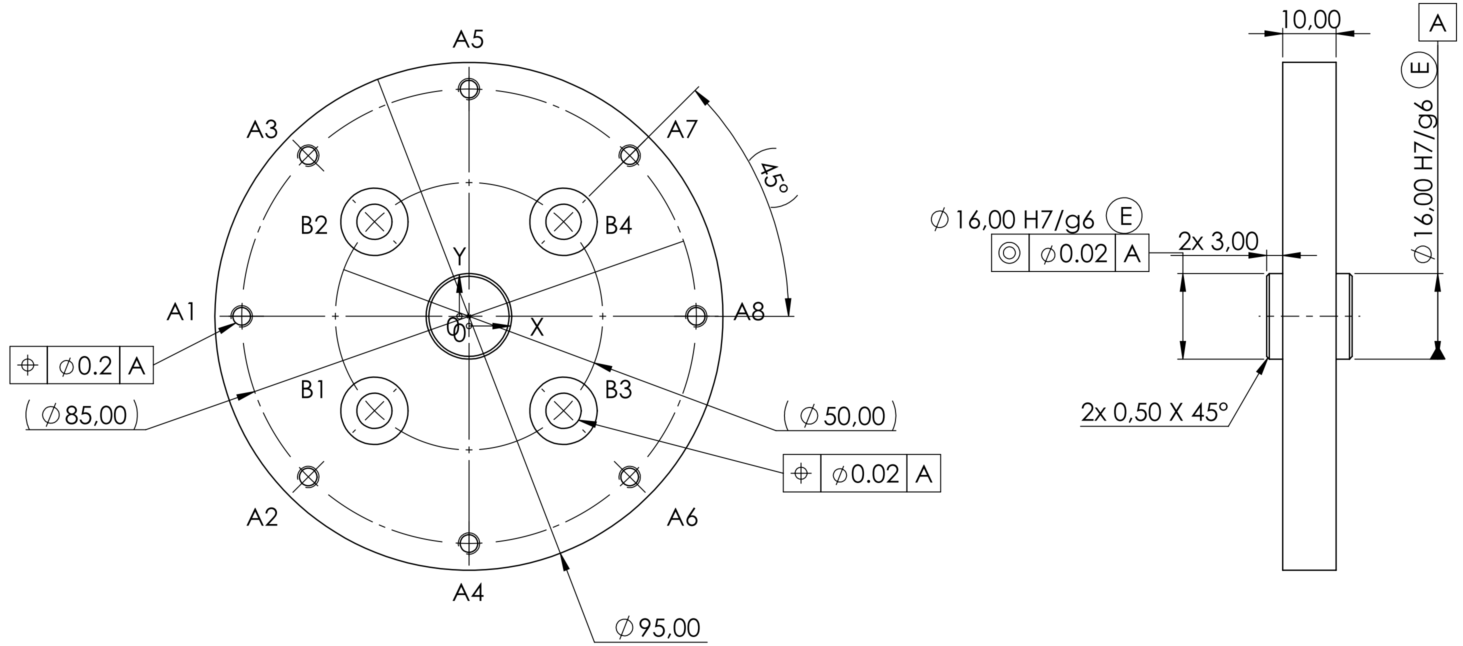

REPERE	POSITION X	POSITION Y	TAILLE
A1	-42,50	0	Ø 3,30 A TRAVERS TOUT M4 - 6H A TRAVERS TOUT
A2	-30,05	-30,05	Ø 3,30 A TRAVERS TOUT M4 - 6H A TRAVERS TOUT
A3	-30,05	30,05	Ø 3,30 A TRAVERS TOUT M4 - 6H A TRAVERS TOUT
A4	0	-42,50	Ø 3,30 A TRAVERS TOUT M4 - 6H A TRAVERS TOUT
A5	0	42,50	Ø 3,30 A TRAVERS TOUT M4 - 6H A TRAVERS TOUT
A6	30,05	-30,05	Ø 3,30 A TRAVERS TOUT M4 - 6H A TRAVERS TOUT
A7	30,05	30,05	Ø 3,30 A TRAVERS TOUT M4 - 6H A TRAVERS TOUT
A8	42,50	0	Ø 3,30 A TRAVERS TOUT M4 - 6H A TRAVERS TOUT
B1	-17,68	-17,68	Ø 6,60 A TRAVERS TOUT ⌵ Ø 12,60 X 90°
B2	-17,68	17,68	Ø 6,60 A TRAVERS TOUT ⌵ Ø 12,60 X 90°
B3	17,68	-17,68	Ø 6,60 A TRAVERS TOUT ⌵ Ø 12,60 X 90°
B4	17,68	17,68	Ø 6,60 A TRAVERS TOUT ⌵ Ø 12,60 X 90°

SAUF INDICATION CONTRAIRE: LES COTES SONT EN MILLIMETRES
TOLERANCES: ISO 2768 - mK

FINITION:

CASSER LES ANGLES VIFS

NE PAS CHANGER L'ECHELLE

REVISION

	NOM	PRENOM	DATE
AUTEUR	Georgopoulos	Alexandra	07/03/25
VERIF.			
APPR.			
FAB.			
QUAL.			

TITRE: TFE POD : Sensor - Rail Interface

MATERIAU: Aluminium

No. DE PLAN: 2

A3

MASSE:

ECHELLE:1:1

FEUILLE 1 SUR 1

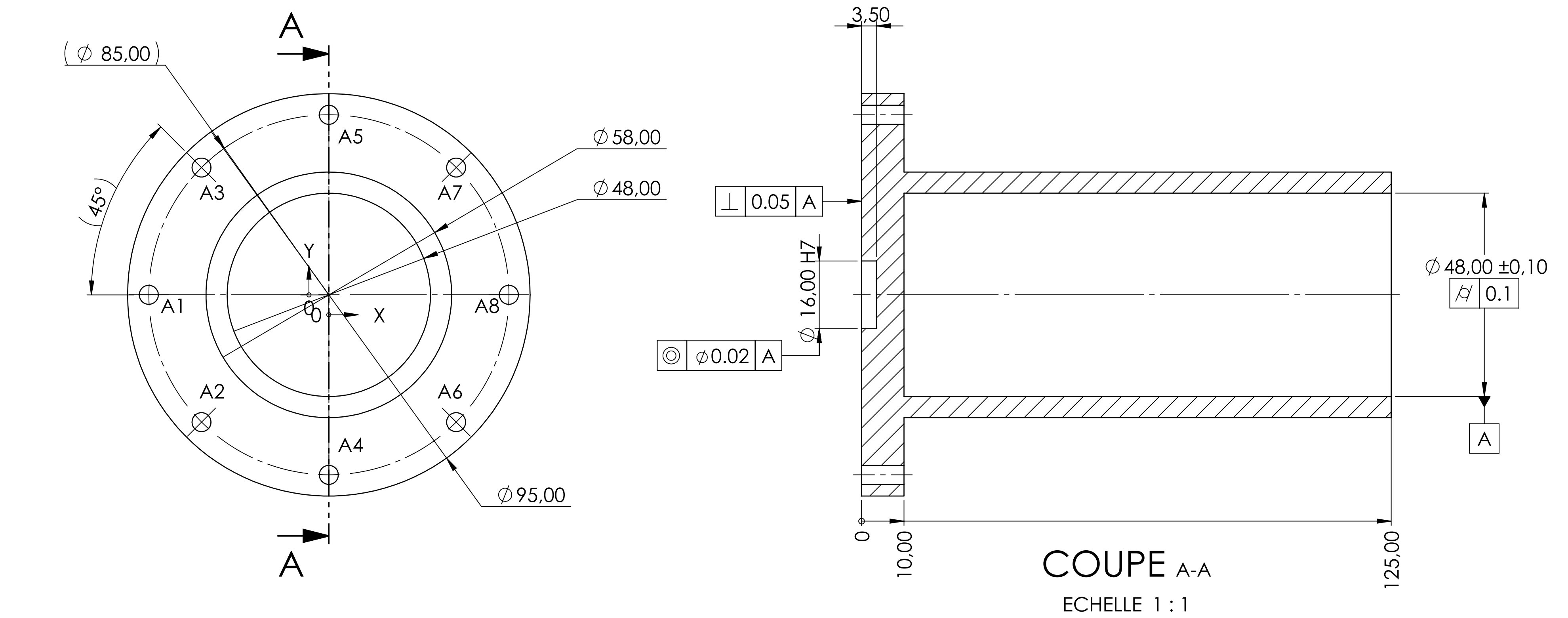

REPERE	POSITION X	POSITION Y	TAILLE
A1	-42,50	0	⌀ 4,50 A TRAVERS TOUT
A2	-30,05	-30,05	⌀ 4,50 A TRAVERS TOUT
A3	-30,05	30,05	⌀ 4,50 A TRAVERS TOUT
A4	0	-42,50	⌀ 4,50 A TRAVERS TOUT
A5	0	42,50	⌀ 4,50 A TRAVERS TOUT
A6	30,05	-30,05	⌀ 4,50 A TRAVERS TOUT
A7	30,05	30,05	⌀ 4,50 A TRAVERS TOUT
A8	42,50	0	⌀ 4,50 A TRAVERS TOUT

SAUF INDICATION CONTRAIRE:
LES COTES SONT EN MILLIMETRES
TOLERANCES:
ISO 2768 - mK

FINITION:

CASSER LES ANGLES VIFS

NE PAS CHANGER L'ECHELLE

REVISION

	NOM	PRENOM	DATE
AUTEUR	Georgopoulos	Alexandra	13/03/25
VERIF.			
APPR.			
FAB.			
QUAL.			

TITRE:
TFE POD :
Track 360°

MATERIAU:
Aluminium

No. DE PLAN
3

A3

MASSE:

ECHELLE:1:2

FEUILLE 1 SUR 1

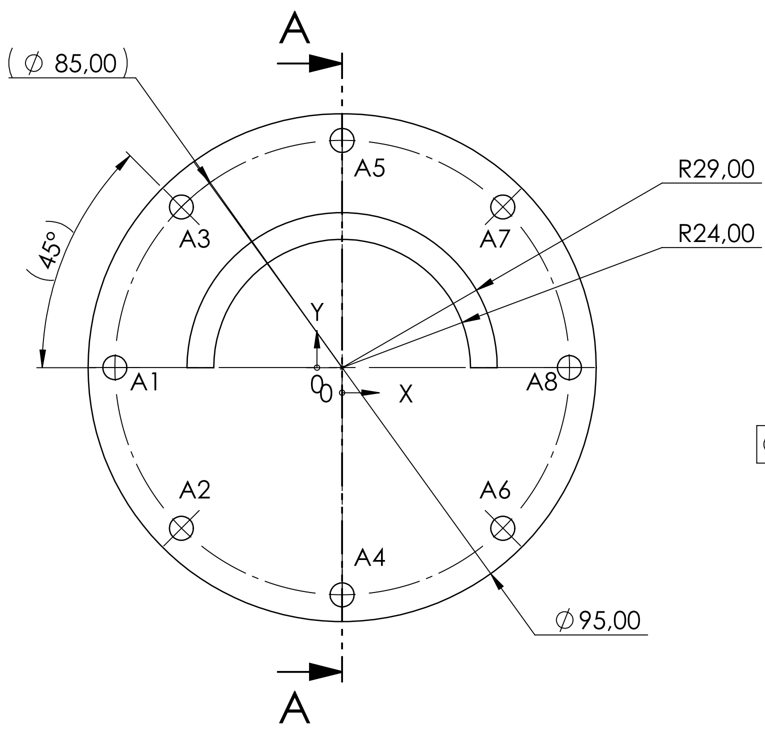

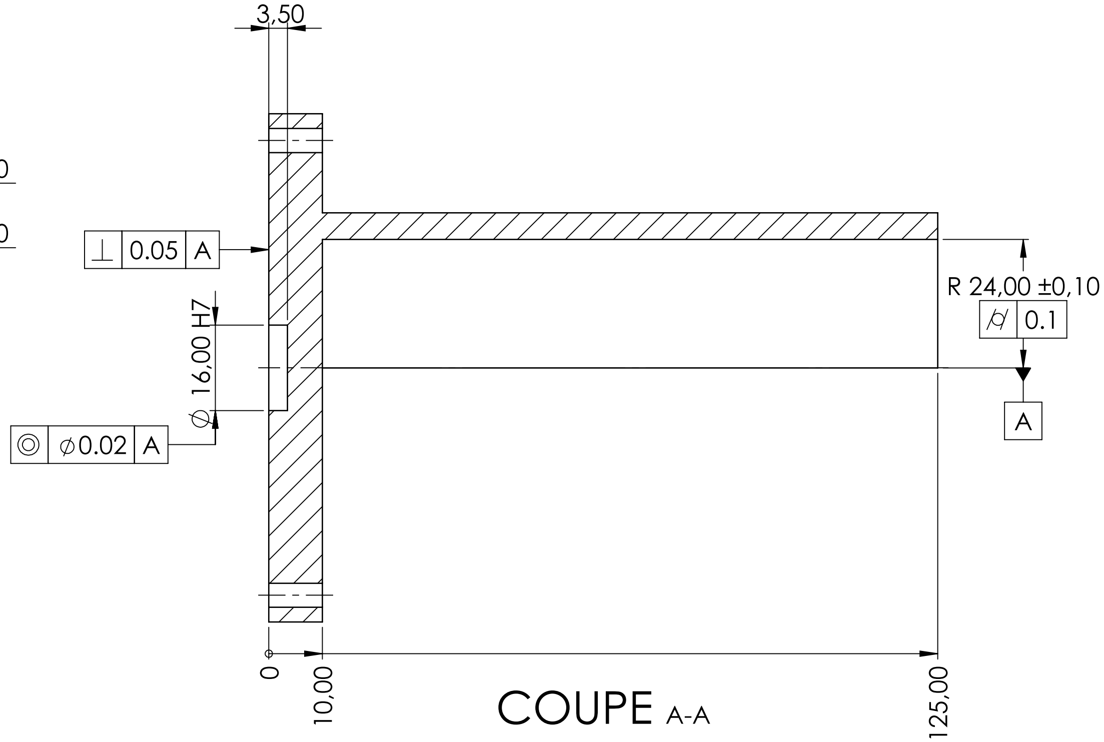

COUPE A-A

ECHELLE 1 : 1

REPERE	POSITION X	POSITION Y	TAILLE
A1	-42,50	0	⌀ 4,50 A TRAVERS TOUT
A2	-30,05	-30,05	⌀ 4,50 A TRAVERS TOUT
A3	-30,05	30,05	⌀ 4,50 A TRAVERS TOUT
A4	0	-42,50	⌀ 4,50 A TRAVERS TOUT
A5	0	42,50	⌀ 4,50 A TRAVERS TOUT
A6	30,05	-30,05	⌀ 4,50 A TRAVERS TOUT
A7	30,05	30,05	⌀ 4,50 A TRAVERS TOUT
A8	42,50	0	⌀ 4,50 A TRAVERS TOUT

SAUF INDICATION CONTRAIRE:
LES COTES SONT EN MILLIMETRES
TOLERANCES:
ISO 2768 - mK

FINITION:

CASSER LES ANGLES VIFS

NE PAS CHANGER L'ECHELLE

REVISION

	NOM	PRENOM	DATE
AUTEUR	Georgopoulos	Alexandra	13/03/25
VERIF.			
APPR.			
FAB.			
QUAL.			

TITRE:
TFE POD :
Track 180°

MATERIAU: Aluminium

No. DE PLAN: 4

A3

MASSE:

ECHELLE:1:2

FEUILLE 1 SUR 1

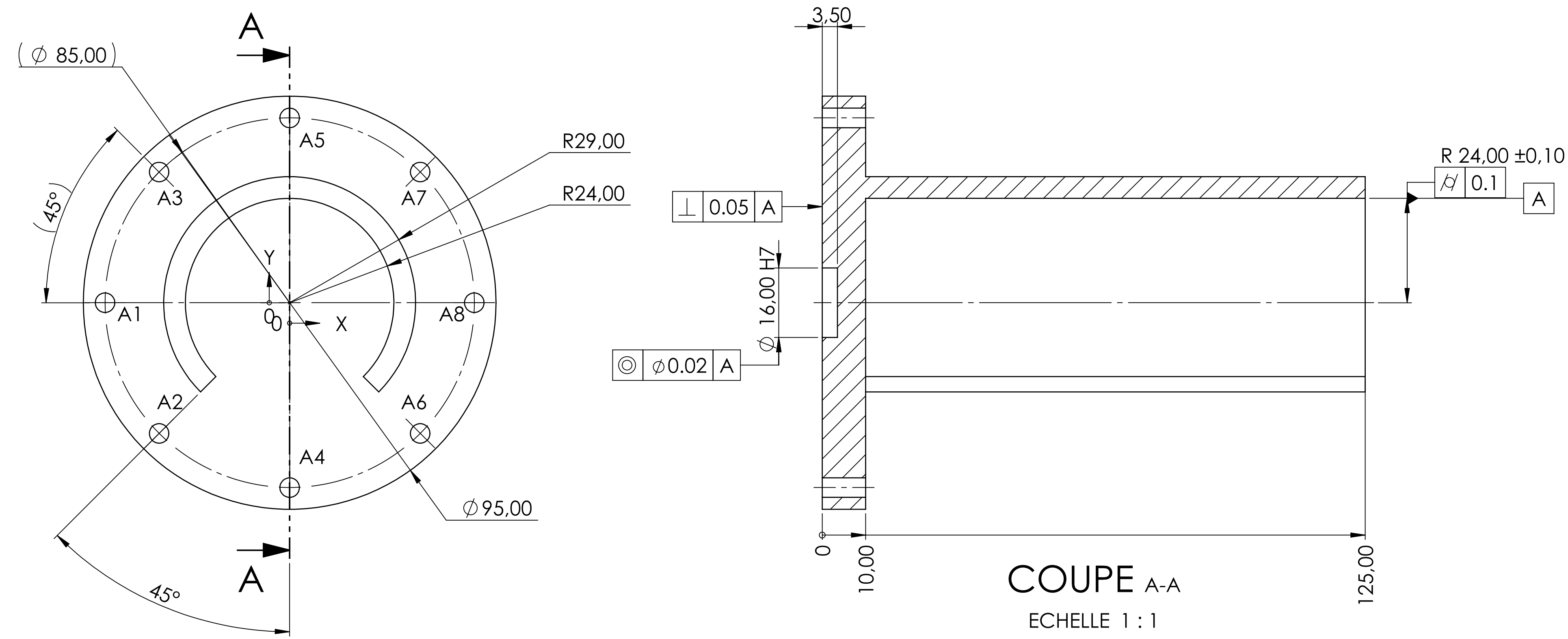

COUPE A-A

ECHELLE 1 : 1

REPERE	POSITION X	POSITION Y	TAILLE
A1	-42,50	0	∅ 4,50 A TRAVERS TOUT
A2	-30,05	-30,05	∅ 4,50 A TRAVERS TOUT
A3	-30,05	30,05	∅ 4,50 A TRAVERS TOUT
A4	0	-42,50	∅ 4,50 A TRAVERS TOUT
A5	0	42,50	∅ 4,50 A TRAVERS TOUT
A6	30,05	-30,05	∅ 4,50 A TRAVERS TOUT
A7	30,05	30,05	∅ 4,50 A TRAVERS TOUT
A8	42,50	0	∅ 4,50 A TRAVERS TOUT

SAUF INDICATION CONTRAIRE: LES COTES SONT EN MILLIMETRES TOLERANCES: ISO 2768 - mK

FINITION:

CASSER LES ANGLES VIFS

NE PAS CHANGER L'ECHELLE

REVISION

	NOM	PRENOM	DATE
AUTEUR	Georgopoulos	Alexandra	13/03/25
VERIF.			
APPR.			
FAB.			
QUAL.			

TITRE: TFE POD : Track 270°

MATERIAU: Aluminium

No. DE PLAN: 5

A3

MASSE:

ECHELLE:1:2

FEUILLE 1 SUR 1

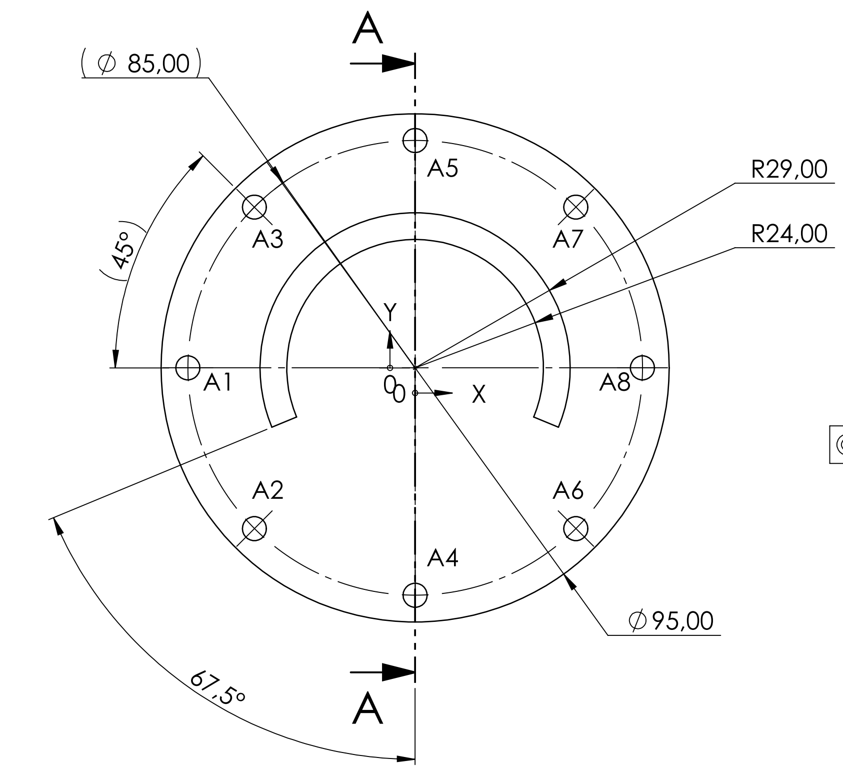

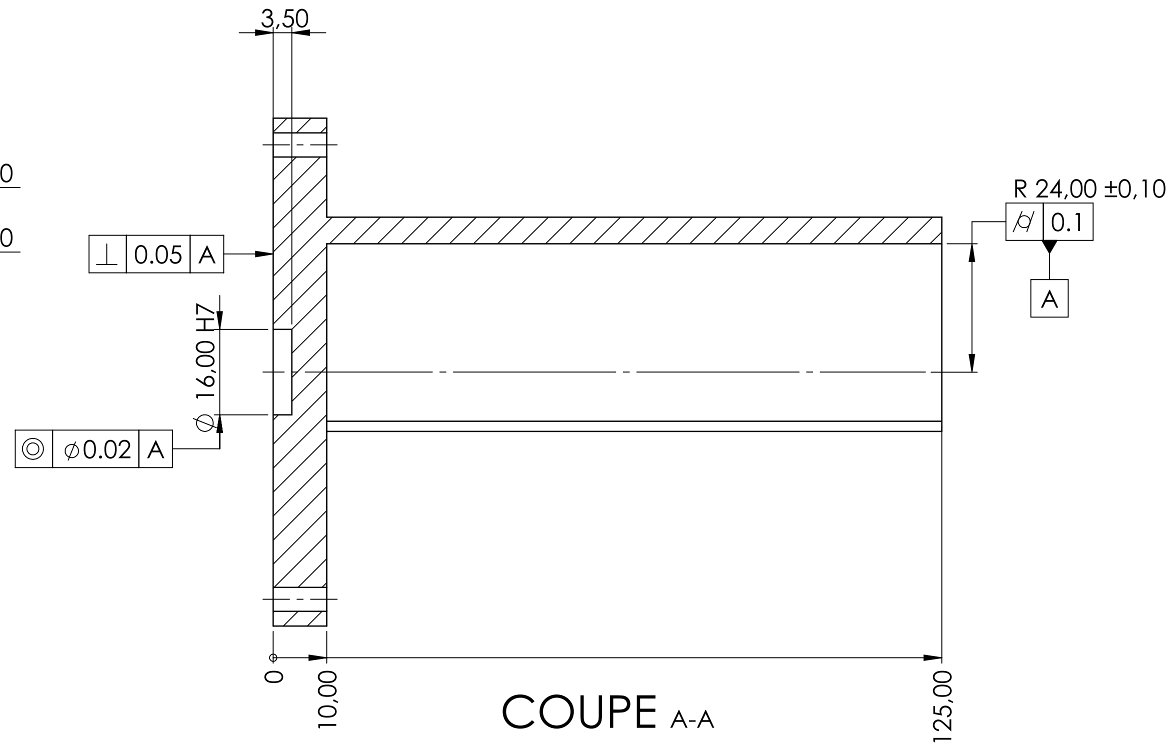

COUPE A-A

ECHELLE 1 : 1

REPERE	POSITION X	POSITION Y	TAILLE
A1	-42,50	0	⌀ 4,50 A TRAVERS TOUT
A2	-30,05	-30,05	⌀ 4,50 A TRAVERS TOUT
A3	-30,05	30,05	⌀ 4,50 A TRAVERS TOUT
A4	0	-42,50	⌀ 4,50 A TRAVERS TOUT
A5	0	42,50	⌀ 4,50 A TRAVERS TOUT
A6	30,05	-30,05	⌀ 4,50 A TRAVERS TOUT
A7	30,05	30,05	⌀ 4,50 A TRAVERS TOUT
A8	42,50	0	⌀ 4,50 A TRAVERS TOUT

SAUF INDICATION CONTRAIRE: LES COTES SONT EN MILLIMETRES TOLERANCES: ISO 2768 - mK

FINITION:

CASSER LES ANGLES VIFS

NE PAS CHANGER L'ECHELLE

REVISION

	NOM	PRENOM	DATE
AUTEUR	Georgopoulos	Alexandra	13/03/25
VERIF.			
APPR.			
FAB.			
QUAL.			

TITRE: TFE POD : Track 225°

MATERIAU: Aluminium

No. DE PLAN: 6

A3

MASSE:

ECHELLE:1:2

FEUILLE 1 SUR 1

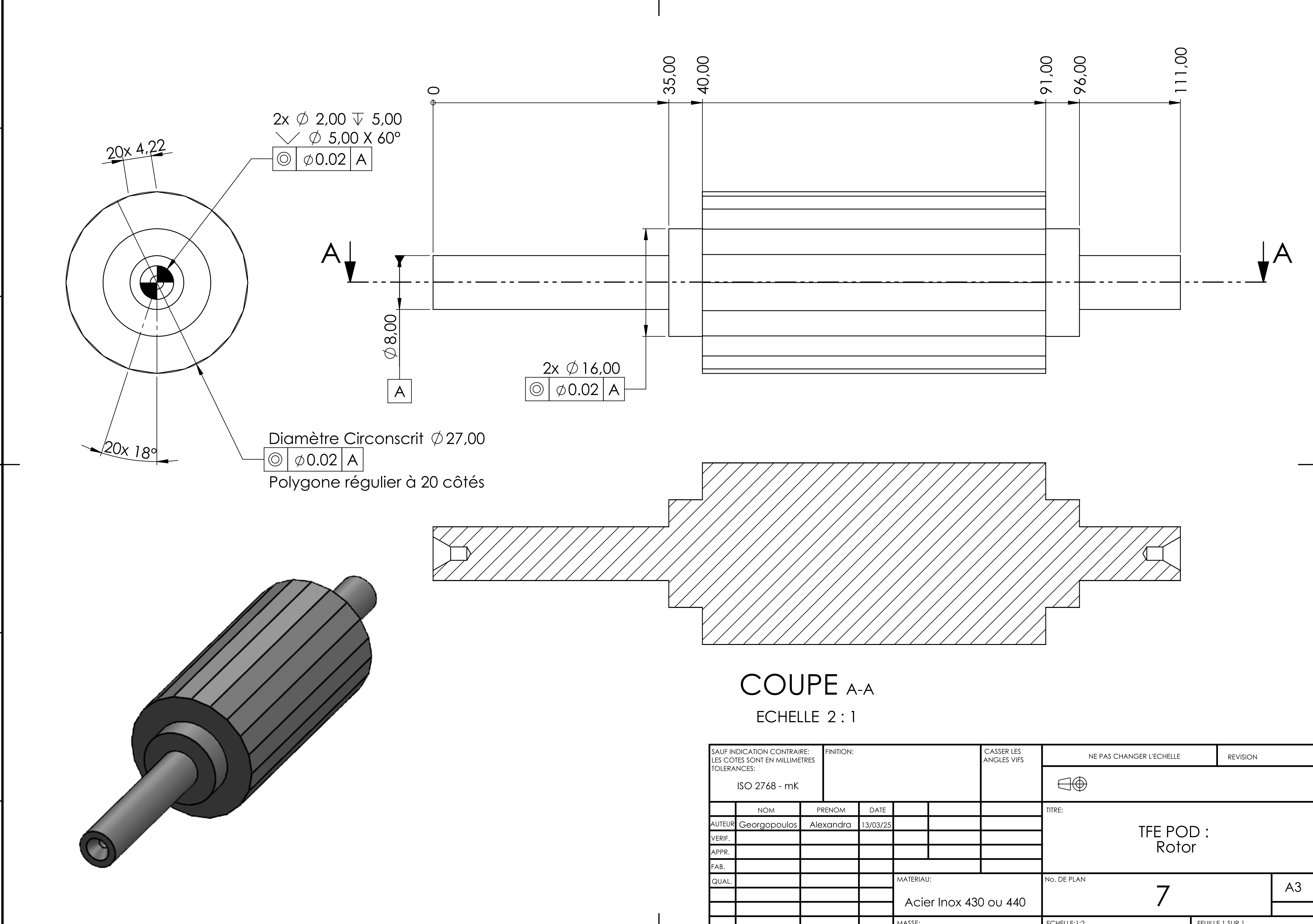

SAUF INDICATION CONTRAIRE: LES COTES SONT EN MILLIMETRES TOLERANCES: ISO 2768 - mK	FINITION:	CASSER LES ANGLES VIFS	NE PAS CHANGER L'ECHELLE	REVISION	
	NOM	PRENOM	DATE	TITRE: TFE POD : Rotor	
AUTEUR	Georgopoulos	Alexandra	13/03/25		
VERIF.					
APPR.					
FAB.					
QUAL.			MATERIAU: Acier Inox 430 ou 440	No. DE PLAN 7	A3
			MASSE:	ECHELLE:1:2	FEUILLE 1 SUR 1

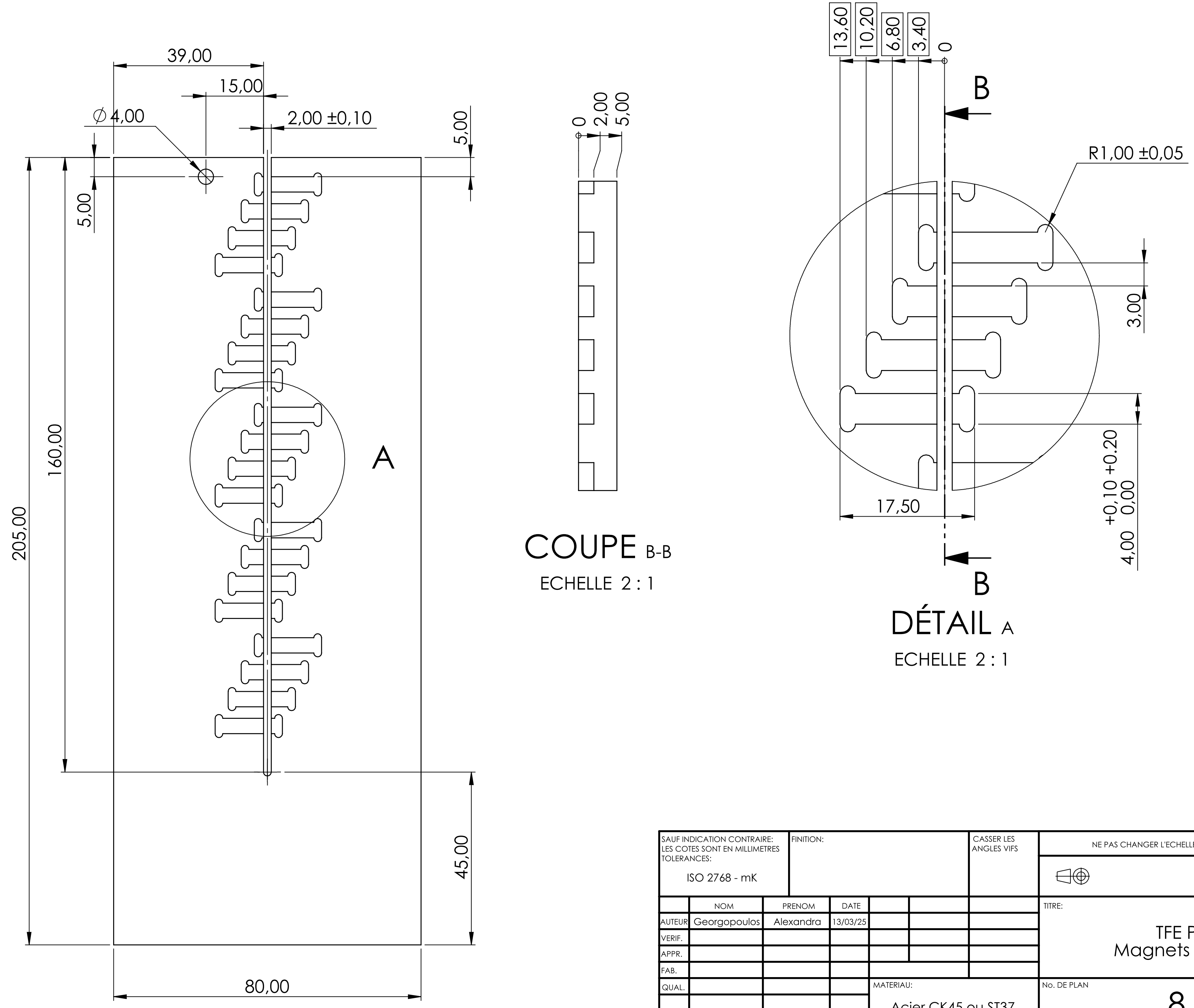

SAUF INDICATION CONTRAIRE: LES COTES SONT EN MILLIMETRES TOLERANCES: ISO 2768 - mK	FINITION:	CASSER LES ANGLES VIFS	NE PAS CHANGER L'ECHELLE	REVISION	
	NOM	PRENOM	DATE	TITRE: TFE POD : Magnets EDM Plate	
AUTEUR	Georgopoulos	Alexandra	13/03/25		
VERIF.					
APPR.					
FAB.					
QUAL.			MATERIAU: Acier CK45 ou ST37	No. DE PLAN 8	A3
			MASSE:	ECHELLE:1:2	FEUILLE 1 SUR 1

UNIVERSITÉ CATHOLIQUE DE LOUVAIN
École polytechnique de Louvain
Rue Archimède, 1 bte L6.11.01, 1348 Louvain-la-Neuve, Belgique | **www.uclouvain.be/epl**